The development of a multi-model optical imaging system to investigate hemodynamic responses to tissue injury in vivo

Jia Qin

A dissertation

submitted in partial fulfillment of the

requirements for the degree of

Doctor of Philosophy

University of Washington

2014

Reading Committee:

Ruikang Wang, Chair

Chun Yuan

Henry Lai

Program Authorized to Offer Degree:

Bioengineering

Jia Qin

University of Washington

Abstract

The development of a multi-model optical imaging system to investigate hemodynamic responses to tissue injury *in vivo*

Jia Qin

Chair of the Supervisory Committee
Professor Ruikang Wang
Bioengineering

Ischemic injury is caused by blockage or rupture of a blood vessel supplying an organ with oxygen and nutrients. A reduction of blood flow in the brain below critical values leads to a series of metabolic, functional, and structural changes resulting in irreversible cell death (1). Ability to non-invasively monitor and quantify functional blood flow, tissue morphology, and blood oxygenation is important for improvement of diagnosis, treatment and management of ischemic injury. Decreased blood flow above the critical value leads to permanent cell death, but a portion of the hypoperfusion region has the potential for recovery. Over the past several decades, much effort has been put forth in investigating endogenous mechanisms involved in salvaging the hypoperfusion region but has focused on neuroprotective mechanisms with little attention given to the vasculature (2). This is most likely due to the lack of a technology capable of elucidating real time macro- and micro-vascular dynamics *in vivo*. Moreover, there are no techniques that can satisfactorily extract the aforementioned parameters from *in vivo* macro- and micro-circulatory tissue beds, with sufficient resolution at defined depth and without any harm to the tissue. The ability which could localize macrovasculature and subsequently visualize the detailed microvasculature networks with multiple parameters is crucial to determine the blood supply status under the pathophysiologic and metabolic conditions.

In this thesis, we developed a multi-model imaging system to achieve a more comprehensive understanding of macro- and micro-vascular responses and hemodynamic parameters during and after ischemic injury, which would greatly improve our ability to develop therapeutic interventions to improve vascular function. There are three specific aims.

(I). Development of the 1st generation multi-model imaging system capable of providing hemodynamic and morphological information of macro- and micro-circulatory tissue beds *in vivo.*

We developed a multi-model imaging system that integrates together the functions of multi-wavelength laser speckle contrast imaging (LSCI) and optical microangiography (OMAG), so that it can rapidly image hemodynamic within living tissues in three dimensions (3D), providing important physiological parameters, e.g., functional blood flow, blood oxygenation, and tissue morphology. For multi-wavelength LSCI, we used two laser sources at different wavelengths, in which a mechanical chopper was used to modulate the illumination light to provide the measurement of blood flow and blood oxygenation. For OMAG, we used the ultrahigh sensitive OMAG (UHS-OMAG) system because of its sensitivity to image functional microcirculations with capillary details. We evaluated the performance of the system using an *in vivo* mouse pinna model through the imaging of blood vessel networks before and after a burn injury.

(II). Improvement of the imaging speed of multi-model imaging system

The imaging speed is a key to the investigation of fast hemodynamic responses (in milliseconds) in an injury. We envisioned that the first generation (1st G) system would have limited imaging speed due to the use of mechanical chopper to control the multi-wavelength LSCI. To mitigate this problem, we advanced the 1st G system, by the use of two synchronized cameras to concurrently capture the laser speckle images at 780-nm and 825-nm wavelengths; so that the rapid changes of blood flow rate and hemoglobin concentration can be provided. We also developed novel algorithms that will enable the direction of blood flow to be monitored.

(III). Validation of the utility of multi-model imaging system for serial monitoring of macro- and micro-vasculature changes following ischemic injury

Using the system we developed, we defined the characteristics of blood flow and oxygenation variations during baseline, occlusion, and reperfusion in an experimental ischemic stroke model. We also correlated measured macro- and micro-vascular responses with the results obtained by conventional histopathology.

The immediate outcome of this research is that we can simultaneously monitor blood flow, blood oxygenation, and tissue morphology in ischemic injury *in vivo*. This technology would be valuable in future research studies that aim to improve our understanding of vascular involvement under pathologic and physiological conditions, and ultimately facilitate clinical diagnosis, monitoring, and therapeutic interventions of neurovascular diseases.

Table and Contents

List of Figures

Acknowledgments

First and foremost, I would like to thank Drs. Ruikang Wang, Chun Yuan, Henry Lai and Xiaodong Xu for being my supervisory committee, Drs. Paul Yager, David Marcinek for being my Qualifying exam committee. Drs. Ruikang Wang and Henry Lai took part in all three of my graduate school examinations: Qualifying, General, and Final Exams. Along the way, I would like to thank my committee for the valuable suggestions and comments, which help me think further and deeper and to have a more thorough understanding and examination of the research projects.

The research presented in this dissertation was done under the guidance of Dr. Ruikang Wang in Biophotonics and Imaging Laboratory (BAIL) at the University of Washington. He afforded me the opportunity to take part in variable research projects. I would like to thank Dr. Wang for his advice at each step of this journey, as none of the work in this dissertation would have been possible without him.

I would like to thank Drs. Lei Shi, Suzan Dziennis, and Roberto Reif for their support in my experiments and comments on my publication during this journey. It is extremely fortunate to work and collaborate with all of you.

I would like to thank Dr. Lin An, Dr. Jingying Jiang, Ph.D candidate Siavash Yousefi, Dr. Yi Wang, Dr. Zhenhe Ma, Ph.D candidate Zhongwei Zhi, Dr. Yali Jia, Dr. Hequn Wang, Dr. Xin Yin, and all other lab mates and research collaborators, who provided support on the projects or assisted with the research.

I would also like to thank my families for helping me smile and being anchors to me during the highs and lows of graduate school. Thank you, my husband, my kids, and my parents.

Finally, I would like to thank the NIH research grant for providing the continuous support for the projects.

Chapter 1. Introduction

1.1 Clinical background

The blood vasculature regulates blood flow and tissue perfusion, and mediates the delivery of nutrients and oxygen to living tissue (3). Blood flow, blood oxygenation, and tissue morphology are important fluid dynamic, biochemical, and anatomical parameters that can be quantified (3, 4). An adequate blood flow is a prerequisite for the tissue to function properly (5). An impairment of blood flow is the direct cause of progression of ~60% of the diseases, such as stroke, that lead to severe disability and death (6). Tissue oxygenation is a sensitive indicator of tissue status (7), e.g., a sudden dip in tissue oxygenation can be a direct indication of severe conditions such as tissue degeneration (8). The pathological morphology of blood vessels, such as blood vessel distortion (9) and rarefaction (10, 11) is closely related to a certain abnormal state of living tissues (12). Reports have shown that diabetes mellitus patients suffer from absence of capillary reserves, due to the changes in oxygen levels (caused by reduced blood flow) and decreased perfusion (13-15). It is also known that brain ischemia is a condition in which there is insufficient blood flow to the brain to meet metabolic demand (16). The ischemia leads to cerebral hypoxia or poor oxygen supply and thus to the ischemic stroke or death of brain tissue (17). Therefore, monitoring changes in the blood flow, tissue morphology, and oxygenation are important for studying vascular physiology (9, 12, 14, 18). One section covered in this dissertation is that a multi-model imaging system is utilized for mouse brain mapping thus it will be beneficial for ischemic stroke study. Stroke is the third leading cause of death and the number one cause of disability in the United States (19). The initial stroke attack often causes regional impairment to brain functions leading to poor quality of life (20). Therefore, understanding the mechanisms underlying the pathophysiology of ischemic brain diseases is of urgent clinical importance. Currently, tissue plasminogen activator (tPA) is the only one therapeutic available as the “clot buster”. However, tPA is only implemented onto a minor percentage of stroke patients (21). Studies focusing on developing clinical therapeutics have been based on neuroprotective rather than strategy of improving vasculature perfusion due to technical limitations. Furthermore, non-invasive technologies capable of elucidating real time macro- and micro-vascular dynamics *in vivo* with a resolution down to capillary level and with a sufficient imaging depth are still not available.

1.2 Current vasculature imaging technologies

Nowadays, several vasculature imaging technologies have been proposed in the biomedical field. For example, based on magnetic resonance imaging (MRI) technique (22), magnetic resonance angiography has been developed to *in vivo* visualize the microvasculatures of biological tissues. Although it could reveal severe blood flow defects in large and medium sized arteries, it cannot image capillaries due to spatial resolution limitation (23). Besides that, the implementation of MRI device is complicated (24, 25). Moreover, as another representative of modern imaging techniques, functional MRI can simultaneously image blood oxygenation level-dependent (the source of contrast in fMRI images). Due to the deoxygenated blood contained in the draining veins, the linear dimension of its physiological spatial resolution is about several millimeters (26). Besides that, it can image blood flow relying on the paramagnetic properties of oxygenated and deoxygenated hemoglobin to visualize change of blood flow in the brain associated with neural activity (27); however, it is costly and difficult to be implemented comparing with some other portable instruments. [14C]iadoantipyrene autoradiography (IAP) has been used as the gold standard for providing blood perfusion information in animal brains (28). But it needs to combine with histological sections to provide 3D information of blood flow, thus, it cannot assess dynamic blood flow in the same imaging subject. Single photon emission computer tomography (SPECT) is a functional imaging technique used to determine blood flow on the distribution of radio-pharmaceuticals (29). Positron emission tomography (PET) is a nuclear medicine imaging technique, which detects gamma rays emitted by the injected radionuclide tracer to produce 3D functional image of biological tissue. This technique is more sensitive than SPECT but the isotope has a shorter half-life and it is costly. In addition, both techniques are limited by their spatial resolution (typically ~1-5 mm), which is not high enough to resolve individual blood vessels (30, 31). Based on detecting injected contrast material, computerized tomography (CT) could produce detailed 3D micro vasculature map. But the injected contrast agent will increase the risk to the imaging subject (32).

Due to the available high imaging spatial resolution (micron scale), more and more attention has been attracted by optical imaging techniques, which could reveal more fundamental details of vascular structure, function, and dynamic changes, such as angiogenesis. For example, single-wavelength optic intrinsic imaging (33) can

qualitatively map the spatial organization of functional activations, though it cannot quantitatively extract comprehensive information including dynamic blood oxygenation and blood flow rate. Confocal (34) and multi-photon (36) microscopies are commonly used techniques which can achieve ultrahigh resolution (~1 μm) imaging. They have been used to map microvasculature (35, 36). However, the imaging depth is only ~300 μm in human skin (36, 37) and mouse cranium is needed to be thinned or removed in mouse brain imaging, which still induces risk to the subjects. Besides, it is not a fluorescent tissue marker free imaging, which makes the experimental operation and results interpretation more complicated. Photo acoustic microscopy (38) can access variances of the parameters, but it is a contacted technology and unpredicted effects could be induced to the imaging samples.

Laser Doppler imaging (39) and single wavelength laser speckle contrast imaging (LSCI) (40, 41) can effectively enables measurement of blood flow rate. Laser speckle contrast imaging was first introduced in the 1980s (42). It is a powerful tool for full-field imaging of blood flow (42). Based on statistically quantification of the fluctuation of speckle pattern, it has found widespread application, as it allows imaging of two dimensional (2D) local changes in blood flow with high spatial and temporal resolution (43-45). However, they are limited to 2D peripheral blood flow mapping (41, 46). Hence, they are unable to detect changes in blood oxygenation. Spectroscopy methods (e.g. near-infrared spectroscopy: NIRs) are capable of determining the changes in the concentrations of hemoglobin based on light absorption differentiation of oxygenated hemoglobin (HbO) and deoxygenated hemoglobin (Hb); however, they cannot detect blood flow (47). Dual-wavelength laser speckle contrast imaging (DW-LSCI) integrates the single wavelength LSCI system and NIRs that enables the imaging of both the relative changes in blood flow and changes in hemoglobin concentration. Dual-wavelength laser speckle contrast imaging has been previously used to investigate functional activation and cerebral ischemia (48, 49) in small animal models. However, these systems require either a filter chopper, or a digital signal for modulating or triggering the light sources; therefore, the temporal resolution is limited to 2 Hz (50), 10-29 Hz (51), 18 Hz (48), and 80 Hz (52) with low spatial resolutions (256×256 pixels). These temporal resolutions are too slow to be sensitive to fast physiological responses, which occur within a few milliseconds (53). Also, the acquired images are interleaved; therefore, a time interval exists between the images acquired from each wavelength. Although interpolation allows the frames to be registered

at the same time point, it adds errors to the measurements. Recently, some multi-mode imaging techniques for blood flow diagnostics have been proposed using a combined fluorescence intravital microscopy, dynamic light scattering, and spectrally enhanced microscopy modalities (54) and MRI (55). However, these methods require the injections of contrast agents, and their temporal resolution is relatively slow.

Therefore, the understanding of the mechanisms underlying the pathophysiology of hypoperfusion in peripheral circulations and ischemic disorders or diseases are limited by the imaging capability in simultaneously monitoring changes of macro- and micro-circulations by extracting full set of parameters down to capillaries deep into the tissue, with non-contact, non-invasive, and *in vivo* manners.

1.3 Laser speckle imaging and optical coherence tomography

Optical imaging techniques are sensitive to several optical parameters, such as scattering and absorption, which if combined with the Doppler Effect (56-58), allow for the measurement of changes of blood flow, concentration of hemoglobin, and morphology of blood vessels. Laser speckle contrast imaging can trace its history back to the 1980s, when a camera was used to obtain a quick snapshot image of a time-integrated speckle pattern. It was advanced in the 1990s for imaging blood flow in the retina and skin with the availability of faster digital acquisition and processing technologies. Based on quantification of the fluctuation of speckle patterns, which are formed by light backscattered from the moving particles (e.g., red blood cells) in typical vessels, LSCI method can provide real-time two-dimensional speckle contrast maps of vasculatures with high-temporal resolution (59). As long as the blood flow is increased, the intensity fluctuations of the speckle pattern will be speeded up in this area. The speckle pattern becomes blurred in the area when integrated over the camera exposure time (2-30 ms) (46, 60-63). Then, the speckle contrast will decrease. A 2-D map of blood flow can be extracted based on a contrast-flow model (46, 60-63). Laser speckle contrast imaging techniques (64-66) are noninvasive techniques and have been widely used to evaluate vascular abnormalities (e.g. blood flow change) in dermatology (67), ophthalmology (68, 69), and neurology (70). Dual wavelength laser speckle contrast imaging (44, 46, 48, 71) is a well-developed imaging modality that has been successfully used to measure rapid changes of blood flow (72-74) and tissue oxygenation (33, 46, 52) with a large field of view.

Using coherence gating, Optical coherence tomography (OCT) is able to use laser sources with broadband to precisely localize light from small volumes, thereby enabling high-resolution imaging of tissue microstructure (75). Optical coherence tomography enables visualization of tissue microstructure in situ and in real time with spatial resolutions in the 1-10 μm range (76-79). Superluminescent diodes (SLDs) are usually employed in OCT systems to enable imaging with 10-15 μm axial resolution. The longitudinal resolution in OCT images is inversely proportional to the optical bandwidth and proportional to the square of the center wavelength of the light source, $\lambda c^2/\Delta\lambda$; hence, ultrahigh resolution OCT requires broad bandwidth $\Delta\lambda$. The spectral region between 1.0 μm and 1.5 μm is of high interest for OCT due to the high penetration depth in biological tissue (80). The particles within the OCT resolution volume can be categorized into three groups: entering or exiting particles, flowing or diffusing, and static (81). As a functional extension of OCT, phase-resolved Doppler OCT (PRDOCT) (82) is developed to extract velocity information of blood flow in functional vessels within the scanned tissue beds, by evaluating phase differences between adjacent A-lines in an OCT B-scan frame. PRDOCT has been applied in imaging, for example, cerebral blood flow (83). The PRDOCT method is of high resolution and high sensitivity to blood flow, however, its imaging performance is greatly deteriorated by characteristic texture pattern artifact, which results from optical heterogeneity of the sample (84); and phase instability due to the sample motion artifacts(85). Being a variation of Fourier domain OCT (86, 87), optical micro-angiography (OMAG) (88) is an imaging technique that can effectively separate moving elements, such as flowing blood cells, from the static scattering elements, i.e., microstructures. It uses the endogenous light scattering from flowing blood cells to produce the imaging contrast, therefore, it is a label-free technique. It is capable of producing 3D images of dynamic blood perfusion within microcirculatory tissue beds with an imaging depth of ~2 mm.

It maps the tissue structure into one image, and maps the blood perfusion into another image whose contrast is based on the velocity of blood flow. Currently, blood flow, typically in the range of ~100-15,000 μm/s (89), can be detected. A sensitivity to blood flow down to 4 μm/sec has been reported utilizing the most recent developed modality called ultra-high sensitive OMAG (UHS-OMAG) (89). With such marvelous sensitivity to the flow, this modality has been successfully employed to image the microcirculations within neovascularization in rodent brain (90), human retina (91, 92) and human skin (89). Optical micro-angiography minimizes problems of sample

movement and noise artifacts typically presented in Doppler OCT by frequency modulation in the interferograms. This reduction in background noise allows visualization of the low perfusion in the capillaries, and creates an image with greater dynamic range of measurement and hence greater contrast.

In general, OMAG is sensitive to functional blood vessel micromorphology (89, 93). Dual wavelength laser speckle contrast imaging system is sensitive to changes in blood flow and the concentration of hemoglobin (94, 95). Therefore, an integration of these two techniques would provide high-resolution 3D imaging of functional blood vessel hymodynamics and metabolism.

1.4 Multi-model technique through integrating dual wavelength laser speckle and OMAG technologies

We develop a novel multi-model imaging technique to simultaneously elicit the aforementioned blood perfusion parameters. The new imaging modality is able to image cerebral microcirculation and blood oxygenation not only in regional bulk tissue but also down to the capillary level. By the use of two complementary metal–oxide–semiconductor (CMOS) cameras, we developed a synchronized DW-LSCI (SDW-LSCI) system which can simultaneously acquire reflectance images backscattered from a sample illuminated by lights at two wavelengths (λ1: 780 nm and λ2: 825 nm), necessary for tissue oxygenation evaluation. The frame rate ranges from 100 Hz to 500 Hz for ~1000 × 1000 pixels (pixel size 12 μm×12 μm), enabling acquiring images at both wavelengths simultaneously with a higher spatial and temporal resolution than prior reported systems (48, 51, 52, 71, 96). We demonstrated the applicability of the dual wavelength laser speckle contrast imaging system by imaging the relative changes of the blood flow as well as the changes in the concentration of HbO, Hb and HbT in an experimental stroke model. We also integrated the SDW-LSCI system with OMAG system and take advantage of mutual complementarities to provide full set of information of tissue response in 2D and 3D. The newly developed multi-model system is capable of providing a non-invasive, non-contact, high resolution, high sensitivity, and high efficiency technology for evaluation of multiple hemodynamic and metabolic parameters along the time course of the disease and the effectiveness of treatment. These advantages will greatly improve the research based on other imaging techniques and investigation of mechanisms of microvascular response to tissue injury *in vivo*.

This thesis mainly addresses an understudied area in tissue injury, including the vascular function in wound healing and brain ischemia. The mechanisms for tissue injury, such as brain injury, to repair remain unclear. Blood flow plays a rescuing role to supply oxygen and nutrients immediately onto the injury, followed by a long period of recovering time, and the whole procedure is accompanied by vessel angiogenesis and remodeling (97). A better assessment of the microvascular dynamics and tissue oxygen consumption during pathophysiological conditions will be beneficial to understand the mechanisms of tissue injury (98).

In preclinical study, the multi-model optical systems can aid in the study of mechanisms linking vascular function to disorders or diseases. We can investigate the mechanism by which ischemia alters neuronal structure and function resulting in neurovascular disease.

Pre-clinical studies on animal models for testing novel approaches and treatments could provide opportunities to early diagnose diseases and develop potentially useful clinical therapeutics. For example, various neurovascular diseases, such as stroke, are probably initiated by low blood supply with embolism or embolism alone (99, 100). Our studies could help in diagnosing stroke at its early stage by determination of the abnormalities of vasculature before the onsite of the disease. They could also expedite the design and assessment of therapies to improve vascular function in disorders or diseases. Therapeutic interventions, such as epoxyeicosatrienoic acids, which can induce vasodilatation endogenously in human, are devoted to improving hypoperfusion, and are considered the most promising treatments for stroke at its early stage. Therefore, not only for investigation of mechanisms, but also for monitoring the treatment effect after inducing therapeutic intervention to control or slow the progression of neurovascular diseases (e.g. stroke, migraine, traumatic brain injury, and vascular dementia in human), a multi-model imaging system is highly demanded.

1.5 Organization of the Dissertation

The goal of this research is to investigate the use of a multifunctional optical imaging system to investigate hemodynamic responses to tissue injury *in vivo*. The research encompasses technology development and preclinical applications, which required an interdisciplinary approach to problem solving. The key personnel who collaborated on this research are listed in the acknowledgments.

In this dissertation, Chapter 1 provides the basic background, theory and system level overview for the synchronized dual wavelength laser speckle system and optical microangiography system currently in use in the BAIL. Chapter 2 covers the design and optimization of the 1st generation multifunctional system. The system characteristics are presented. This chapter also describes the investigation of the 1st generation system to non-invasively assess early biological changes in injured tissue. Chapter 3 covers a speeded up 2nd generation multi-model imaging system and its utilization in monitoring response of tissue injury. Chapter 4 demonstrates that the newly developed 2nd generation system could qualitatively and quantitatively differentiate the degree of injury in a stroke mouse model. The results suggest the system can be used to monitor both morphological and functional information near and in the ischemic regions in the mouse brain subjected to middle cerebral artery occlusion.

Chapter 2. Development of a 1st generation multi-model imaging system capable of providing hemodynamic and morphological information of microcirculatory tissue beds *in vivo*

This chapter is a description of the construction of the 1st generation combined multi-model imaging system that can simultaneously image blood flow, blood oxygenation, and vascular remodeling in small animal models. The integrated system that incorporates a dual wavelength laser speckle imaging system and ultra-high sensitive OMAG system can provide the aforementioned parameters of the injured tissue response. Briefly, the DW-LSCI system can provide a large field-of-view of blood flow, blood oxygenation information at fast imaging speed. The OMAG can provide the depth-resolved blood vessel remodeling response information with high spatial resolution and high flow sensitivity.

2.1. Development and validation of the 1stG multi-model imaging system

As the huge dataset scanned by high sensitivity and high resolution optical imaging (e.g. OMAG) over a whole

organ (e.g. mouse ear flap, or mouse brain) induces inevitable burden for the imaging implementation, a fast, synchronized and large field of view optical imaging technique is required to localize the exact injured region core of the tissue and then guide the OMAG for subtleties investigation.

The 1stG DW-LSCI system is utilized to monitor the hemodynamic response in experimental stroke. The 1stG multi-model imaging system is finally utilized to differentiate the wound-healing process in the wound core, bilateral, upstream, and downstream of the tissue wound (101).

2.1.1. DW-LSCI system and method for attaining flow and oxygenation

2.1.1.1 1stG DW-LSCI system configuration

The DW-LSCI system (shown in the right part of Fig. 1) contains two single-mode laser diodes with a wavelength of λ1 = 780-nm (30 mW) and λ2 = 825-nm (30 mW). The lasers are modulated with an optical chopper at a frequency of 2 Hz, such that only one laser wavelength is selected at a given time. The two laser beams are aligned via a beam splitter such that they illuminate the same surface area of the sample. The incidence of the laser beam is set at a 30 ° angle from the tissue surface (102) to minimize specular reflection. The diffusely reflected light from the tissue is detected with a CMOS camera (Basler A 504k, 1280×1024 pixels) through a zoom lens, which provides an adjustable magnification. The speckle size (>~19 μm) can satisfy the requirement that the speckle size must be larger than twice of the size of the camera pixels (~8.5 μm) (103) (see *Equation 1*), which maximizes the contrast of the speckle patterns (40, 104). This is achieved by setting a magnification of 2.5 and imaging a field of view of ~4× 4 mm^2. The scanning protocol of the system is shown in Fig. 4 (A). The camera exposure time was set to ~10 ms, to render high contrast images with sufficient dynamic range for speckle flow imaging (48, 102). The contrast to noise ratio is high at 5 ms-10 ms exposure time (40, 44, 105). The DW-LSCI system captures 500 frames for each dataset. The frame acquisition frequency is set to 2 Hz; therefore, it takes ~4 min to capture a data set. The speckle contrast sensitivity of particle dynamics via camera exposure time over decorrelation time is shown in Fig. 2 (40, 105): T is camera exposure time; τ_c is decorrelation time of flow particles in the flow sample. At the point that T=τ_c, the

speckle contrast sensitivity is maximum. We experimentally tested the system spatiotemporal resolutions and flow sensitivities using flow phantom (shown in Fig. 2). (101)

$$\rho_{speckle} = 2.44\lambda(1 + M)f_n \quad [1]$$

where $\rho_{speckle}$ denotes the speckle size, λ is the wavelength of light, M is the magnification of the imaging system, and f_n is the f number of the system. Overall, an optical imaging system is developed to first localize the exact injured region core of the tissue and will be utilized for guiding OMAG to investigate the subtleties of tissue injury.

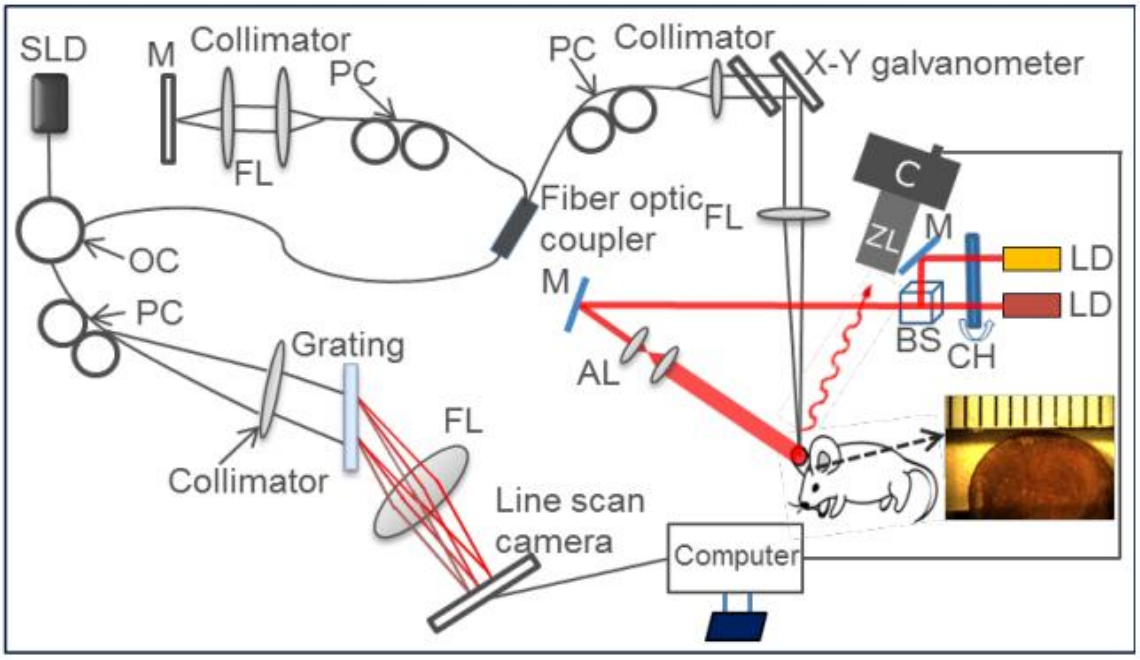

Figure 1 Schematic diagram of the multi-model optical imaging system. SLD: super-luminescent diode, OC: optical circulator, PC: polarization controller, FL: focusing lens, LD: laser diode, CH: chopper, M: mirror, BS: beam splitter, AL: adjusting lens, C: camera, ZL: zoom lens. The insert is a photo of the mouse pinna. Each division on the ruler is 1 mm. (101)

One of the characteristics of the system is that the light sources (780 nm and 825 nm) of the system are modulated by an optical chopper to interactively illuminate onto the sample, and subsequently backscattered from the sample and received by the camera. The speckle size is considered large enough if the static sample has the value of speckle contrast ~0.9, tested by a white static plate. The spatial resolution (Fig. 2(a)) of the laser speckle system is ~ 7.2 μm,

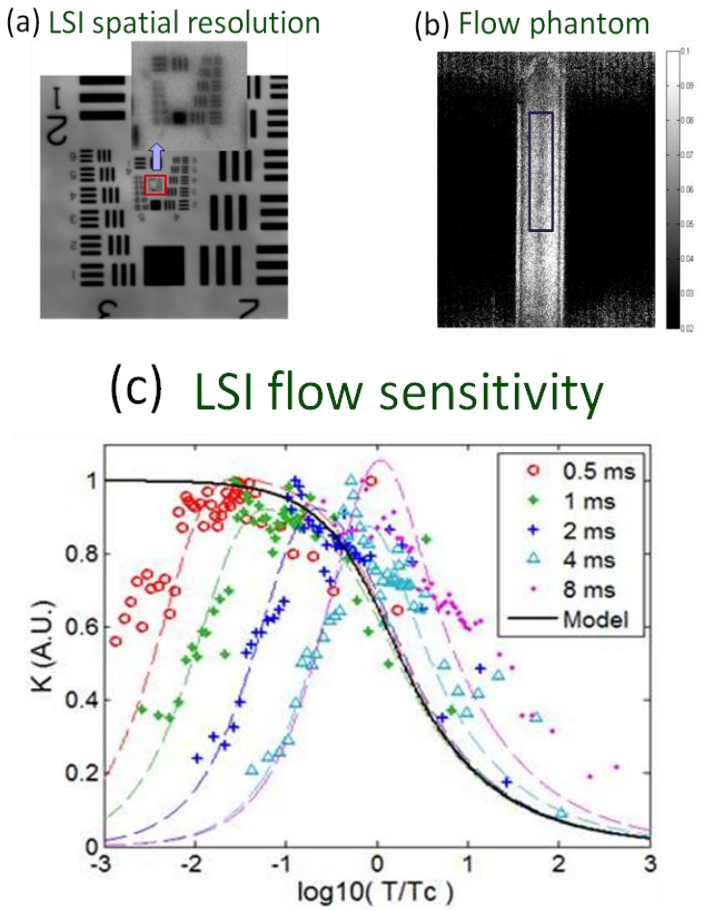

Figure 2 System performances: resolutions and sensitivities. (a) LSCI system spatial resolution: ~7.2 μm; (b) Speckle contrast image of the flow phantom; this experiment is used for flow sensitivity and temporal resolution testing. The tubing diameter is ~1.00 mm, and the solution is diluted 2% milk. The tubing is driven by a syringe pump. (c) LSCI system flow sensitivity and model of the contrast via the ratio of exposure time/decorrelation time. From this figure, we can estimate that the flow sensitivity of the LSCI system is ~30 μm/s, and exposure time has influence on the contrast values in the low flow range: 0-1000 μm/s.

which was tested by imaging the USAF RES Target (resolution test pattern). The highest temporal resolution is 2 ms (frame rate 500 fps) and flow sensitivity is ~30.0 μm/s, tested by tubing phantom flow driven by a syringe pump (Harvard Apparatus Model 55-1111).

2.1.1.2 Methods for attaining the large field of view DW-LSCI flow and oxygenation images

Speckle pattern remains constant over time as long as a laser beam is illuminated into a static tissue. However, when there are scattering particles that are in motion, e.g., RBC moving in a patient's blood vessels, it leads to time-varying fluctuations in light intensity, resulting in dynamic speckle. As long as the camera has sufficient temporal response to record the time-varying speckle, the spatial or temporal speckle contrast can be used to visualize the dynamic blood flow (46). The speckle contrast K_t at pixel *(x, y)* is calculated by *Equation 2*, in the case of temporal contrast method in which a series of N frames are recorded over a time period of T (106):

$$K_t(x,y) = \frac{\sigma_t(x,y)}{\langle I(x,y)\rangle} = \frac{\sqrt{\frac{1}{N-1}\{\sum_{i=1}^{N}[I_i(x,y) - \langle I(x,y)\rangle]^2\}}}{\langle I(x,y)\rangle} \quad [2]$$

where σ_t is the temporal standard deviation, $\langle I(x,y)\rangle$ is the mean intensity of pixel (x,y) over *N* frames, $I_i(x,y)$ is the light intensity recorded by the camera at the i'th frame (i=1, 2, …N). This method is simple and efficient, though it has limitation in providing optimal treatment to suppress the background scattering signals from the static elements, leading to reduced visibility of small blood vessels, in particular the capillaries (shown in Fig. 3). Thus, we proposed an alternative analysis method to contrast blood flows. For achieving better contrast, we first perform a division operation on adjacent images, i.e., $D_i(x,y) = [I_i(x,y)]/[I_{i+1}(x,y)]$. This operation of division emphasizes the scattering particles in motion, as the diffuse reflectance of background static tissue recorded by the camera remains relatively constant. We then calculate the differences between two consecutive division images, $\Delta D_i(x,y) = [D_i(x,y) - D_{i+1}(x,y)]/2$ (107). Due to static tissue elements on one hand and an increased highlighting of fine changes between adjacent frames on the other, this computation suppressed the background signals (107). Finally, we use standard deviation $\sigma_m(x,y)$ to extract blood flow contrast in the resulting mLSCI images:

$$\sigma_m(x,y) = \sqrt{\sum_{i=1}^{N} \frac{[\Delta D_i(x,y) - \Delta D_m(x,y)]^2}{N-1}}$$

[3]

where $\Delta D_m(x,y)$ *is* the means of difference: $\Delta D_m(x,y) = \frac{1}{N}\sum_{i=1}^{N} \Delta D_i\,(x,y)$ *(107).*

The aforementioned method was aimed to enhance the contrast (shown in Fig. 3). However, for the flow velocity measurement, we use the spatial contrast, which was calculated as the ratio of standard deviation *(σ_s)* to the mean intensity of each binning window <*I*>. A five by five pixel binning window was applied on the raw image to reduce noise. The relationship between the speckle contrast and the dynamic features of the speckles is expressed in Equation 4, where the relative change of blood flow is derived from the model reported in (40, 44).

$$K = \frac{\sigma_S}{\langle I \rangle} = \left\{ \frac{\tau_C}{T} + \frac{\tau_C^{\,2}}{2T^2}\left[\exp\left(-\frac{2T}{\tau_c} \right) \text{-1} \right] \right\}^{0.5}$$

[4]

where *T* is exposure time of the camera; τ_c is the correlation time which is assumed to be inversely proportional to a measure of the velocity of the scattering particles.

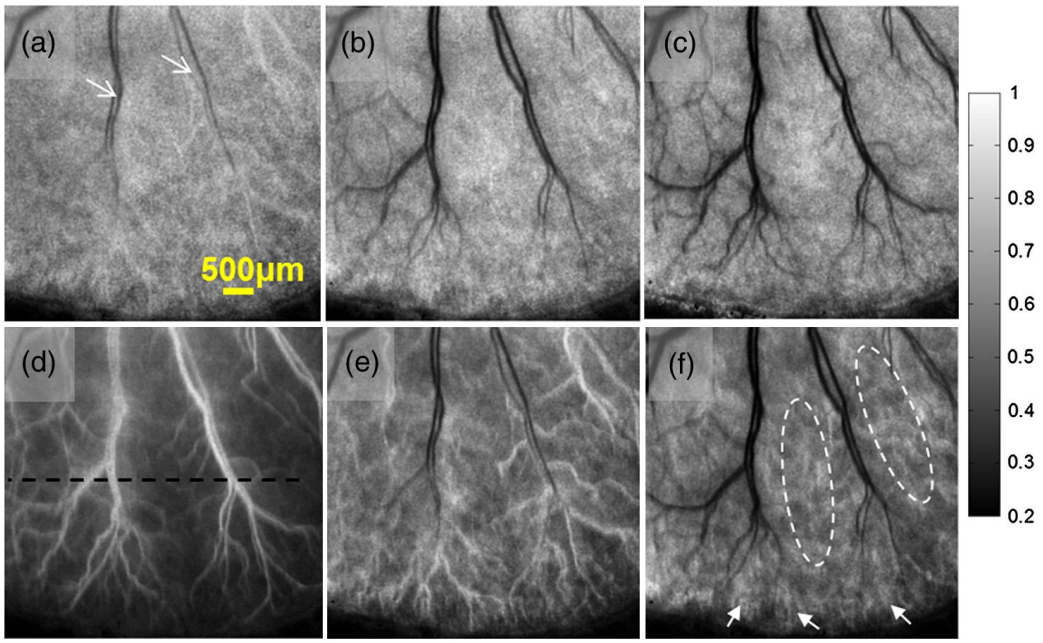

Figure 3 Resulting images from temporal contrast *Kt* (top row) and the corresponding motion enhanced contrast σ_m (bottom row) for the exposure time of (a, d) 4 ms, (b, e) 10 ms, and (c, f) 40 ms, respectively. (107)

The relative blood flow change could be resolved through calculating the relative flow velocity change. Different concentration of HbO and Hb can generate modulation to the backscattered light intensity captured by the cameras. According to Beer-Lambert law, the relationship between the concentrations of HbO and Hb could be presented by Equation 5 (108, 109).

$$ln\left(\frac{I^{\lambda_i}}{I_o^{\lambda_i}}\right) = \varepsilon_{HbO}^{\lambda_i} C_{HbO}^{\lambda_i} L_{\lambda_i} + \varepsilon_{Hb}^{\lambda_i} C_{Hb}^{\lambda_i} L_{\lambda_i} \quad [5]$$

where $ln\left(\frac{I^{\lambda_i}}{I_o^{\lambda_i}}\right)$ is called the absorbance. ε is the molar spectral absorbance coefficient of an absorbing chromophore; I^{λ_i} is the light intensity of different wavelengths at a specific measurement time point. L_{λ_i} is the path length of the light inside the medium. Because the two wavelengths we chose are very similar, the path lengths of two different lights can be assumed to be the same (110, 111) and could be estimated to ~1.5 mm through Monte Carlo simulations (112). As the two lights is coupled by a fiber, the lights will be evenly illuminate onto the sample, with the same initial light power, $I_0^{\lambda_i}$, initial light intensity of the two-wavelength light evenly illuminated to the mouse brain, will be considered as the same. If we use three wavelengths, different combination of the captured

images of different wavelengths will produce two equations with two variables based on Equation 5, through which the concentration of *HbO* and *Hb* could be resolved. The total hemoglobin concentration can be obtained from *HbT=HbO+Hb* and is assumed to be linearly proportional to the local blood volume (48). To reduce the speckle noise, ten frames will be first averaged before the calculation. For the hemoglobin images, no spatial averaging will be used. Here, we use two wavelengths to compute changes in the concentration of *HbO* and *Hb*, which can be measured through diffuse reflectance due to the changes of light absorption. Equation 6 is a model based on the Beer-Lambert law (48, 110) which extracts the concentration changes of *HbO* and *Hb*.

$$\begin{bmatrix} \Delta HbO(t) \\ \Delta Hb(t) \end{bmatrix} = \begin{bmatrix} \varepsilon_{HbO}^{\lambda_1} & \varepsilon_{Hb}^{\lambda_1} \\ \varepsilon_{HbO}^{\lambda_2} & \varepsilon_{Hb}^{\lambda_2} \end{bmatrix}^{-1} \begin{bmatrix} \dfrac{\ln\left(R_{\lambda_1}(0) \big/ R_{\lambda_1}(t)\right)}{L_{\lambda_1}} \\ \dfrac{\ln\left(R_{\lambda_2}(0) \big/ R_{\lambda_2}(t)\right)}{L_{\lambda_2}} \end{bmatrix} \quad [6]$$

where ε is the molar spectral absorbance coefficient of an absorbing chromophore; $R_{\lambda_1}(t)$, $R_{\lambda_2}(t)$ are the measured diffuse reflectances at the two wavelengths after the wound; $R_{\lambda_1}(0)$ and $R_{\lambda_2}(0)$ are the baseline diffuse reflectance values prior to the wound. L_{λ_1} and L_{λ_2}, are the path lengths of the light inside the medium and assumed to be constant, time-invariant and equal to ~1.5 mm (110, 111). The change in total hemoglobin concentration can be obtained from *ΔHbT=ΔHbO+ΔHb* and is assumed to be linearly proportional to the local blood volume (48).

2.1.2 UHS-OMAG system for high resolution 3D microvascular networks imaging

Based on coherence gating and frequency domain Optical coherence tomography (FD-OCT), OMAG is able to select the backscattered photons from the moving blood cells for image remodeling. The axial and lateral resolutions of OMAG are dependent on the light bandwidth (source coherence length) and the numerical aperture of the objective lens, respectively.

2.1.2.1. OMAG system configuration

As shown in Fig. 1 (left part), a superluminescent diode with a central wavelength of 1310 nm and a bandwidth of

65 nm is used as a light source, which yields an axial resolution of ~9 μm in the tissue (113). The light from the light source was divided into two paths through a 2×2 optical coupler, one for the reference arm and the other for the sample arm. In the sample arm, the light was coupled into a custom-designed optical system, containing a collimator, a pair of galvo mirrors, and an objective lens with a 50 mm focal length. This design of the optical system provided a ~16 μm lateral resolution (113). The depth of field (DOF) is about 200 μm. The lights backscattered from the sample and reflected from the reference mirror are recombined using the 2×2 optical coupler, and then transmitted to a home-built spectrometer via an optical circulator for the detection of the spectral interference signal. The spectrometer has a spectral resolution of 0.141 nm, providing an imaging depth of 2.22 mm into the sample. A high speed InGaAs line scan camera (SUI, Goodrich Corp) is used in the spectrometer to capture the interferograms at a recording speed of 92,000 A-lines per second. With this imaging speed, the system's sensitivity has been determined to be 105 dB at a depth position of 0.5 mm from the zero-delay line. A scanning protocol which yields fast imaging speeds was utilized. The scanning protocol of the system is shown in Fig. 4 (B). Briefly, a saw tooth waveform is used to drive the x-scanner (for fast B scan) and a step function waveform is used to drive the y-scanner (for a 3D scan). Along the x-scanning direction, 256 A-lines are captured at ~8 μm spatial interval between adjacent A-lines to achieve one B-scan cross-sectional image, which covers a range of ~2 mm on the sample. The duty cycle for the rising side of the saw tooth waveform is set at ~80% per cycle, which provides a B-scans frame rate of ~280 fps. For the y-scanning direction, the 2 mm scan range is evenly divided into 200 steps with a 10 μm spatial interval between them. In each step, ten frames are captured and processed to extract one B-scan cross-sectional flow image (89). The system acquires 2000 frames to form each three dimensional dataset. The total time for acquiring one 3D data set takes ~7 seconds, which is suitable for *in vivo* detection. Twenty datasets can be sequentially acquired in different regions and stitched together to obtain a wide field image that covers an area of ~12×8 mm.

2.1.2.2. Methods for attaining the high spatial resolution UHS-OMAG images

Motion artifacts might be generated from involuntary movement as long as UHS-OMAG system is able to pick up small-scale velocity changes. To solve the problem, a new scanning protocol is introduced in order to achieve faster imaging speed than that was used in our previous work (89). In order to image the slow blood flow within capillary vessels while keeping the imaging time at the same order as the conventional approach, the method is performed by decreasing A-line density in one B-scan, while increasing B-scan density (89).

Briefly, a saw tooth waveform was used to drive x-scanner (for fast B scan); a step function waveform was operated

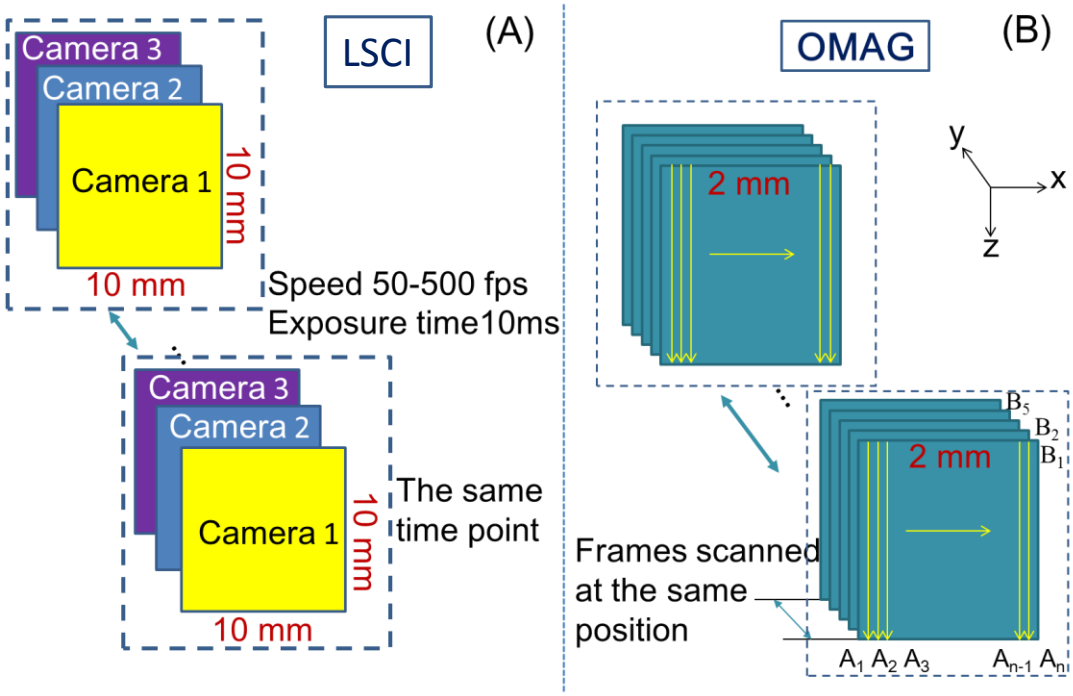

Figure 4 Schematic of imaging protocols of (A) DW-LSCI and (B) OMAG systems. DW-LSCI system captures the frames similar to taking snapshots. The speckle pattern fluctuation images are first acquired by the CMOS camera, and then analyzed statistically. OMAG B scan cross section image (x-z direction) is composed by thousands of A lines, and then hundreds of B scan cross section images are acquired along the y direction (C scan) to finally achieve a 3D image.

for the y-scanner. To achieve one B-scan cross-sectional image, 128 A-lines, along x-scanning direction, are captured with a 15 μm spatial interval between adjacent A-lines. The B-scan cross-sectional image covers a range of 2 mm on the tissue. The speed for B-scans is determined at 280 fps when the duty cycle for the rising side of the saw tooth waveform is set at 75% in one cycle. As to the y-scanning direction, the 2 mm scan range is evenly divided into 200 steps with a 10 μm spatial interval. At each step, five frames are captured and processed to extract

one B-scan cross-sectional flow image (89). The B-scan cross-sectional flow image is extracted by applying OMAG algorithm on C-scan direction (elevational direction), rather than B-scan direction (lateral direction) as in the conventional approach (114). We can use a time interval between adjacent B-scans at 3.3 ms to achieve a flow sensitivity close to 4 μm/s (115). The total time for acquiring each 3D data cube takes only 3.6 seconds, which is suitable for *in vivo* detection.

In the following section, we will show that the different depth 2D *en face* images and 3D volume images afforded by the UHS-OMAG imaging datasets can be manipulated to directly examine in details the appearance of the blood vessel networks under normal and diseased conditions.

2.1.2.3 *In vivo* volumetric imaging of microcirculation within human skin under psoriatic conditions using Optical microangiography (116)

Vascular abnormalities may play an important role in dermatologic diseases, such as psoriasis and skin cancer. A non-invasive imaging modality capable of assessing 3D microcirculations within skin tissue beds *in vivo* is needed, that can improve our understanding of vascular involvement in these skin conditions. In this section, we aim to demonstrate the feasibility of using UHS-OMAG to visualize skin microcirculations in 3D. We will also quantify microvascular density under normal and psoriatic conditions *in vivo*.(116)

The UHS-OMAG system works at 1,310 nm wavelength for *in vivo* imaging of microcirculation in human skin. At this time, the system has an axial resolution of 10 μm and lateral resolution of 20 μm. We set the frame rate at 280 fps to acquire 3D imaging dataset. The 3D dataset encompasses morphology and capillary level microvascular blood perfusion within the scanned skin tissue volume. Using this system, we performed imaging experiments on the plaque type psoriatic skin of a volunteer.

Blood vessel elongation and the denser network are shown in the 3D images acquired from the psoriatic lesion skin compared with normal skin. The Statistical analyses demonstrate that higher blood vessel density was presented within the psoriasis lesion skin. UHS-OMAG can be a valuable tool for imaging skin microcirculations non-invasively with high speed and high-sensitivity. Therefore, it may play an important role in future clinical diagnosis and treatment of dermatologic diseases such as psoriasis. (116)

2.1.2.3.1. Background and significance

Approximately 2% of the population in western countries is affected by psoriasis, which is a chronic, inflammatory skin condition (117). The prominence of dermal microvascular expansion in lesion skin has been demonstrated and that psoriasis is angiogenesis-dependent was suggested in previous studies (118). A non-invasive imaging means is needed to assess abnormality of blood circulation conditions within the tissue beds of human skin. As long as the imaging tool of high resolution and high sensitivity to blood flow is developed, the capillary vessels can be resolved within human skin. Nowadays, there are several technical methods available for imaging the macro- and micro-vasculatures within human skin in vivo. Capillaroscopy and videocapillaroscopy (119, 120) are considered reliable ways to perform microvascular analyses. However, they can only provide capillary morphology within a very superficial layer, less than100 μm. Here, we demonstrate the utility of the UHS-OMAG in assessing subcutaneous vasculatures within normal and diseased skin tissue beds in vivo. We show that UHS-OMAG is capable of distinguish the microcirculation network within the psoriatic skin from that in healthy skin. The results show the promising utilities of UHS-OMAG imaging modality in pre-diagnosing skin diseases, such as psoriasis. (116)

2.1.2.3.2. Material and methods

The schematic of the imaging system setup is similar to that shown in Figure 1 (left), which is similar to the one reported in Ref. (89). As aforementioned, the system is illuminated by a superluminescent diode light source with a central wavelength of 1,310 nm and a bandwidth of 65 nm that yields an axial resolution of 10 μm in air. The light power of the beam incident upon the skin was 3 mW, which is below the safe occupational exposure level established by the American National Standards Institute (ANSI Z136.1) (121). This design of the optical probe could provide a 20 μm lateral resolution for skin imaging. Here, the spectrometer has a designed spectral resolution of 0.141 nm, providing an imaging depth of 2.22 mm into the sample (assuming the refractive of the skin is 1.35). The system sensitivity has been determined at 105 dB at a depth position of 0.5 mm, with a high speed InGaAs line scan camera employed in the spectrometer to capture the interferograms at a recording speed of 47,000 A-lines per second. With these setups, the system sensitivity to the blood flow is determined to be within a range of 4-22.2 μm/sec. Such sensitivity is sufficient to image the capillary blood vessels within skin tissue beds. The imaging is

done through air without any contact to the subject, as long as the optical probe is situated 30 mm above the skin of interest.

We performed the measurements on a young male volunteer with a stable psoriasis plaque located at the front region of the right elbow. The experimental procedures were in compliance with the Helsinki Declaration of 1975, as revised in 2008. With the forearm positioned under the optical imaging (shown in Fig. 5 (A)), the volunteer was comfortably seated during imaging. The normal skin and lesion skin areas examined by the UHS-OMAG system are shown in Fig. 5 (A). A photograph is taken from the subject, shown in Fig. 5 (C). The psoriasis lesion skin appears reddish, indicated by the white arrow. The tested area (marked by red square 2) was randomly selected. It covered a surface area of 2 mm by 2 mm on the lesion skin. A normal skin area of 4 mm^2 (marked by the yellow square 1) was also randomly selected in the region that is close to the lesion region. (116)

Twenty different positions in total (2 mm x 2 mm for each) were randomly selected for UHS-OMAG imaging, 10 of which from the areas bearing the psoriasis lesion skin and the other 10 from the normal skin adjacent to the psoriasis lesion. (116)

2.1.2.3.3. Results

Figure 5 (B) shows a schematic drawing of microcirculation within human skin. Referring to the histopathology (122, 123), the dermal vasculature encompasses of two major horizontal vascular networks. The networks include the deep reticular vascular plexus lying near the dermal/hypodermal interface in the dermis and the superficial papillary vascular plexus lying at the junction between the epidermis and the vascularized dermis. (116) The two layers of plexuses are linked by the communicating blood vessels which are oriented perpendicular to the plexuses (122).

The results are discussed in relation to the differences of blood vessels between the lesion and normal skins. Typical B-scan cross-sectional structure images were captured from the areas (shown in Fig. 5 (C)), representing the normal and the lesion skins, respectively. The UHS-OMAG algorithm was extracted and highlighted the functional vessel morphology. It is obvious that the papillary vessels in the lesion skin (marked by the red arrows) appeared more abundant and much longer than those in the normal skin (marked by yellow arrows). (116) All the results

demonstrated here and the following part are based on a single human subject study.

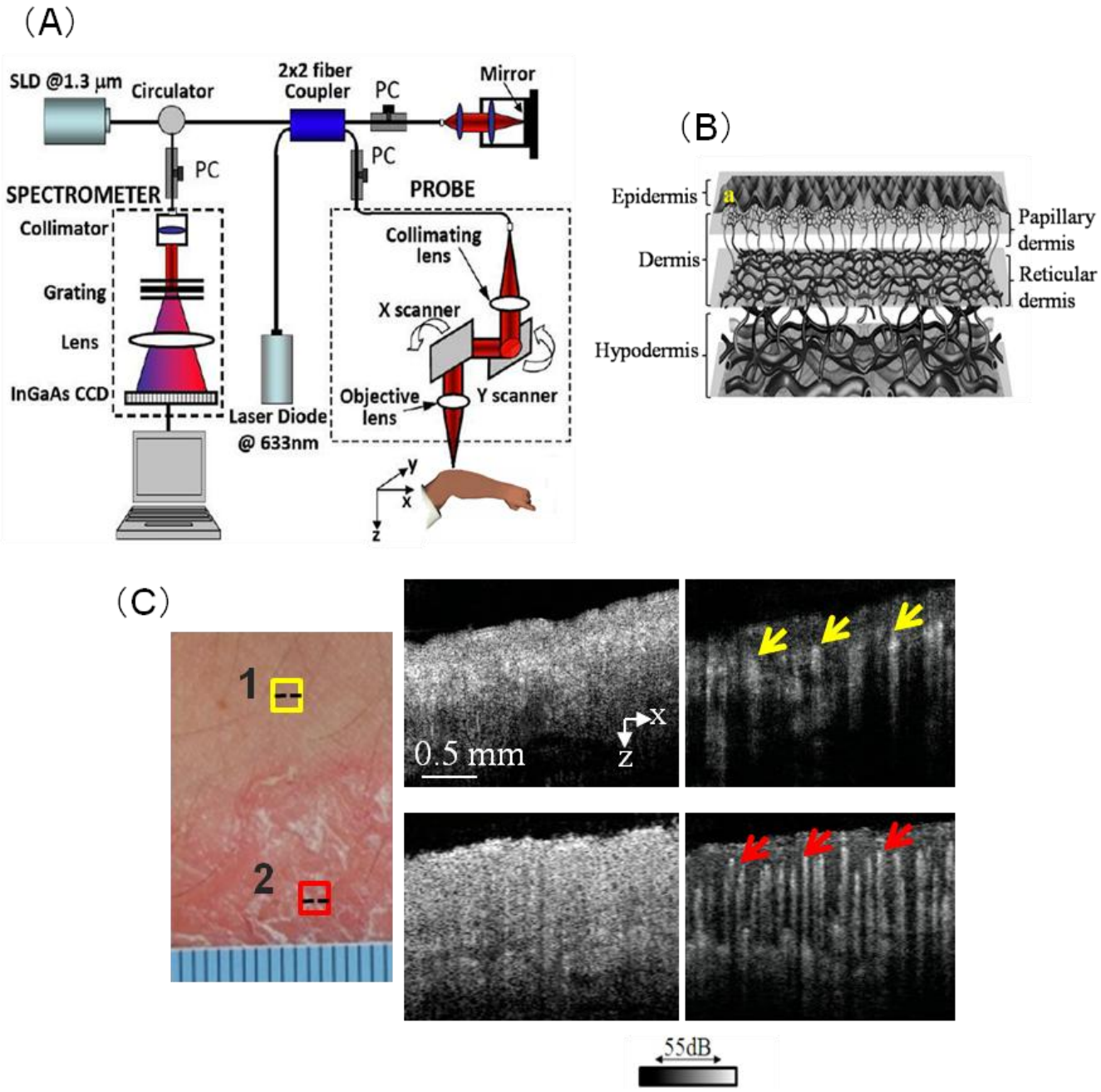

Figure 5 (A) Schematic of UHS-OMAG system. SLD, superluminescent diode; PC, polarization controller; CCD, charge-coupled device. Measurements were performed on a stable psoriasis plaques located in the antecubital skin of a 33 year-old male volunteer. (B) Schematic of microcirculation network within human skin, which structurally contains of three

layers marked as epidermis, dermis, and hypodermis. The dermis consists of papillary layer and reticular layer. (C) Photograph shows the regions of interest selected for UHS-OMAG imaging. The yellow square indicates an area of the normal skin (1), and the red square of the psoriasis lesion (2). Typical OMAG B-scan images taken from the regions of interest: Representative B-scan structural and the corresponding blood flow images obtained from the normal skin area (b, c) and from the psoriasis lesion skin area, respectively. The yellow arrows and red arrows indicate some representative blood vessels. (116)

The expanded superficial microvessels in psoriasis lesion are located close to the epidermis. Volumetric visualization of tissue morphology and micro-vasculature can be made available for both the normal and lesion skin, by combining together the cross-sectional flow images with sequential structural images. (116) Fig. 6 (A) illustrates the representative *en face* images at different depth positions (each column for the same depth) extracted from the volumetric blood flow images of the normal skin (the upper row) and the psoriasis lesion skin (the lower row), respectively. (116) The columns in Fig. 6 (A) correspond to the depth (measured from the surface of the skin) of 210 μm [(a) and (e)], 340 μm [(b) and (f)], 530 μm [(c) and (g)], 720 μm [(d) and (h)], respectively, from the surface to deeper tissue of skin. The microcirculation within the lesion skin demonstrates a totally different pattern from that within the normal skin through comparison. Almost no functional blood vessel networks could be observed at 210 μm depth within the normal skin. It indicates that this depth layer belongs to the epidermal layer due to that no blood vessel anatomically in the normal epidermal layer (123). Different with Fig. 6 (A)a, Fig. 6(A)e demonstrates the dense bright spots of blood vessels at the same depth, which indicate the papillary loops at the junction between the epidermis and the dermis. It implies that the epidermal layer of the lesion skin is thinner than that of the normal skin. Fig. 6(A) b shows the capillary loops at the depth of 340 μm within the normal skin. Some representative papillary loops are marked by 1. Connecting the dermal arterioles and venules by forming capillary loops in the papillary plexus, those papillary loops lie horizontally through the papillary layer due to the elongation and microvascular angiogenesis (124), the papillary vessels in the lesion skin are represented as bright spots [marked by 2 in (e) and 3 in (f)] in a depth of region from 210–340 μm. Fig. 6 (A)c, g exhibits the superficial reticular perfusion maps from the normal and lesion skin at the same depth (530 μm), respectively. The vessel density in the lesion skin appears larger than that in the normal skin shown in Fig.6 (A) c, probably due to angiogenesis. We also visualized angiogenesis through comparing Fig. 6 (A) d with h, which represent the deeper reticular vessel networks within the normal and lesion skin at the same depth, respectively. The overlaid 3D view of

normal skin and lesion skin is shown in Fig. 6 (B). This 3D view demonstrates that papillary loops appeared elongated in the psoriasis skin. Moreover, the blood vessel in the lesion skin is much denser than that in the normal skin. (116)

The blood vessel density (BVD) was computed as a quantitative metric for comparing blood vessel patterns within normal and psoriatic skins. Here, BVD was defined as the ratio of the blood vessels area (BVA) to the total area of the tissue slice, the B-scan structure area (SA). By setting a threshold value of 15 dB to eliminate the noise effect on the calculations, B-scan images, including blood flow images and corresponding microstructural images, were converted into binary images. Afterwards, BVA and SA were determined by the pixel numbers of binary image of blood flow and the corresponding structural image, respectively. Finally, the BVD value was calculated using the function:

$$BVD = BVA/SA \quad [7]$$

For statistical analysis, twenty different regions of skin areas (each of 2 mm x 2mm) were randomly selected and examined. Ten was selected from the psoriasis lesion skin and the other ten from the normal skin. We generated two groups of BVD values: the first one was from psoriasis lesion skin; the second one i from the normal skin. For each group, we elicited fifty BVD values. Fig. 6 (C) shows the histogram distribution of the BVD values. By fitting the experimental data to the normal distribution function, the normal distribution bell-curves were evaluated. It is noticible that both the distributions of the BVD values from normal skin (blue bars) and lesion skin (red bars) approximately follow the normal distribution. The null-hypothesis and alternative hypothesis were used to statistically evaluate the difference of BVD within the normal skin and the lesion skin. The null-hypothesis H_0 is that the mean value of BVD values obtained from the psoriasis lesion skin is not significantly different from those from the normal skin. The alternative hypothesis H_A is that the mean value of BVD values obtained from the psoriasis lesion skin is significantly larger than those from the normal skin. Using Student's t-test test, the difference between blood vessel densities in normal and psoriasis human skin with was found to be significant with P-value <0.001. The bar graphs of BVD values for the normal skin and psoriasis lesion skin are shown in Fig. 6 (D). From the graph, the BVD of normal skin (0.3687 ± 0.0422) is significantly smaller than that of the psoriasis lesion skin (0.5286 ± 0.0603).

Here,it indicates that UHS-OMAG is capable of differentiating the blood vessel network within the normal skin from that in the psoriatic skin conditions. We can use cross-sectional image (B-scan frame) and representative volumetric images to visualize differences of microcirculation between the normal skin and lesion skin. The *en face* images in Fig. 5 (A), i.e., the x–y plane views at different depths are used to examine changes of blood vessel appearance within the psoriatic lesion skin. Eongated blood vessels and high BVD appear in the psoriatic skin, which is not observed in the normal skin. Overall, UHS-OMAG imaging modality is able to provide depth resolved information. Also, it has the capability to create volumetric vascular images with high resolution and high sensitivity, without using any contrast agents. The results showed that the BVD in the psoriasis lesion skin was statistically significant difference from that in the normal skin. (116)

2.1.2.3.4 Summarization

In this section, we have demonstrated that the UHS-OMAG imaging system has adequate sensitivity and imaging speed to image the volumetric microcirculation within the human skin *in vivo*. The different depth 2D en face images and 3D volume images afforded by the OMAG imaging datasets can be manipulated to directly examine in detail the appearance of blood vessel networks under normal and diseased conditions. The BVD in the psoriasis lesion skin has a statistically significant different appearance when compared to that in the normal. Hence, we expect that the UHS-OMAG to have a great value in the future in clinical diagnosis and treatment assessment in human skin disorders and diseases.(116)

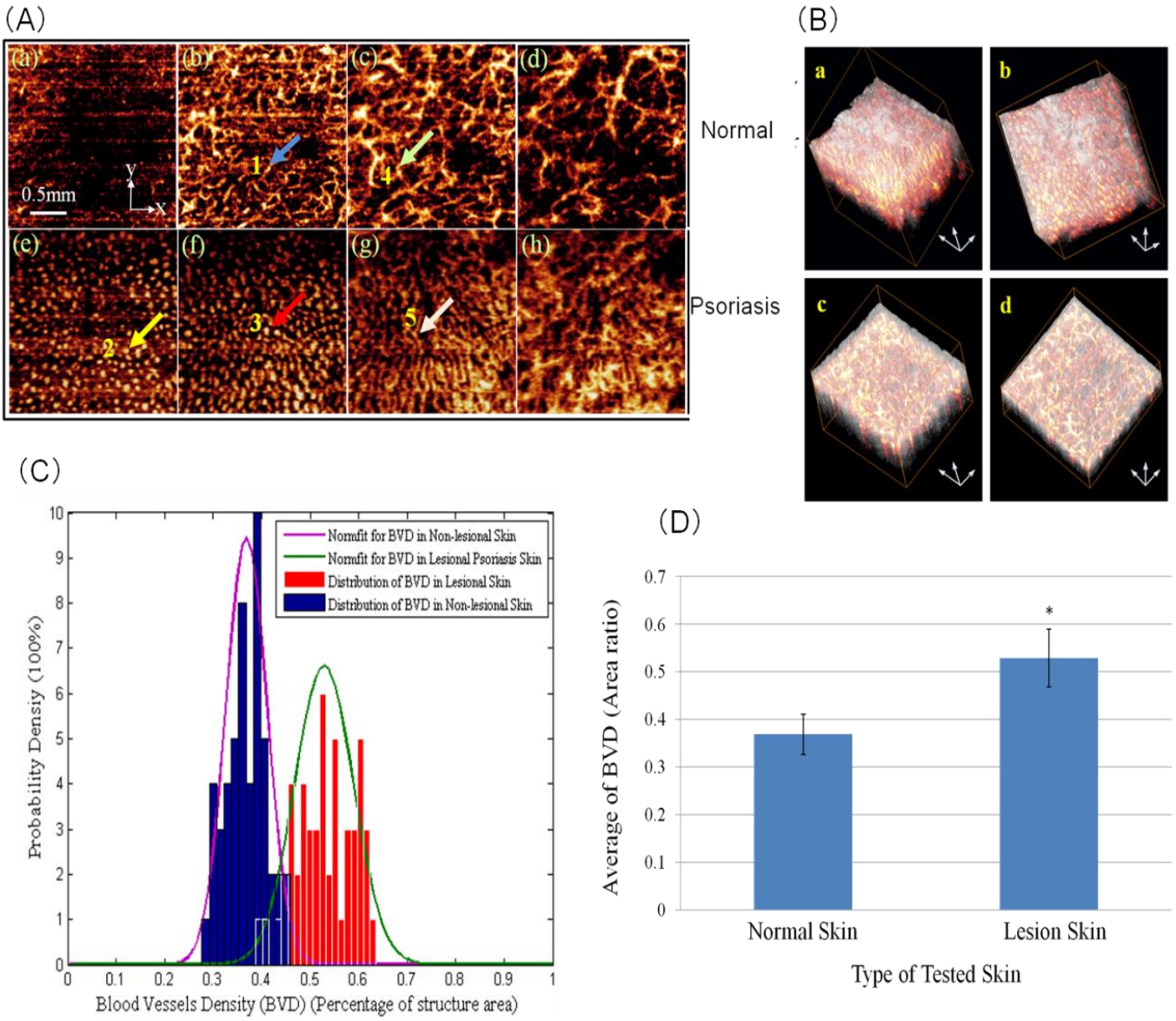

Figure 6 (A) Representative volumetric structural images (x–y–z 3D) merged with microcirculations obtained from (a, b) normal skin and (c, d) psoriasis lesion skin by UHS-OMAG. The cube size is 2.2x2.2 mm^3. (B) Typical *en face* images (x–y plane) at the different depths within the normal skin (the upper row) and the psoriatic skin (the lower row). Columns from left to right correspond to the depths of ~210 μm (a, e), ~340 μm (b, f), ~530 μm (c, g), and ~720 μm (d, h) measured from the tissue surface. One representative region of papillary loops is denoted by number 1 within the normal skin. The typical elongated papillary loops [marked by number 2 in (e) and 3 in (f)] are seen abundant but homogeneously distributed within the psoriasis lesion skin, the appearance of which indicates that the elongated loops are perpendicular to the surface of the skin. The regions of interest scanned were 2 mm x 2 mm. The scale bar is 0.5 mm. (C) Histogram distribution for the blood vessel density (BVD) values obtained from the normal skin and psoriatic skin. Blue bars are for the normal skin and the red bars from psoriatic lesion skin. The bell-curves are obtained by fitting the BVD values in each group to the normal distribution function.

(D) bar graph *(Mean ± SD)* of BVD values of normal skin and lesion skin. (n=50 per group *P<0.001 at a=0.01). (116)

2.1.2.4. UHS-OMAG with supercontinumm light source images (125)

Based on the previous system setup (shown in section 2.1.2.1), we have updated the SLD light source to a supercontinuum (SC) light source. Being spectrally very broad and visually very bright, SC light source has been promoted recently as an excellent alternative for OCT imaging to achieve sub-cellular axial resolution. (125)

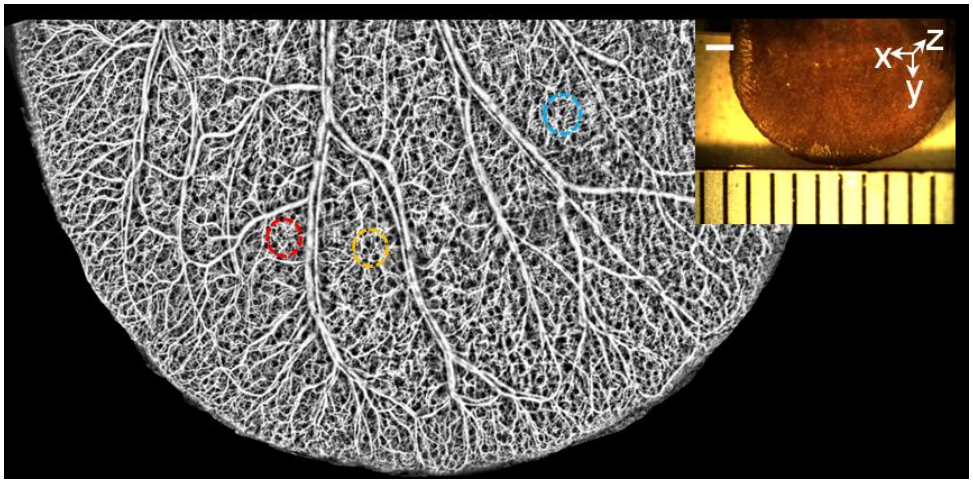

Figure 7 (a) Whole-ear vascular network of a living mouse imaged by a supercontinnum light source coupled UHS-OMAG system. The snapshot of the mouse ear is shown in the right corner. Scale bar represents 1 mm. (125)

To demonstrate the capability of the designed UHS-OMAG system powered by the SC light source, we conducted experiments to image the capillary vessel networks lying within the mouse pinna (ear) in vivo. The scanning protocol described above was applied to capture a 3D data cube that covered 1.2×1.2 mm^2, onto which we applied UHS-OMAG algorithm to obtain both structural and blood flow images. (125) By scanning multiple small regions and combining them together afterwards, Fig. 7 shows a detailed and impressive vascular perfusion map of the whole ear, where the inserted is a photograph of the mouse ear imaged. Since the densely patterned capillary beds and plexus (red circles) can be imaged and resolved clearly, this image demonstrates the power of the OMAG imaging of microcirculations within tissue beds *in vivo.(125)*

2.2. 1st G multi-model optical imaging system applied in burn wound imaging (101)

In this section, we describe a combined DW-LSCI and OMAG system capable of determining relative changes in blood flow, hemoglobin concentration, and morphological features of the blood vasculature. The vessel area density (VAD) is used to quantify the blood vessel network morphology. The multi-model system is employed to assess the blood perfusion status from a mouse pinna before and immediately after a burn injury. (101)

2.2.1. Introduction

Measuring and evaluating changes in the blood flow rate, hemoglobin concentrations, and tissue morphology, are important for studying vascular physiology (126, 127). (101) Usually, changes of blood flow, metabolic oxygenation, and vascular morphology occur simultaneously under physiological and pathological conditions. Changes of these parameters occur simultaneously during capillary recruitment (127, 128). For example, diabetes mellitus patients suffer from absence of capillary reserves, due to changes in oxygen levels (caused by reduced blood flow) and decreased perfusion (129, 130). An overall quantification of their values would enhance our understanding of the hemodynamic and morphological procedures under changes in metabolic demand, taking into consideration that changes of these parameters are interrelated under specific physiological and pathological conditions. A multi-model technique is needed to simultaneously monitor the aforementioned blood perfusion parameters to achieve the goal. (101) Hence, we would be able to obtain several important physiological parameters that enable the quantification of blood perfusion by combining these two techniques into one single system. Previous, DW-LSCI was not sufficient in providing high resolution blood vessel network images, it would be valuable if the DW-LSCI is integrated with a non-contact, non-invasive, high resolution (down to capillary beds) optical imaging technique that has an ability to provide more comprehensive information about the vasculature. OMAG is such a candidate (131) (84, 132, 133). DW-LSCI and OMAG were integrated into one single imaging system. Wavelengths 780 nm and 825 nm were employed in the DW-LSCI system to visualize the blood flow rate change. Near-infrared oxymetry was employed to extract the concentration changes of hemoglobin (134). The OMAG was used to non-invasively image and determine the morphological change of blood vessels under specific conditions where metabolic demands change. In the following sections, the performance of a multi-model imaging

system is demonstrated by noninvasively imaging blood vessel networks *in vivo* within mouse pinna before and after a burn injury. (101)

2.2.2. System and methods

We performed *in vivo* experiments for visualizing the microcirculatory response in the mouse pinna before and after a burn injury to demonstrate the imaging capability of a multi-model imaging system. All experiments were performed on two-months-old C57BL/6 male mice. The mouse pinna was depilated with a commercial human hair remover lotion (Nair) after anesthetizing the animal using 2% isoflurane (0.2L/min O2, 0.8L/min air). A thermal burn was created by using a metal bar with a 2.5 mm diameter tip preheated to 100 ℃. The metal bar was placed in contact with the depilated skin area for a period of ~1 min. The pressure applied to the skin by the metal bar was kept constant during applying the burn. The mouse pinna had an intact epidermis and dermis. Tissue carbonization was not visible. Hence, a partial-thickness burn had been created on the mouse pinna. Both the laser speckle and the optical microangiography system were used to image the mouse pinna before and immediately after the burn. The animal's body temperature was maintained between 36.6 and 37.2 ℃, The animal was disposed of according to IACUC regulations which was approved by the University of Washington Institutional Animal Care and Use Committee and was in compliance with the guidelines of the National Institutes of Health for care and handling of laboratory animals. (101)

The multi-model imaging system is illustrated in Fig.1. Two single-mode laser diodes with a wavelength of $\lambda 1$ = 780 nm (30 mW) and $\lambda 2$ = 825 nm (30 mW) were contained in the DW-LSCI system. As long as the lasers were modulated with an optical chopper at a frequency of 2 Hz, only one laser wavelength was selected at a given time. The two laser beams were aligned via a beam splitter in order to illuminate the same surface area of the sample. To minimize specular reflection, the incidence of the laser beam was at a 30 ° angle from the tissue surface (94). The diffusely reflected light from the tissue was detected with a CMOS camera (Basler A 504k, 1280×1024 pixels) through a zoom lens, providing an adjustable magnification. To maximize the contrast of the speckle patterns, the speckle size was set to twice the size of the camera pixels (135). It could be achieved by setting a magnification of 2.5 and imaging a field of view of ~4 × 4 mm^2. To render high contrast images with sufficient dynamic range for speckle flow imaging, the camera exposure time was set to 10 ms (94, 95). For each data set, the DW-LSCI system

captured 500 frames. It took ~4 min to capture a data set when the frame acquisition frequency was set to 2 Hz; a five by five pixel binning window was applied on the raw image to reduce noise after the data was acquired. The speckle contrast value (K) was computed as the ratio of standard deviation to the mean intensity of each binning window. (101) A spectral domain OMAG system (shown in Fig. 1) has been developed as previously described. A superluminescent diode with a central wavelength of 1310 nm and a bandwidth of 65 nm was used as light source. This setup can yield an axial resolution of ~10 μm in air. This design provided a ~20 μm lateral resolution (89). For providing an imaging depth of 2.22 mm into the sample, the spectrometer had a spectral resolution of 0.141 nm. The A-line rate is 92,000 A-lines per second. The system sensitivity was determined to be 105 dB at a depth position of 0.5 mm from the zero-delay line with the aforementioned speed. A fast scanning protocol (136) was utilized. A number of 256 A-lines were captured along the x-scanning direction, with ~8 μm spatial interval between adjacent A-lines to achieve one B-scan cross-sectional image. The B-scan image covered a range of ~2 mm on the sample. The duty cycle for the rising side of the saw tooth waveform was set at ~80% per cycle. This setup provided a B-scans frame rate of ~280 frames per second. A 2 mm scan range was evenly divided into 200 steps with a 10 μm spatial interval between them in the y-scanning direction. Ten frames were captured and processed to extract one B-scan cross-sectional flow image in each step (136). To form each three dimensional data set, the system acquired 2000 frames. The total time for acquiring one 3D data set took ~7 seconds. This time period is suitable for *in vivo* detection. Finally, thirty five data sets were sequentially acquired in different regions and stitched together to obtain a wide field image that covered an area of ~12×8 mm^2. (101) The image processing method to obtain images of the microvasculature network probed by OMAG has been reported in (89). Before and after the burn injury, the *en face* projected images were analyzed using a vessel area density (VAD) method (137).

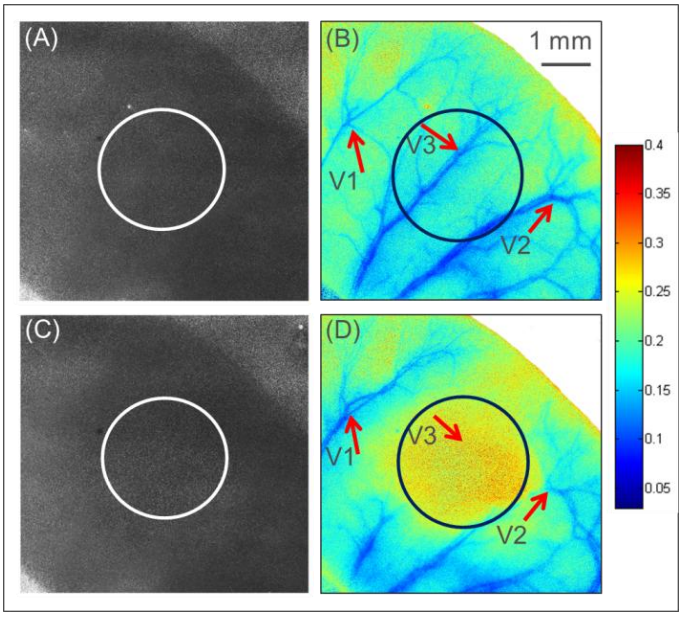

Figure 8 LSCI diffuse reflectance and speckle contrast images of the mouse pinna. (A) Diffuse reflectance, and (B) speckle contrast image of the mouse pinna before the burn. (C) Diffuse reflectance, and (D) speckle contrast image of the mouse pinna after the burn. The circles indicate the burned area. The arrows indicate representative vessels that are affected by the burn injury. Color bar shows the speckle contrast value (K). (101)

2.2.3. Results

The diffuse reflectance (R(0)) and the speckle contrast images (K) from the control mouse pinna, respectively, are presented in Fig. 8 (A) and (B). The diffuse reflectance (R(t)) and the speckle contrast image of the mouse pinna after the injury, respectively was presented in Fig. 8 (C) and (D). The speckle contrast image was calculated with using 20 frames. It was not possible to visualize any biological changes caused by the burn injury by comparing the diffuse reflectance images (Fig. 8 (A) and (C)). However, the speckle contrast images (Fig. 8 (B) and (D)) could highlight large blood vessels. The differences can be observed within the circle region, representing the injured area. The blood flow had decreased after the burn as indicated by an increase in the speckle contrast value inside the burn region. The blood flow changes can be visualized by comparing some representative blood vessels, for example, the ones pointed by arrows V1, V2 and V3 in Fig. 8 (B) and (D). An increase and decrease in speckle contrast occurred in Vessle1 and 2, respectively. Vessel 3 disappears in Fig. 8 (D). (101)

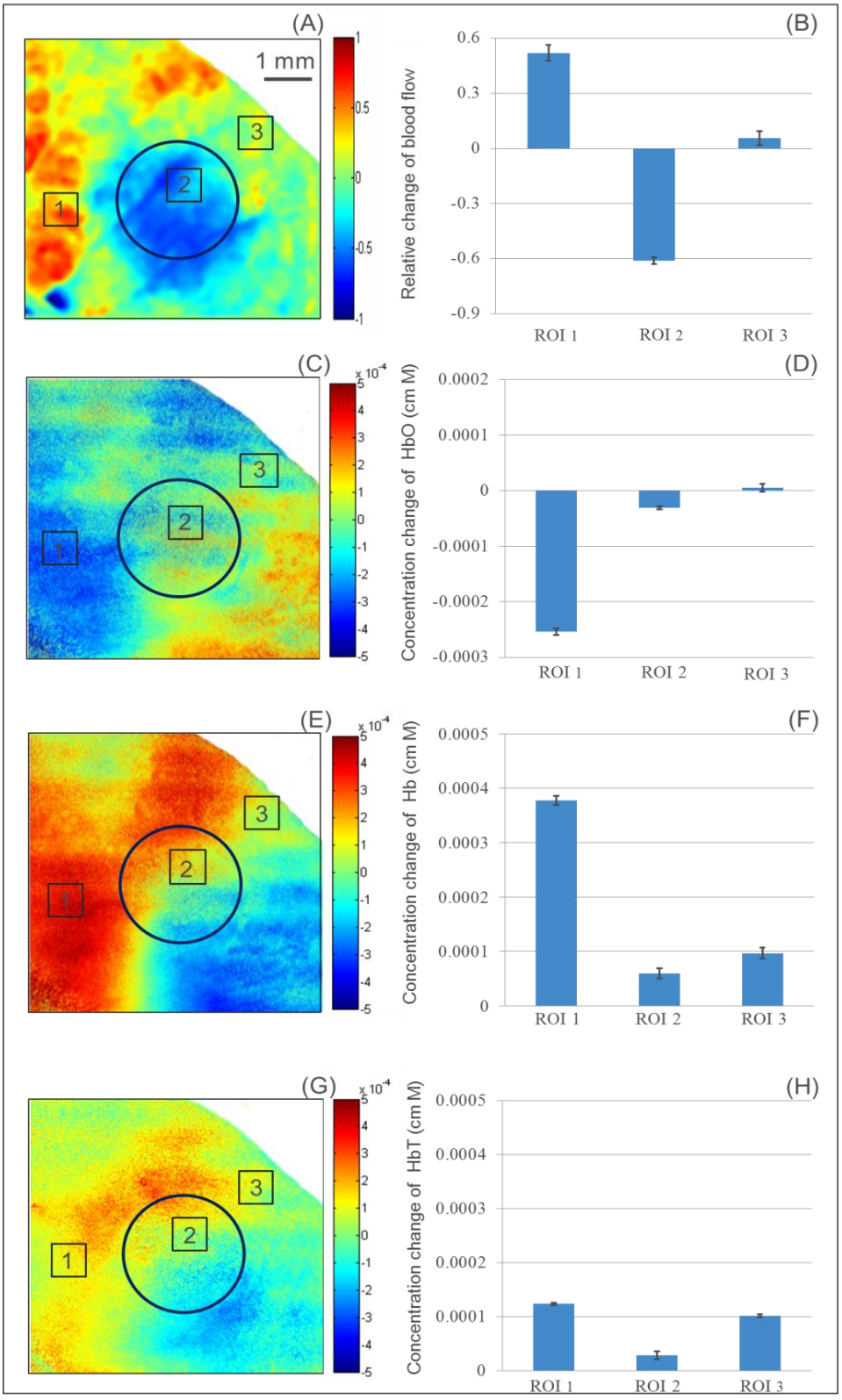

Figure 9 Color coded map of the relative change of blood flow (A), HbO (C), Hb (E) and HbT (G). Mean and standard deviations of the relative change of blood flow (B), HbO (D), Hb (F) and HbT (G), from the three regions of interest. The circle indicates the burned area. (101)

The speckle contrast images (shown in Fig. 8(B) and 2(D)) were converted to flow images by using *Equation 4* and fitting for τ_c. τ_c is inversely proportional to the velocity of the scattering particles. Normalized by the baseline flow (before the injury), the subtraction of the flow images (after the injury minus before the injury), provides the relative change of flow. The normalized relative change of blood flow is shown in Fig. 9 (A). Overall, the flow rate within the injured region decreased, whereas, the flow rate in the surrounding regions increased. We selected three regions of interest (ROI) (marked squares in Fig. 9 (A)) from the image for better visualization. From the three regions, Fig. 9 (B) shows the mean and standard deviation of the relative change of blood flow. It can be determined that the blood flow in ROI 2 was reduced, known as haemostasia, whereas the blood flow in the peripheral regions such as ROI 1 had increased, known as hyperaemia. Moreover, some regions (e.g. ROI 3) did not exhibit significant blood flow change (138). We employed a model reported in (102), from which HbT was also evaluated, to calculate the change in the concentration of HbO and Hb. The concentration change of HbO, Hb and HbT are shown in Fig. 9 (C), (E) and (G), respectively. The mean and standard deviation of the ROIs 1, 2 and 3 are shown in Fig. 9 (D), (F) and (H). We can conclude that the concentration of HbO decreased, and the concentration of Hb and HbT increased which is consistent with hyperaemia in ROI 1(138, 139). Due to thermal damage of the blood vessels, the thermally coagulated region ROI 2 presented a small decrease in HbO, and a slight increase in Hb and HbT. ROI 3 had no change in HbO and a little increase in Hb and HbT. It is assumed that the HbO did not decrease because ROI 3 is rescued by other main vessels even though V1, V2 and V3 had been affected. (101)

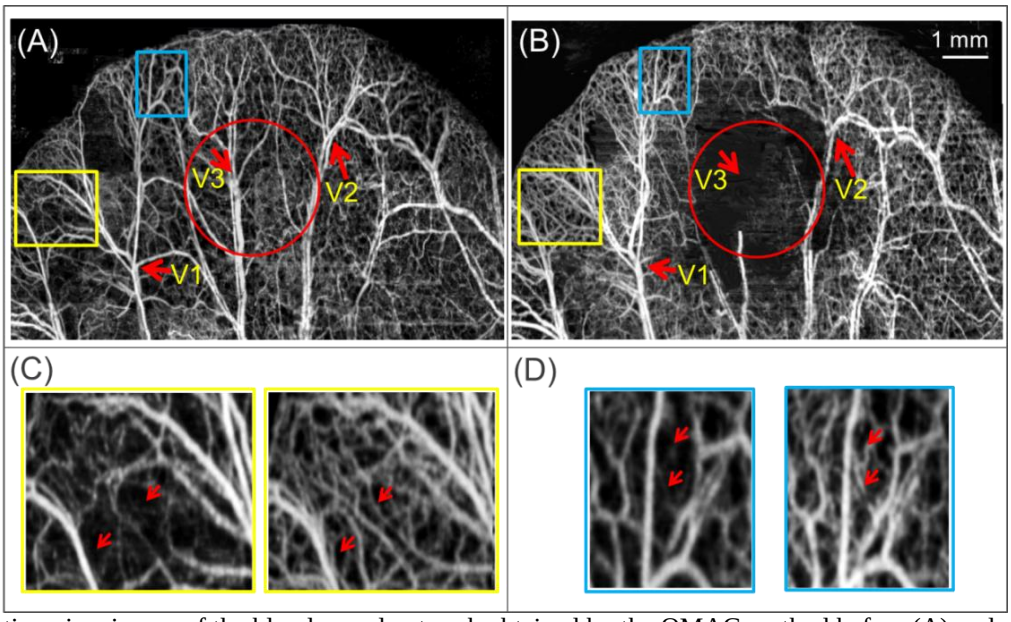

Figure 10 Projection view image of the blood vessel network obtained by the OMAG method before (A) and after (B) the burn injury. The red solid round circle indicates the burned area; the yellow dotted elliptical circle marked a typical ligated artery after burn that performed with vessel dilation. The arrows indicate the reference vessels from Fig. 8. Enlarged areas of the yellow (C) and blue (D) rectangles, where the left and right images belong to (A) and (B), respectively. (101)

We obtained microangiography images of the mouse pinna before and after the burn injury using the OMAG system. The obtained images after stitching together different regions to produce a ~12×8 mm^2 area are shown in Fig. 10. It can be visualized that the OMAG system has higher resolution compared to the LSCI images (shown in Fig. 8(B) and (D)), allowing small capillaries to be identified. The three red arrows indicate the vessels (V1, V2 and V3) highlighted in the LSCI images. It is notable that V1, V2 and V3 appeared to be vessel pairs, appearing as artery and vein, in the OMAG images; while in the LSCI images they seem to appear as single vessels because of its lower spatial resolution. The capillary vessels before and after the burn injury, respectively are shown in Fig. 10 (A) and (B). Fig. 10 (B) includes an area in the middle where there were almost no visible vessels and capillaries, which are indicated by the red circle, where the injury occurred. The vessels may still be present; however, the flow had been stopped or significantly reduced. It is interesting that an artery, which is marked by the yellow dotted elliptical circle, was ligated after the thermal burn. This artery performed as still flowing towards the burn area while suddenly stopping in the middle of the way. It is more interesting that the diameter of this artery changed from ~70 μm to 125 μm, indicating the blood volume increased. The yellow and blue rectangles in the periphery of the burn

area have been enlarged for direct comparison in Fig. 10 (C) and 10 (D). It is noticed that there was an increase in capillary density after the injury. Some representative capillaries have been marked with red arrows. We are certain that the appearance of new capillaries was not due to angiogenesis (new blood vessel formation), since the images were obtained within a few seconds of each other. It is due to reserve capillaries that existed before the injury, but had no or minimum blood flow. These reserved capillaries had been recruited after the injury, known as capillary recruitment phenomena (140, 141). The enlarged images (Fig. 10 (C) and (D)) present a qualitative way for analyzing the images; however, we opted to use a quantitative method to evaluate the vessel density over a given area, i.e. vessel area density (VAD). In a window area, VAD is determined by the ratio of area that is occupied with vessel and capillaries over the overall window area, therefore has a value between 0 and 1 (142). We first converted the OMAG images to black and white to calculate the VAD. We first applied a low pass filter to minimize the image noise. Then, we applied an adaptive threshold algorithm. We created a 64×64 pixels window (white solid box on the top left corner of Fig. 11 (A)) on the black and white image. We then counted the number of white pixels in that window, which was then divided by the total number of pixels in the window. We assigned the value to a middle pixel in the window. We moved the window across every pixel in the image to obtain the VAD image. A smaller window size was used to minimize artifacts for the pixels close to the borders of the images. (101)

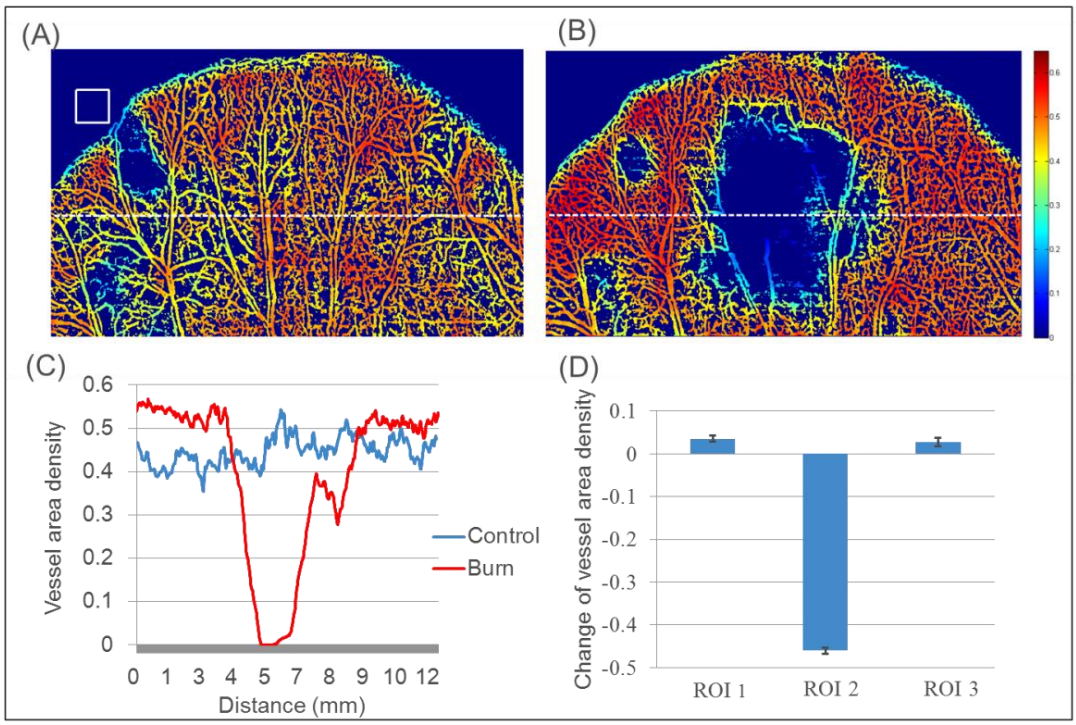

Figure 11 Vessel area density map multiplied by the black and white projection view image of the blood vessel network obtained by the OMAG method before (A) and after (B) the burn injury. The white square in (A) is the window size used to calculate the VAD. (C) Vessel area density of the dashed line in (A) and (B). (D) Mean and standard deviation of the VAD for the three ROI's were determined in Fig. 9. (101)

Figure 11 (A) and (B) show the pre and post injury VAD images multiplied by the black and white image, respectively. These images render the visualization of the regions of high and low vessel and capillary density. We can visualize that the edges of the mouse pinna present a slow decline in density due to the window covering regions both inside and outside of the mouse pinna. Compared to the control image, the VAD image after the injury showed a higher redness in the periphery of the burned area. A region of interest was selected. The regions were indicated by a white dashed line. Fig. 11 (C) shows the VAD of the dashed line from the burn and control image. There was a higher VAD after the burn in the periphery of the injured area. However, there was a significant reduction of VAD within the injured site. The injury was caused with a 2.5 mm diameter bar, however; the reduction in VAD had a diameter greater than that value, indicating that heat might have been diffused out and caused by injury. The mean and standard deviation of the three regions of interest indicated in Fig. 9 are presented in Fig. 11 (D). (101)

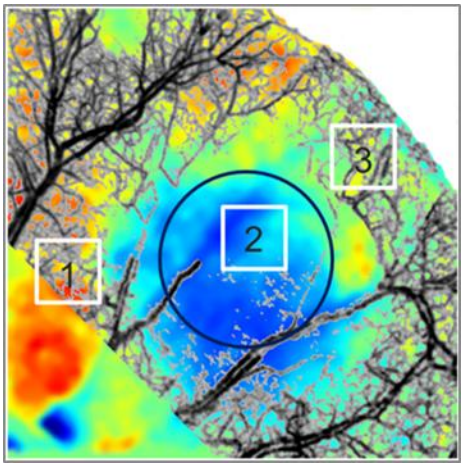

Figure 12 Co-registered image of the change in blood flow image (Fig. 9A) with the projection view image of the blood vessel network obtained by the OMAG method after the injury (Fig. 10B). The color map is the same as in Fig. 9A. The grayscale of the OMAG image was inverted such that the blood vessels appear dark for better contrast. (101)

By co-registering the LSCI and OMAG images, the three regions of interest indicated in Fig. 9 were easily identified (shown in Fig. 12). To provide better contrast, the gray color of the OMAG image was inverted, such that the vessels appeared black. It can be observed that there was an increase of VAD in the upstream and lateral vessel regions, and a significant decrease of VAD within the injured region from Fig. 12. (101)

Except comparisons of functional vascular and tissue oxygenation before and after burn, we examined an application of quantifying the fractal dimension (FD), vessel length fraction (VLF) from small areas of angiography images. There is a need to quantify small microangiography regions in many applications. For example, different morphologies may be shown in blood vessels near and far away from a wound area. (143) A box counting method for calculating the FD of images of different sizes was proposed and demonstrated. We also assess the repeatability for obtaining OMAG images. (101)

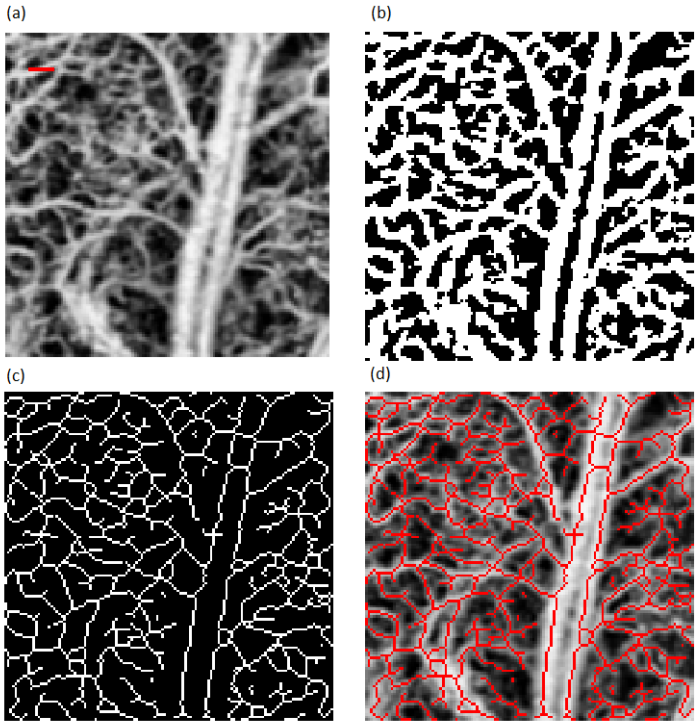

Figure 13 (a) OMAG image obtained from a mouse ear. Scale bar is 0.5 mm. (b) Black and white segmented image of (a). (c) Skeletonization of the segmented image (b). (d) Overlay of (c) and (a). (143)

For Fig. 13 (a), the total number of pixels in the image is 128 × 128 = 16, 384 pixels. The binary image is then skeletonized by reducing all the continuous white segments to a line with a single pixel width. The skeletal image is a representation of the total vessel length. The skeletonization consists of iteratively deleting the pixels in the outer boundary of the segments until a single pixel width line is obtained [34]. As a result, we obtained a collection of lines which represent the midlines of all vessel shapes. A skeletonized image is presented in Fig.13 (c). The VLF is calculated by counting the number of pixels in the skeletonized image, which represents the length of all the vessels, and dividing it by the total number of pixels in the image. (143)

We calculated the fractal dimension over the skeletonized image using a box counting technique (144). This is a method of estimating the fractal dimension from structures that are not perfectly self-similar. The box counting method consists of dividing a skeletonized image into square boxes of equal sizes. In the square boxes, the number of boxes containing a vessel segment is counted. We iteratively repeated this process with boxes of different sizes. The fractal dimension is the absolute value of the slope of the curve that shows the logarithm of the box size plotted against the number of boxes containing a vessel segment. VAD and VLF have values between 0 and 1, while the FD

has a value between 0 and 2. The first section will validate the method that calculates the FD and the segmentation algorithm which enables the quantification of the FD, VLF, and VAD. Then, these parameters are used to prove the repeatability for obtaining OMAG images. Furthermore, a new method of studying angiography images is proposed. We used a box counting method to calculate the fractal dimension (145). The box counting method is applied by dividing a skeletonized image into square boxes of equal sizes, followed by the number of boxes containing a vessel segment is counted. We repeat the process several times with boxes of different sizes. Against the number of boxes containing a vessel segment, thee logarithm of the box size is plotted. The fractal dimension is the negative of the slope of the linear part of the curve. It is defined by:

$$FD = -\frac{log_{10}(N(l))}{log_{10}(l)} \quad [8]$$

where *l* is the box length and *N(l)* is the number of boxes needed to cover the image. Although, true fractal images are linear throughout the whole plot, quasi-fractal images are linear within a subsection of the curve. It is important to quantify small areas of tissue in the study of several microvascular phenomena, such as angiogenesis, which is the growth of new blood vessels. For instance, comparing with the healthy surrounding blood vessels, regions close to tumors may present angiogenic blood vessels, showing as higher tortuosity and FD (146). Hence, as long as the smallest number of pixels within an image is determined, the box counting method can accurately determine the FD value. (143)

2.2.4 Discussion

The absorption coefficients of HbO and Hb around near infrared region (~800 nm) are relatively low, though the light sources in this region we used in the proposed system can achieve deeper penetration depth. The intensity modulations to both of the wavelengths may be contributed by the absorption coming from the other components, which might lead to system biases to the final results (44). One alternative strategy is to use the laser sources working at 560 nm and 580 nm because of their high absorption coefficients, which are more than 10 times higher than 800 nm range. The captured intensity modulations of different wavelengths will be dominated by the HbO and Hb absorption upon this case. However, the penetration depth achieved by a ~570 nm laser is relatively low compared with that at around ~800 nm. (101) Moreover, the OMAG beam cannot be directly visualized on the

LSCI camera which decreases the efficiency of LSCI conducted OMAG beam localizing the exact intended imaging region. Hence, laser source at the wavelength ~1000 nm, which is able to be received by the CMOS camera of LSCI, is in need to be employed and coupled to the OMAG sample arm to aid in visualization of the exact regions scanned by OMAG. However, we need a high quality customized diachronic mirror to separate the 570 nm/ 800 nm (LSCI light source) range and 1000 nm (conducting light) with 1300 nm (OMAG light source). Furthermore, more complicated alignment work will be needed. (101) There is also a limitation in UHS-OMAG. Currently, UHS-OMAG could clearly reveal detailed micro-vasculature networks; however, it loses some functional information, such as the blood flow velocity variance and blood flow direction. To suppress the limitation, an alternative strategy is to combine the scanning protocol of UHS-OMAG and the conventional OMAG method together. However, this requires the imaging probe to scan the same area twice, which will be time consuming resulting in a disadvantage in capturing rapid changes in functional parameters. (101)

2.2.5 Conclusion

In this chapter, a multi-model imaging system that combines DW-LSCI with OMAG is described. It can be used to asses several important physiological parameters of the tissue blood perfusion status. The relative change in blood flow and blood oxygenation is revealed by the DW-LSCI system. High resolution images of small capillary networks, allowing for the quantification of the vessel area density and the observation of the capillary recruitment are revealed. The results observed could provide spatial information of the blood perfusion parameters. In the chapter, I also mentioned that these results are consistent with haemostasia occurring in the burn area and hyperaemia occurring in some of the surrounding regions. We also observed the capillary recruitment within a few minutes after the injury. DW-LSCI is featured in imaging large areas with fast imaging acquisition speed. Although OMAG has a small field of view and requires several small images to be stitched together, it provides depth resolved high resolution images. Overall, the 1st generation multi-model imaging system delivers a valuable platform for better understanding the functional hemodynamic and morphology changes of the vasculatures. The utilization of the system can play an important role in diagnosis and treatment of diseases that have vascular involvement. (101)

Chapter 3. Improving the imaging speed and enhancing the functions of multi-model

imaging system

A 2nd G DWLS-OMAG system has been developed for imaging blood flow, blood oxygenation, vascular remodeling, and flow direction in small animal models. The integrated system that incorporates a 'synchronized dual wavelength laser speckle imaging system and function'-enhanced OMAG system can provide a full set of parameters of the injured tissue responses. The objectives are (I) to optimize the prototype 780-nm and 825-nm DW-LSCI and 1310-nm OMAG system for 2D and 3D mapping of the microcirculation; (II) characterize SDW-LSCI, which is integrated into OMAG, named as SDWLS-OMAG for imaging cerebral blood perfusion during experimental acute ischemic stroke in the mouse. In this chapter, we use a series of experimental models to demonstrate that SDWLS-OMAG has the capability to generate real-time 2D and 3D images of both tissue structure and blood flow at capillary level resolution with an imaging depth up to 2 mm without the need for exogenous contrast agents. The incorporated SDWLS-OMAG is designed to rapidly extract blood flow signals from the huge "noise" background of optical scattering. Briefly, in order to investigate the potential of SDWLS-OMAG imaging of cerebral microcirculations in mice with the cranium left intact, we have developed a synchronized dual wavelength laser speckle imaging system that used 780-nm and 825 -nm laser sources to rapidly 2D map blood flow and tissue oxygenation over the whole brain to guide OMAG system for subtleties exploration. We have also performed new scanning protocols and data processing algorisms to enhance the functions of OMAG system for blood flow and blood flow direction measurements. We demonstrated the SDWLS-OMAG for mapping detailed blood flow and morphology responses to an ischemic injury in mice. In this section, we presented images of mouse brain and pinna *in vivo* acquired by the use of the prototype. These results demonstrate that OMAG is capable of visualizing the subtleties including capillaries, its progressive changes and vascular remodeling over time after tissue injury under the guidance of SDW-LSCI, which can provide regional change of vasculature flow and oxygenation. SDWLS-OMAG is able to produce dynamic images to draw out pathophysiological problems that could not be achieved with existing tools. (147)

3.1. The 2nd G SDW-LSCI system utilized for monitoring hemodynamic changes in a mouse stroke model

In this section, we describe a newly developed synchronized dual-wavelength laser speckle contrast imaging system. It consists of two cameras that are synchronously triggered to acquire data at a high spatiotemporal resolution. The resolution can reach up to 500 Hz for ~1000 × 1000 pixels. We used a mouse model of stroke to demonstrate the system's capability for imaging fast changes, which usually occurred within tens of milliseconds, in the relative changes in blood flow, oxygenated and deoxygenated hemoglobin concentrations in the mouse brain, with the cranium left intact. This novel imaging technology will play an important role in fast imaging of hemodynamics and metabolic changes in vascular diseases.(147)

3.1.1. The SDW-LSCI system development and methods

In response to cellular oxygen demand, cerebral blood flow changes occur rapidly. As the hemodynamic and biochemical parameters, relative changes in blood flow and changes in the concentrations of HbT, HbO, and Hb indicate the status of blood perfusion. For example, odor stimulation in the olfactory bulb glomeruli evokes local functional hyperemia accompanied by increased blood flow and HbO in blood vessels within seconds (46). LSCI (148) (46) with single wavelength, is capable of measuring the relative changes in blood flow in biological tissues, while they are unable to detect changes in hemoglobin concentration. Although spectroscopy methods are capable of determining the absolute changes in the concentrations of HbO, Hb, and HbT, they cannot detect blood flow (149, 150). DW-LSCI integrates two wavelengths in one system. It enables the imaging of both the relative changes in blood flow and changes in hemoglobin concentrations. Previously, DW-LSCI has been used to investigate functional activation and cerebral ischemia (95) (101) in small animal models. However, either a filter chopper or a digital signal for modulating or triggering the light sources are required in these systems Hence, the temporal resolution has been limited to 2 Hz (94), 10–29 Hz (151), 18 Hz (95), and 80 Hz (152) with low spatial resolutions (256 × 256 pixels), which are too slow to be sensitive to fast physiological responses in the brain (53). Moreover, the acquired images are interleaved. Thus, a time interval exists between the images acquired from each wavelength. Interpolation allows the frames to be registered at the same time point; however, it adds errors to the measurements. Some multimode imaging techniques for blood-flow diagnostics have been recently proposed using a combined fluorescence intravital microscopy, dynamic light scattering, and spectrally enhanced microscopy modalities (54)

and MRI (153). However, the injections of contrast agents are required in these methods. In addition, their temporal resolution is relatively slow. (147)

We require a fast optical imaging technique to localize the exact injured region core of the tissue and then guide the OMAG for subtleties investigation. Here, we have developed and utilized the 2ndG SDW-LSCI system to differentiate the infarct, peri-infarct, and healthy regions in the brain after ischemia injury (72, 154-156). Reflectance images backscattered can be acquired by the SDW-LSCI system by employing two CMOS cameras from a sample illuminated by lights at two wavelengths (λ1=780 nm and λ2=825 nm), which are necessary for tissue oxygenation evaluation. Enabling acquiring images at both wavelengths simultaneously with a higher spatial and temporal resolution than the prior reported systems (33, 71, 72), the frame rate ranges from 100 Hz to 500 Hz for ~1000×1000 pixels (pixel size radius=8.5 μm). The spatial resolution of this system is ~11.4 μm, acquired by testing the USAF RES Target (resolution test pattern) (see Fig. 17 (a)). We tested the flow sensitivity of the SDW-LSCI system by measuring the minimum flow velocity using the phantom flow made by Research and Test Particles Latex Microsphere Suspensions (0.30 μm diameter) in translucent Teflon tubing. The minimum flow of ~35 μm/s can be tested by our system. In this chapter, it is demonstrated that the applicability of the SDW-LSCI by imaging the relative changes of blood flow as well as changes in the concentration of oxygenated, deoxygenated and total hemoglobin during an experimental stroke model in a mouse brain through an intact cranium. (147)

The SDW-LSCI imaging system is illustrated in Fig. 14 (a). We combined two collimated diode lasers at the wavelengths of λ_1=780 nm and λ_2=825 nm coaxially by a dichroic beam splitter DBS_1 (>99% transmission at λ_1, >99% reflection at λ_2). Then, we expended both of the lasers, making them uniformly illuminated the sample, with an illuminated area of ~12 mm in diameter, at an incident angle of ~60 °(48) from the tissue normal direction. The backscattered light, was transmitted to a zoom lens (Zuiko, 75-150 mm, f/4.0), routed towards two (one for each wavelength) CMOS cameras (Basler A504k) via another dichroic beam splitter, DBS_2. DBS_1 and DBS_2 have the same parameters. We configured the two cameras to acquire images at a synchronized frame acquisition speed from 100 Hz to 500 Hz. We also aligned both of the cameras to acquire the images with the same area. We adjusted the magnification of the system to obtain a field of view of ~10×10 mm^2, to fit the size of the whole mouse brain [Fig. 14(b)] in the experimental stroke model. We employed λ_1 in acquiring images to extract the relative change of blood flow. We also acquired images using both λ_1 and λ_2 for elucidating the concentration changes of HbO, Hb and

HbT (ΔHbT = ΔHbO + ΔHb). We set the exposure time of the camera at ~10 ms. It was optimized to achieve high contrast with sufficient dynamic range for speckle flow imaging (50). Hence, the frame rate was set to ~100 Hz. (147)

The speckle contrast was elicited by quantifying the blurring of the speckle pattern over the exposure time of the camera after data acquisition. Here we computed the temporal speckle contrast maps as the ratio of the standard deviation to the mean intensity for each single pixel along every 20 frames. We still derive the flow velocity from spatial speckle contrast (50, 157). The Beer-Lambert law model was used to estimate changes of hemoglobin concentration, as previously described (48, 49, 110, 158), given that the concentration changes of HbO and Hb would cause changes in the diffuse reflectance due to their absorption properties. For each dataset, we captured 500 frames. It took ~4 min to capture a data set as long as the frame acquisition frequency was set to 2 Hz. $CMRO_2$ can be elicited from:

$$1 + rCMRO_2 = (1 + \frac{\Delta CBF}{CBF_0})(1 + \gamma_r \frac{\Delta Hb}{Hb_0})/(1 + \gamma_t \frac{\Delta HbT}{HbT_0}) \quad [9]$$

where the 'o's indicate the baseline values. There are several parameters need to be predetermined for calculation of $CMRO_2$. For example, the parameters γ_r and γ_t are vascular weighting constants, taken into account that the measured changes in hemoglobin are a combination of arterial and venous quantities (159). We assumed their values are 1.25 in our calculation (159). $\frac{\Delta CBF}{CBF_0}$ represents the relative change of cerebral blood flow. This parameter could be obtained through calculating the relative blood flow velocity change when the blood vessel diameter could be obtained. $\frac{\Delta Hb}{Hb_0}$ and $\frac{\Delta HbT}{HbT_0}$ denote the relative concentration changes of Hb and HbT. As different wavelengths have different absorption coefficients, the HbO and Hb concentrations could be calculated through solving absorption equations based on the Beer-Lambert law. (147)

3.1.2. Results: 2ndG SDW-LSCI system images experimental stroke

We have shown that OMAG is predominantly providing details of blood flow in tissue injury. However, OMAG is a high resolution 3D imaging techniques, using which the scanning mode and data computations decrease the imaging efficiency. Therefore, a rapid 2D mapping of the whole mouse brain is required to guide OMAG to specifically target to the regions of interest for deeper investigation. The SDW-LSCI has been developed as a dual-wavelength system, incorporating two cameras that are synchronously triggered to acquire data to achieve a high spatiotemporal resolution (up to 500 Hz for 1000x1000 pixels). This rapid system is particularly useful to

provide rapid 2D mapping of fast hemodynamics changes. (147)

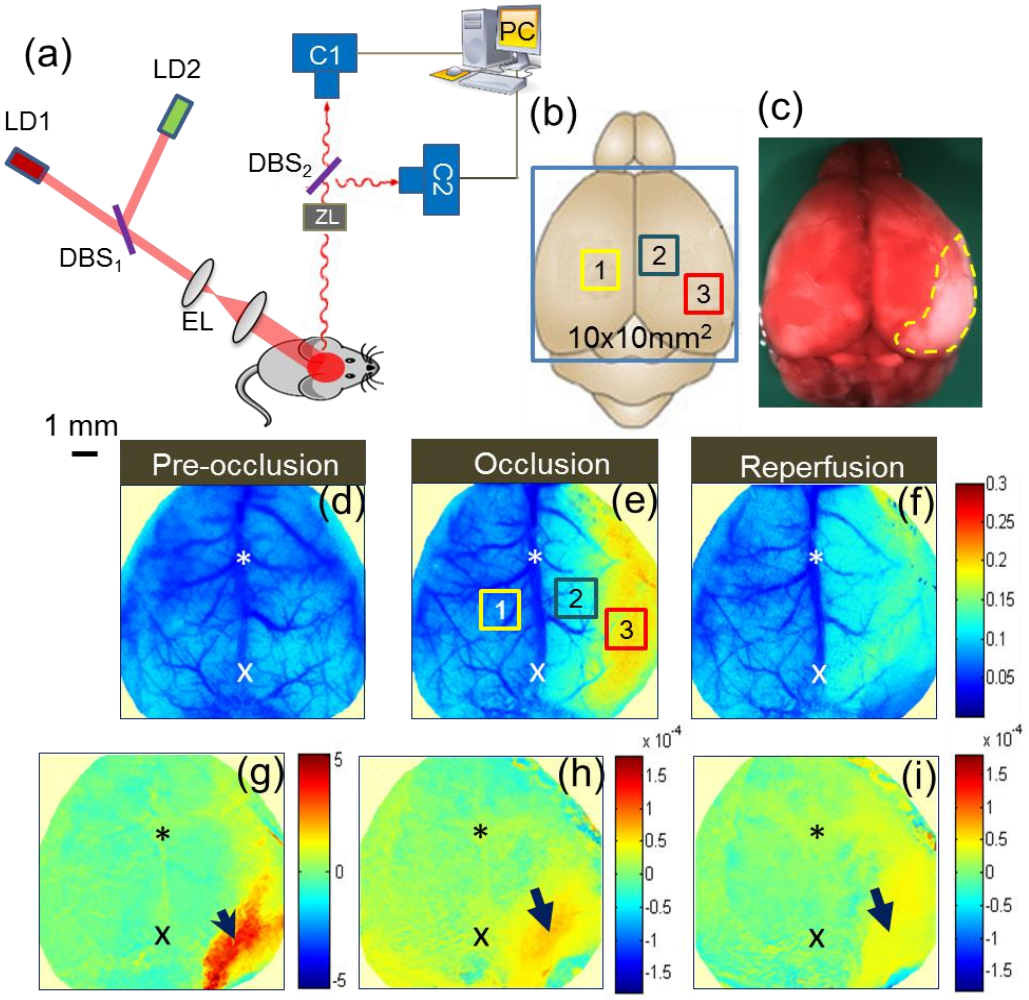

Figure 14 Rapid 2D mapping of blood flow and hemoglobin concentration from a MCAO mouse model. (a) Schematic diagram of the system. LD_1: 780 nm laser diode, LD_2: 825 nm laser diode, DBS: diachronic beam splitters, EL: beam expanding lenses, C: cameras, ZL: zoom lens, PC: computer; (b) Delineation of the mouse brain with the imaging field of view of 10×10 mm^2 and three squared regions of interest 1, 2 and 3; (c) TTC snapshot image with the infarct region circled by the yellow dashed line; (d) Laser speckle contrast image of a normal mouse brain; (e) Laser speckle contrast image at the time point of 60 min post-occlusion, with the same three regions of interest 1, 2 and 3 depicted in (b); (f) Laser speckle contrast image at 2 min after reperfusion. (g) Relative change of the blood flow between the time points of (e) and (f). Concentration changes of (h) HbO and (i) Hb from the time point of (e) to (f). The arrows in (g)-(i) indicate the infarct regions. The asterisk and cross symbols in (d) to (i) represent the bregma and lambda, respectively. The scale bar represents 1 mm that applies to (d)-(i). (147)

We imaged the rapid blood perfusion response aftermiddle cerebral artery occlusion (MCAO) followed by

reperfusion to demonstrate the effectiveness of the SDW-LSCI system for measuring the relative changes of blood flow and changes in hemoglobin concentrations (160). We applied triphenyltetrazolium chloride (TTC) histology to determine the ischemic injury (infarct) to confirm the imaging results. A 6-0 nylon filament with a silicone-coated tip was inserted into the right internal carotid artery via the external carotid artery of an anesthetized mouse. The filament was removed at which time reperfusion occurred after 60 min or 90 min (we use 60 min here) of occlusion. Figs.14(d), 14(e) and 14(f) present the speckle contrast images of the whole mouse brain before occlusion, at 60 min after occlusion and at 2 min after reperfusion, respectively. During occlusion and reperfusion, the contrast value increased in regions of interest (ROI) 2 and 3 compared to that of pre-occlusion, indicating a decrease in blood flow according to the relationship between the speckle contrast and flow velocity. The blood flow in the ischemic region (ROI 3) increased after reperfusion compared to the occlusion as well. Fig. 14 (g), (h) and (i) show the whole map of relative change of blood flow, and the changes of HbO and Hb from 60 min post-occlusion to 2 min after reperfusion, respectively. Normalized by the 60 min post-occlusion time-point, the relative change of blood flowwas calculated as the difference between the 60 min post-occlusion and the 2 min post-reperfusion. Fig.14 (g) exhibits the relative change of blood flow extracted from the speckle contrast values from the time points of Figs.14 (e) and 14 (f). We can clearly differentiate the ischemic region (marked by arrows) in these maps. Finally, Fig. 14 (c) exhibits TTC staining at 24 h after MCAO, in which the infarct area circled by the yellow dashed line was consistent with the region with the most severe changes localized in the maps presenting changes of blood flow, HbO and Hb in Figs.14 (g), 14(h) and 14(i). In general, the blood flow and concentration changes of Hb and HbO increased in the ischemic region shortly after removing the filament due to the restored blood flow. (147)

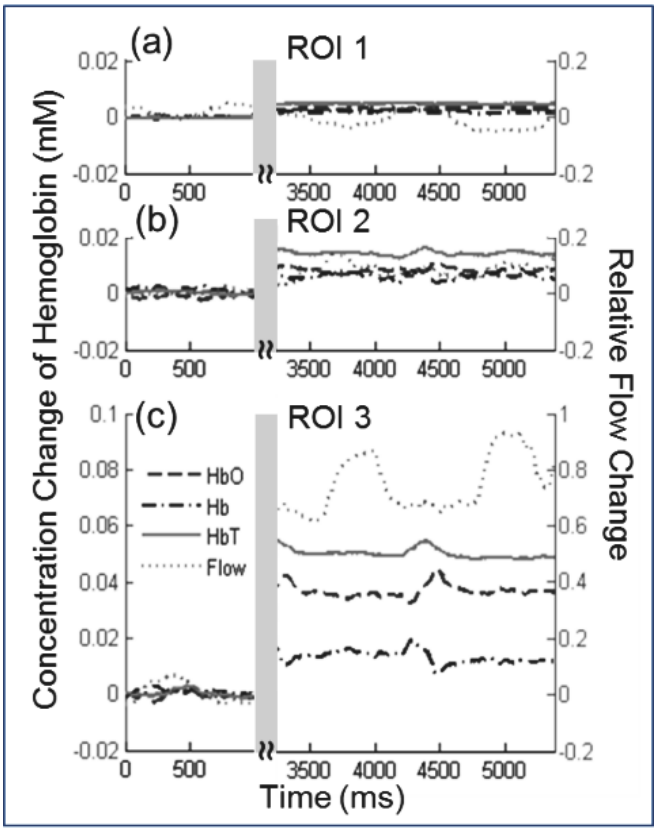

Figure 15 The time courses of the changes of four parameters, blood flow (dots) according to the right y-axis, Hb (dash-dot), HbO (dashes) and HbT (solid) according to the left y-axis in (a) ROI 1, (b) ROI 2, and (c) ROI 3 before and after filament removal. (a) Variances of the four parameters in ROI1 in the non-ischemic hemisphere of the brain depict a small change after removing the filament. (b) Variances of the four parameters show a rising trend in ROI 2 compared with those in ROI 1. (c) All the values of the parameters increased in ROI 3, indicating hyperemia. The vertical bar represents the time period of filament removal (reperfusion) ~2.5 seconds, when the light was blocked out. The SDW-LSCI system is capable of collecting dynamic variances with time intervals of milliseconds in localized regions of interest. (147)

We selected three regions and a time course from occlusion to reperfusion for quantifying the rapid changes of the above parameters. Changes of all the parameters from the three selected regions for a period of 5.5 sec are demonstrated in Fig. 15. ROI 1 had negligible changes of all the parameters (Fig. 15(a)). ROI 2 presented small changes of the parameters (Fig. 15(b)) compared to ROI 3. During occlusion, all the parameters (Fig. 15(c)) in ROI 3 presented large changes. Here, hyperemia is indicated, showing as the changes presented in ROI 3 after removing the filament. It is noteworthy that the blood flow (dots) in ROI 3 appeared periodically (~1 Hz), which is appreciated due to the high acquisition rate of the system. It indicates a low

perfusion state caused by the damaged capillaries in the infarct region, where the restoration of normal flow was disturbed (161). In general, the hemodynamic and metabolic alternations in the occlusion followed by reperfusion in the whole mouse brain can be recorded by the instrument, which has high spatiotemporal resolution, high sensitivity and with a large field-of-view. However, the proposed SDW-LSCI system still has some limitations. For example, the two cameras are required to be co-registered with pixel level resolution. This issue is time consuming during the system development, compared to the single camera system. It is critical that the proposed SDW-LSCI system enables synchronized imaging of relative changes of blood flow and the changes in hemoglobin concentration. It is featured to overcome the drawbacks of previous imaging modes, which lack the ability to acquire both wavelengths with high spatiotemporal resolution and large field-of-view. The detailed investigation of the fast hemodynamics and oxygen metabolism of physiological and pathological activities will be facilitated by the parameters. Hence, this system would enable noninvasively monitoring and diagnosing vascular diseases *in vivo*. Also, it is useful to monitor immediate hemodynamic responses which occur during normal and abnormal cognitive and motor functions. (147)

3.2 Repeatability of OMAG system for vessel remodeling imaging

It is important to validate the repeatability for obtaining OMAG images to guarantee that the calculated values for FD, VLF, and VAD are comparable among images, This is crucial for long term imaging. Here, OMAG images were obtained at three consecutive days from the same region of a mouse ear. Each day, six OMAG images (2×2 mm^2) from different regions of the mouse ear were obtained and stitched together to create a larger image (3.5×5.5 mm^2).

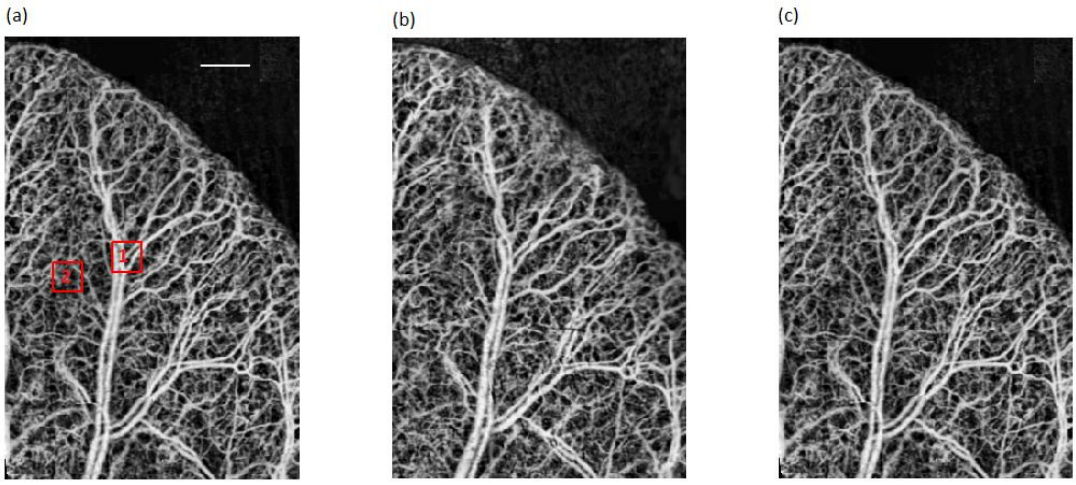

Figure 16 OMAG images obtained from the same mouse ear at day (a) 1, (b) 2 and (c) 3. Scale bar is 0.6 mm. (143)

Figure 16 presents the *en face* maximum projection view images from the mouse ear, obtained on three consecutive days. (143) The fractal dimension, vessel length fraction, and vessel area density were calculated for the images exhibited in Fig. 16. We elicit fractal dimension, vessel length fraction, and vessel area density from the images of days 1, 2, and 3. The fractal dimension are respectively listed: Day1: 1.754; Day 2: 1.751; Day 3: 1.747; vessel length fraction are respectively: Day1: 0.12; Day 2: 0.12 Day 3: 0.123; vessel area density are: Day1: 0.441; Day2: 0.433; Day3: 0.433. We calculated the repeatability based on computing overlapping of the binaries images. We calculated the overlapped vessel region over the whole vessel regions, and obtained 99% repeatability value. (143)

The capability to simultaneously capture blood flow velocities at different ranges from arteries/veins down to the capillary level is important for a comprehensive study of vascular responses during occlusion and reperfusion. This is because the flow velocity within the cerebral cortex exhibits a wide range of values, from tens of μm/s in capillaries to tens of mm/s in larger vessels. The previous study is not able to provide tunable flows from a 3D image scan. To overcome this limitation, a tunable velocity ranges in capillaries, venules and arterioles can be achieved by implementing a new effective scanning protocol. Briefly, the fast scanner is driven by a step waveform. A 3D image is composed by totally 400 steps; at each step, a 25 times repeated A scans will be acquired while keeping a stabilized scanner to realize high correlation between A scans; different velocity ranges are achieved by post processing A scans with wide range time interval (162). With the imaging speed of 75 kHz A-scans per sec,

one 3D scan of 2x2 mm2 region can be acquired in ~67 sec (frame rate 3 Hz and totally 200 frames). We incorporate this multi-range Doppler OMAG (162) into our SDWLS-OMAG system to achieve 3D blood flow velocities images at different ranges from arteries or veins down to capillaries. (162)

3.3. The integrated SDWLS-OMAG system and its utilizations

3.3.1. The development of the integrated SDWLS-OMAG system

We utilized a multifunctional imaging system (147) for imaging CBF in both *en face* and cross section view of the mouse brain. The system incorporates SDW-LSCI and DOMAG modalities. It is advantageous in continuously and comprehensively monitoring the neural activities involved in the physiological processes noninvasively. The schematics of the systems are delineated in Fig.18 (a). The SDW-LSCI system setup is marked by the blue dotted square in Fig.18 (a). Both cameras were acquiring images at 100 fps with 1000×1000 pixels. To avoid spatial offset, the images with two wavelengths captured by the two CMOS cameras were aligned by micro scale ruler before acquiring the mouse brain images. The field of view was set to ~6×6 mm^2 to fit the dimension of the contralateral side of the mouse brain [Fig.18 (b)]. The feature of integration strategy of the 2^{nd}G DWLS-OMAG system included: a 3D translation stage that could carry the OMAG probe to select the imaging area without moving the animal. The diachroic mirror DBS_0 was the shared component of OMAG and SDW-LSCI. The dichroic beam splitter DBS_0 was used to transmit the light from the SDW-LSCI system and reflect the light from the OMAG system. These designs give us the unique flexibility to select the imaging area of OMAG while keep the same field of view of SDW-LSCI, and constantly maintaining the optical performance of each of them. A relay lens was positioned after the objective lens of OMAG for enlarging the distance between the sample to the OMAG objective lens to create more space for the DBS_0 and SDW-LSCI probe. The focus spot of OMAG objective lens was fixed at twice of the focus length of the relays lens and kept the beam spot rightly onto the sample at the distance of twice of the focus length of the relay lens. The schematic diagram of the OMAG system is marked by the red dotted square in Fig.16 (a). A superluminescent diode light source (central wavelength 1310 nm, bandwidth 56 nm) was employed for sample illumination in this system. Therefore, the theoretical axial resolution in air was ~13 μm. The tested axial resolution was ~15 μm. The light was divided into two paths using a 2×2 optical coupler. The light in one of the paths was

transmitted towards a mirror in the reference arm, and the light in the other path was transmitted towards the mouse brain in the sample arm. In this arm, the light was coupled into an optical system which included a collimator, a pair of galvo scanners, and an objective lens with a 30 mm focal length, providing a lateral resolution of ~10 μm. The light reflected from the sample and reference arm were recombined and transmitted to a home-built spectrometer. The spectral resolution was 0.141 nm which provided an imaging depth of ~3.0 mm. The camera had a line scan rate of ~1.5 kHz, and each frame contained 512 A-lines that cover ~2.2 mm on the sample. Serial repeated B-scan images were acquired at a frame rate of ~3 fps and 42 seconds. (163)

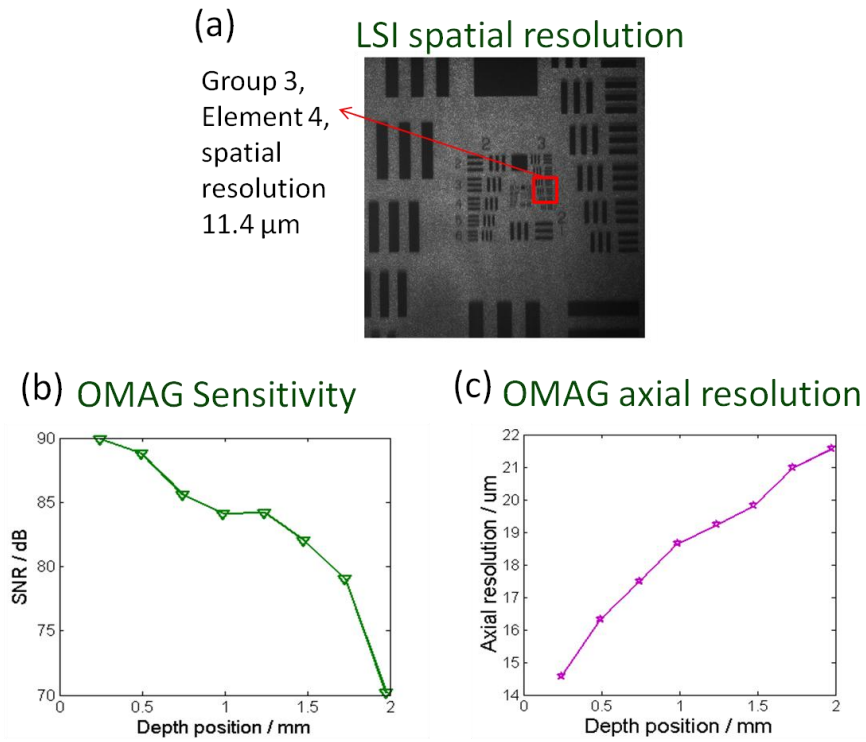

Figure 17 System performance (a) spatial resolution of SDW-LSCI system is ~11.4 μm, which is tested by the USAF RES Target (resolution test pattern). (b) OMAG sensitivity 20 dB falling off. y axis: the signal to noise ratio (SNR), x axis is the depth position. From the graph, we can determine the SNR change from 90 dB to 70 dB from zero delay line to depth of 2 mm. (c) OMAG system axial resolution: calculate the half peak width in each depth position (moving the sample micro lens from zero delay line to 2 mm).

For brain hemodynamic and metabolic responses evaluations, several parameters were calculated from the images captured by the multifunctional systems. Firstly, the speckle contrast maps were calculated as ratio of the standard

deviation to the mean intensity rendered by moving a 5×5-pixel binning window in the raw intensity image at the wavelength of λ1=780 nm. The flow velocity could then be derived from the model of spatial speckle contrast versus flow velocity (157). Secondly, the concentration changes of HbO, Hb and HbT and $CMRO_2$ were obtained by using the images acquired with both λ1 (780nm) and λ2 (825 nm). A differentiation model, based on absorption of the light between two wavelengths, was used to estimate the changes of HbO and Hb (71, 147, 164). HbT is defined as the amount of hemoglobin (unit: milli-mole) per liter of blood, which is equivalent to the sum of HbO and Hb. $CMRO_2$ was extracted using Equation 9 (165) by assuming a baseline concentration of Hb and HbT as 40 μM and 100 μM, respectively (165).

3.3.2. Functional evaluation of hemodynamic and metabolic variations during neural activation (163)

In neural activation, evaluation of spatiotemporal hemodynamic and metabolic responses is crucial in studying brain functions. In this chapter, using a non-invasive multi-model optical imaging system, we measured hemodynamic and metabolic responses in the mouse brain upon electrically stimulated neural activation using the developed SDWLS-OMAG system. SDW-LSCI was run at an image acquisition speed at ~100 Hz. It was used to extract the large-scale 2-D map with the localized response of blood flow, hemoglobin concentration, and metabolic rate of oxygen change. It was also utilized to monitor near real time hemodynamic responses, thus it can guide the OMAG image acquisition. With its unique depth-resolved capability, OMAG is prominently used for imaging the response of typical vessels. The demonstrated feasibility of the integrated system in the investigation of neural activation would play a important role in pre-clinical study of the mechanism of neurovascular coupling, diagnosing, and treating neurological diseases. (163)

3.3.2.1. Introduction

A platform for the study of brain functions is provided by neural activation. It is a physiological landmark in brain function explorations that changes in neuronal activity are associated with changes in both local blood flow and metabolic responses (166). Nowadays, evaluation of the hemodynamic and metabolic responses in neural activation

has become an effective tool for studying normal or pathological brain functions. The local blood flow and energy metabolism are anatomically restricted to specific activated areas in the brain as reported in (167). Nerve tissue in localized brain area is thought to be provided with sufficient substrates, such as glucose and oxygen. Those substrates are required for local energy metabolism. Usually, the dynamic variations of cerebral blood flow (CBF), the concentrations of hemoglobin, and cerebral metabolic rate of oxygen ($CMRO_2$) are used as surrogate markers for neuronal activation in specific brain areas (94, 95, 168). The highly vascularized central nervous system is enclosed by meninges, which contains three connective tissue layers: dura mater, arachnoid mater and pia mater. Perivascular nerves play the role of regulating vascular tones and perfusions in the meningeal layer. During the regulation process, in order to reconcile local variations of blood flow in brain activities, chemical signals released from activated perivascular nerves and astrocytes alter vascular tones (169). The vascularization and blood circulation within meninges are important for a number of neurological diseases and complications (163, 170, 171). Laser speckle contrast imaging (LSCI) (46, 107) and near-infrared spectroscopy (NIRS) (172) (including multi-wavelength 2-D imaging) have been used for imaging the neural activation in the brain with a relative large field-of-view (46, 173) to extract the hemodynamic and metabolic parameters. For example, multiple interference of the reflected (or transmitted) wavelets is detected by LSCI methods (46), which is similar to taking snapshots of a series of pictures. However, they lack tomographic capability, thus cannot resolve functional vascularization in individual sub-layers of the cortical tissue. Optical microangiography (OMAG) is a label-free non-invasive imaging modality that can be used to obtain three-dimensional (3D) blood perfusion map within microcirculatory tissue beds *in vivo* based on Fourier-domain optical coherence tomography (FDOCT) (89, 116, 174-177). By quantifying the phase differences between adjacent A-lines, Doppler optical microangiography (DOMAG) is a functional extension of FDOCT/OMAG to image blood flow velocity within functional microvasculatures (178) . However, a tradeoff between the overall imaging area and sampling rate of DOMAG exists due to the point scanning manner and limited imaging speed. Here, we developed a SDWLS-OMAG system for brain imaging, which can overcome the disadvantages of each individual technique. We demonstrated that the system could efficiently extract not only two dimensional vasculature maps but also the depth-resolved layer to layer information in the meningeal layer and the somatosensory cortex in the mouse brain. (163)

3.3.2.2. System and methods (163)

Fig.18 (a) delineated the schematics of the integrated systems. The specific configurations are described in the previous section. Both lasers in the SDW-LSCI system were uniformly illuminated onto the sample at an incident angle of ~60 °(147). The exposure time of the camera was set to 10 ms, which was optimized to achieve high contrast for speckle flow imaging (94). Both of the cameras were running at 100 fps with each snapshot at dimension of 1000×1000 pixels. We set the field of view at ~9.5×9.5 mm^2 in order to cover the dimensions of the contralateral side of the mouse brain. For maximizing the contrast of the speckle pattern, this setting ensured the speckle size (~22 μm) to be approximately twice the pixel size (12 μm) (135). A super luminescent diode light source, with a central wavelength of 1310 nm, bandwidth 56 nm was employed for sample illumination in the OMAG system, which gives a theoretical axial resolution of ~13 μm in air. The camera in the spectrometer had a line scan rate of ~1.5 kHz. Each frame contained 500 A-lines that cover ~2.2 mm on the sample. A series of repeated B-scan images, called MB scans, were acquired at a frame rate of ~3 fps. It takes 42 seconds for acquiring a total MB-scan images. (163)

We have described the details of the pre-stimuli animal preparation including anesthesia procedure in (179). We made an incision with a~1.2 cm length cut on the skin along the direction of sagittal suture. The frontal parietal and interparietal bones were exposed. Here, the mouse cranium is neither thinned nor opened for imaging (174). Then, an electric stimulation mouse model was used for contralateral brain neural activation imaging through applying electrodes into the hind paw (180). We applied a 2 s pre-stimulus, 15 s stimuli with 0.5 mA current, and 25 s post-stimulus onto the mouse hind paw. The pulse frequency was 3 Hz and the pulse duration was 3 ms (181). The animal was then located under the scanning probe. Again, several parameters were calculated from the images captured by the multifunctional system for the evaluation of brain hemodynamic and metabolic responses. Firstly, the speckle contrast maps revealed functional blood flow within scanned tissue volume. The contrast map were calculated as a ratio of the standard deviation to the mean intensity rendered by moving a 5×5-pixel binning window in the raw intensity image at the wavelength of λ1=780 nm. Using the model of speckle contrast versus flow velocity, the relative flow changes can then be derived (157). Secondly, by using the images acquired with both λ1 (780nm) and λ2 (825 nm), the concentration changes of HbO, Hb, HbT and $CMRO_2$ were extracted (71,

147, 164). HbT was defined as the amount of hemoglobin (unit: millimole) per liter of blood, which is calculated as sum of HbO and Hb. By assuming a baseline concentration of Hb and HbT as 40 μM and 100 μM, respectively, $CMRO_2$ was extracted using the same approach described in (165). For localizing the brain region of hind paw stimulation, we extracted two regions. We defined the percentage of change in cerebral blood flow as in the range of 2% to 4% as the region 1, and the range of 2 μM to 3 μM of HbO change as region 2. We then overlapped the two anatomical regions for eliciting the specific activated region in the brain. The OMAG probe was then guided to image the details of vascular activations in this region after we had precisely localized the hind paw region in somatosensory region (SCR). We captured and processed the repeated OMAG B-scan frames in the localized SCR to achieve cross-sectional blood flow images using the DOMAG algorithm. (163)We finally estimated the flow velocities by calculating phase difference values between adjacent A-lines of flow signals (178).

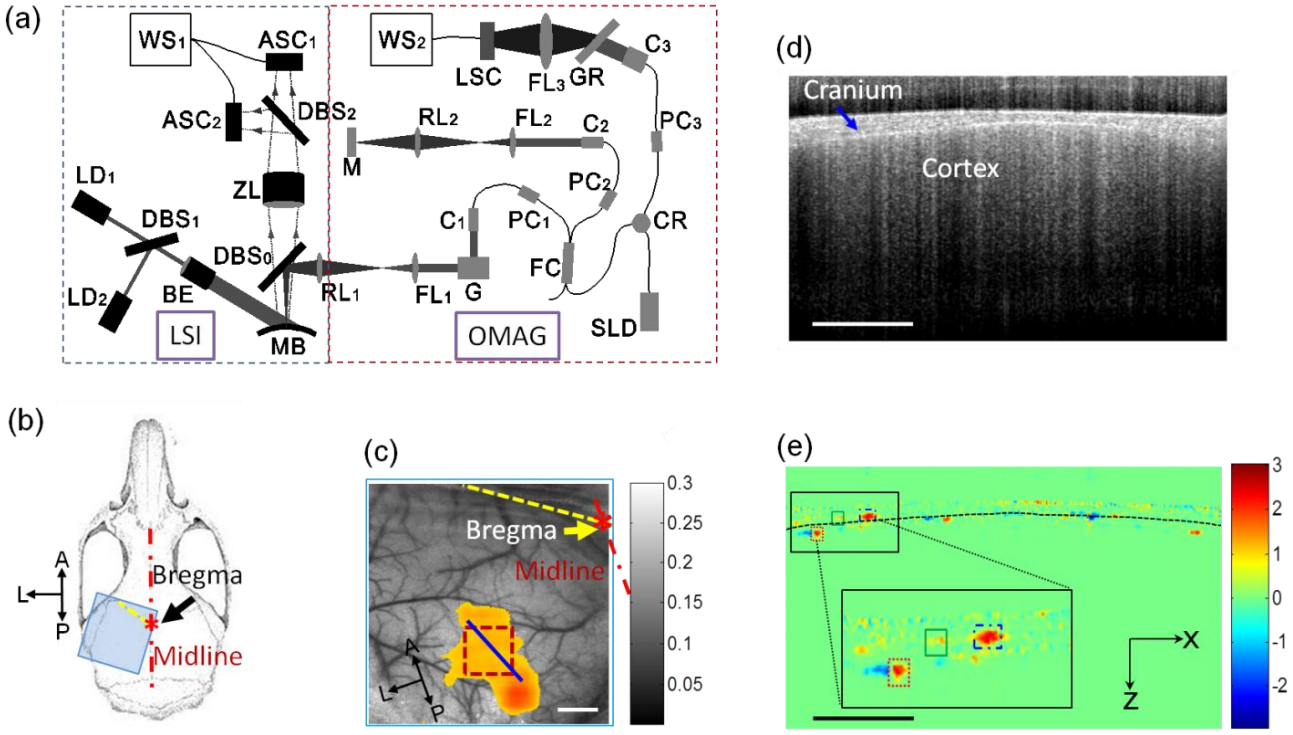

Figure 18 The SDWLS-OMAG system and representative blood vasculature images. (a) The schematic of the SDW-LSCI (marked by blue dotted square) and DOMAG (marked by red dotted square) system. LD: laser diode, DBS: dichroic beam splitter, BE: beam expander, ZL: zoom lens, ASC: area scan camera, WS: workstation, SLD: superluminescent diode, CR: circulator, FC: fiber coupler, PC: polarization controller, C: collimator, G: x-y galvanometer, FL: focusing lens, RL: relay lens, GR: grating, LSC: line scan camera, MB: mouse brain. (b) The imaging area in the contralateral (left) side of the brain. (c) The localized somatosensory cortex area (orange area) superposed on

SDW-LSCI speckle contrast image; the DOMAG repeated B scan region, marked by blue solid line; A: anterior, L: lateral, P: posterior. Scale bar: 1.0 mm. Bregma is marked by asterisk, and midline is marked by red dash-dot line, coronal suture is marked by yellow dash line in (b) and (c). (d) One typical DOMAG B-scan of microstructures showing morphological features, such as cranium and cortex. Scale bar: 500 μm. (e) DOMAG phase map showing the enlarged three typical regions of interest; blue dash-dot square: a large vessel in meningeal layer; green solid square: another vessel in meningeal layer; red dots square, a vessel in somatosensory cortex. The cortex layer and meningeal layer are separated by the black dash line. x: A-line scanning direction; z: normal direction to the mouse brain. Scale bar: 500 μm. (163)

We firstly obtained the hind paw region in the SCR by overlapping regions of R1 and R2. Then we overlaid the region onto the speckle contrast map. Typical branches (marked by the red spots) of the middle cerebral artery (MCA) and typical branches (marked by the blue spots) of the sagittal sinus can be visualized clearly. Anatomically, the MCA first arises from the internal carotid and projects to the portions of the lateral cerebral cortex. The functions of MCA and its branches are to supply the clusters of neurons, hind limb barrels in SCR. (182). Veins on the cortical surface mainly function to drain the SCR into the superior sagittal sinus. (163) The SCR is localized within the MCA and ACA anastomosis region which is in agreement with (182).

3.3.2.3. Results

One B-scan image within the DOMAG structural volume is shown in Fig.18 (d). In this image, typical morphological features, such as cranium and cortex, are visualized. A representative DOMAG phase map acquired during the stimulus is demonstrated in Fig.18 (e). Red color depicts the direction of the vertical flow component. The direction is consistent with that of the incident light. The blue color represents the opposite direction. We segmented the meningeal layer from the cortical layer using the method introduced in (174). The phase differences values of each B-scan frame were first integrated, normalized, and then plotted according to the captured time course for demonstration of the details of hemodynamic responses. Three ROIs were chosen, including a cortex vessel (~50 μm in diameter), a middle size meningeal vessel (~40 μm in diameter), which originates from dura mater from the depth 100 to 200 μm below the cranium surface, and a large meningeal vessel (~90 μm in diameter), respectively. (163)

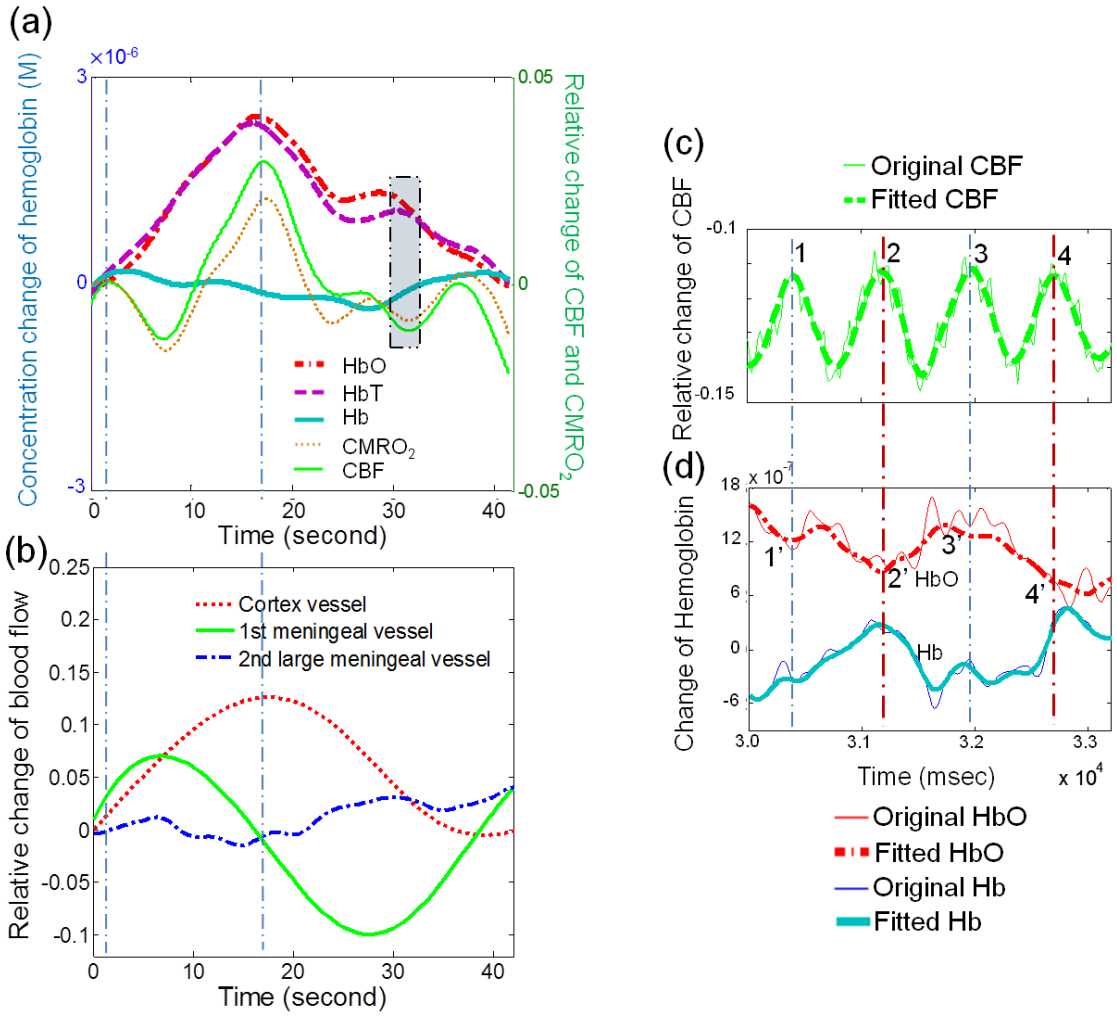

Figure 19 Time courses of the variances of CBF, $CMRO_2$, HbO, Hb, and HbT in the SCR before, during and after electrical stimulation. (a) Changes of all the five parameters depicted in the procedures of pre-, during and post-stimuli. The rectangular box shows the area enlarged for (c) and (d). (b) DOMAG flow changes in specific vessels. (c) The enlargement of the CBF curves shows a pulsatile trend (denoted by 1-4). (d) The enlargement of HbO and Hb curves show both the pulsatile and respiratory fluctuation. The pulsatile is denoted by 1'-4', which is corresponding to 1-4 in (c). (163)

The time courses of the relative changes of CBF, CMRO2 and changes of HbO, Hb and HbT are shown in Fig.19 (a). Each value is averaged from the vessels within a square region localized in the somatosensory area (Fig. 18 (b)) before, during, and after electrical stimulation. Except Hb, all the parameters raised to the peak values at ~17 s. The maximum decrease of Hb was observed behind the ridge wave of hyperemia; however, the change of Hb was not as obvious as those of other parameters. These trends are consistent with what was observed in (109). We also noted that an artery was situated within the SCR in our study while a vein was covered in it (95). The change in CBF was

greater than the change in CMRO2. It is also noteworthy that a secondary increase was shown in CBF, HbO, and HbT. This phenomenon indicates a delayed stress relaxation in the vessels (183). The magnified curves of CBF and concentration changes of HbO and Hb during 3.2 s time course of the recovery period (post-stimulus) are presented in Fig. 19 (c) and 19 (d). We can estimate the pulsatile frequency (~7.5 Hz) and respiratory frequency (~1.2 Hz) from the CBF and hemoglobin concentration changing curves using fast Fourier transform. So, the system has the feasibility to monitor the pattern of the oscillated pulsatile and respiratory frequencies in arteries and veins. The time course of the DOMAG flow-changing trend in the three typical vessels (marked in Fig. 18 (d)) is exhibited in Fig. 19 (b). The flow-changing pattern in the three vessels is obvious. The hemodynamic reconciling with propagating wave of hyperemia to the neural activation is shown by the cortex vessel (marked by the red dotted line in Fig. 19 (b)). A trend of flow increasing curve depicts the wave of hyperemia. The trend was similar to the propagating wave of hyperemia that SDW-LSCI showed. The big meningeal vessel exhibited totally different flow response with that in the cortex vessel. It is explicit that there was almost no flow change in the big meningeal vessel throughout the stimulus procedure. This big meningeal vessel may be a vein, which behavior not actively. The CBF in the other representative meningeal vessel (marked by the green solid line in Fig. 19 (b)) was innervated. (163) Therefore, it showed a oscillating pattern, which is probably caused by stimulated vascular tone (184).

3.3.2.4. Summarization

In summary, the multifunctional imaging system is useful in delineating the microvascular hemodynamic and metabolic responses in the cortex during peripheral neural activation. The system is advantageous in the ability of localizing 2D microvasculature responses. It is also useful in assessing depth-resolved single vessel flow responses. The SDW-LSCI is combined with OMAG for directly rendering images of any mouse model with local CBF and oxygenation variations. Therefore, it has the potential to explore a broad range of brain disorders, such as cerebral thrombosis and stroke, etc. (163)

3.3.3. SDWLS-OMAG utilized in monitoring the response of wound punch

We have proposed and developed a non-invasive biomedical optical imager, SDWLS-OMAG. The system was designed to maintain the performances of both subsystems. We need the capability of the system for simultaneously

imaging hemodynamic and metabolic responses in tissue environment *in vivo* with high image quality. To achieve such requirements, we optimized the optical designs here, such as we added additional relay lens to increase working distance and translational sample probe to select imaging area and focal plane freely; we also added paired dichroic mirrors to compensate dispersion. The multi-modelity of the system was demonstrated in a thorough investigation of hemodynamic and metabolic responses to an acute wound healing model in mouse pinna *in vivo*. The microvasculature, blood flow, and hemoglobin concentration from millimeter level down to single capillary were comprehensively visualized. The captured instantaneous responses to wound onset showed great differentiation between areas in the pinna tissue; a rebalance tendency was exhibited in the following blood flow response and simultaneously a dynamic recovery to baseline situation was revealed in the hemoglobin concentration variation.

3.3.3.1. Introduction

In this chapter, we utilize a combined system for quantitatively imaging hemodynamics and oxygen metabolism in a mouse wound healing model *in vivo*. We employ ultrahigh sensitive OMAG (UHS-OMAG) (89) and multi-range Doppler OMAG (mDOMAG) (162) to map the vascular response down to capillary level. The SDW-LSCI system provides relative flow velocity and hemoglobin concentration over the whole mouse pinna. A 3D translation stage is featured in carrying the OMAG probe to select the imaging area. Then, we position the focal plane without moving the animal. A relay lens plays an important role here. It is placed after the objective lens of OMAG, leaving the dichromic mirror as the solely shared component to avoid lens-introduced aberration to each other. Both the global and detailed hemodynamic and metabolic responses are demonstrated from the onset to ~40 min after punching.

Figure 20 Snapshot of a mouse pinna. The punched hole is marked by the dotted circles.

3.3.3.2. System and methods

We performed the wound punch experiment on a hairless mice pinna. The animal preparation was described elsewhere (101). A puncher with 1 mm diameter was pressed to the mouse pinna to punch a hole by removing ear tissue (shown in Fig. 20). First, both OMAG and SDW-LSCI baseline images were captured before creating the wound. We took snapshots of the SDW-LSCI images with 5.7×5.7 mm^2 at 1000×1000 pixels. We averaged twenty frames for the final SDW-LSCI image [Fig. 21(a3)]. We used the average of fifty frames as the baseline of HbO and Hb. To monitor the flow and hemoglobin concentration changes after wound, six regions of interest ROI1~6 were selected as representative areas at the upstream and downstream of an artery vein pair. The flow sensitivity of SDW-LSCI was calibrated as ~32 μm/s. We could have an overview of the mouse pinna vasculatures before the punch. We imaged a 2.2×4.2 mm^2 area [dashed in Fig. 21(a3)] located in the upstream using both UHS-OMAG and mDOMAG to investigate the fine vasculature system. This area was a mosaic of two 2.2×2.2 mm^2 tiles. The whole area was imaged one after another by shifting the OMAG probe for 2 mm. The 3D UHS-OMAG data set was composed by 512 pixels × 400 A-lines × 300 B-frames. With a frame rate of 170 Hz, each B-frame was high-pass filtered from 8 repeated frames. Fig. 21(a1) exhibits the maximum projection view of the 3D image. We performed mDOMAG mode with the A-line rate of 9 KHz for extracting slow flow velocity in the mouse pinna. We captured 25 A-lines at each position, followed by a waiting time of 7 A-lines before switching to another position. Each B-frame contained 200 positions, thus a frame rate of 1.13 Hz was yielded. We composed the whole 3D mDOMAG data set with 512 pixels × (25 A-lines × 200 positions) × 200 B-frames. We could capture blood flow whose axial velocity was within three ranges of [−2.2, 2.2], [−0.7, 0.7] and [−0.2, 0.2] mm/s by applying mDOMAG processing algorithm. The bidirectional maximum projection image of the data combined from different velocity ranges is demonstrated in Figure 21(a2). For achieving higher imaging contrast, we delineated the data in the range of [−0.7, 0.7] mm/s. To increase the velocity detectability, the pinna was titled for an angle of 10°, with that upstream is higher than the downstream. Hence, the red and green colors basically corresponded to flowing toward downstream and upstream, respectively. We denoted some typical arteries, veins and arterioles as A*n*, V*n* and AL*n*, respectively. A*n* and V*n* indicated the artery and vein of the *n*th pair, respectively. It is noteworthy that V4 appeared red, appearing the same as A4. We could estimate that a strong branch of V4 was flowing to converge with V2 and V3 via a bridge [white arrow

in Fig. 21(a2)]. Without external disturbance, this vein-to-vein connection was naturally formed. mDOMAG provided a detailed velocity map of all the main vessels overlaying in the mouse pinna.

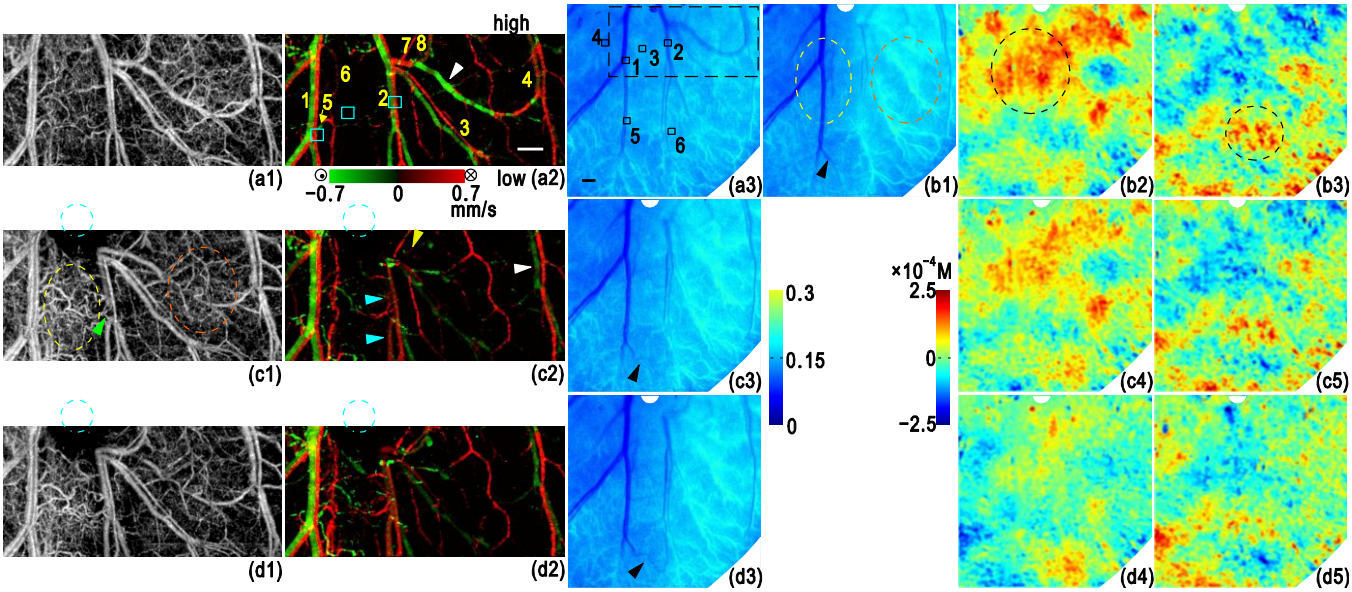

Figure 21 OMAG and SDW-LSCI images of the mouse pinna showing the acute wound healing process. (a1)-(a3) baseline UHS-OMAG, mDOMAG and SDW-LSCI images, respectively. (b1)-(b3) LSCI, HbO and Hb images, respectively, at 10 s after punching. (c1)-(c5) UHS-OMAG, mDOMAG, SDW-LSCI, HbO and Hb images, respectively, at 6 min after punching. (d*i*) is the same as (c*i*), but at 45 min after punching. The OMAG imaged area is dashed in (a3). The 0.5 mm biopsy punch is depicted as blue dashed circles in OMAG images and white notches in SDW-LSCI images. Scale bar, 400 μm.

3.3.3.3. Results

The SDW-LSCI, HbO and Hb images at 10 s after punching are shown in Figures 21(b1)-2(b3). The region that the 2nd, 3rd, and 4th vessels supplied (orange circle) showed a great reduction in blood flow. In the downstream region, the blood flow in a branch of V1 showed a trend for rescuing the wound region (marked by the black arrow). At the onsite of the wound punch, the upstream region exhibited higher concentration of HbO while the downstream appeared lacking of it. The Hb map showed an opposite phenomenon in downstream and upstream. From the onsite of the wound punch, we consistently captured the SDW-LSCI and OMAG images for 45 min. The images that were taken at 6 min after punching are shown in Figures 21(c1)-(c5). The UHS-OMAG provided the functional vascular response down to capillary level [Fig. 21(c1)]. There was almost no flow near the puncture. The main artery and vein that branch into the 3rd pairs were completely dysfunctional. The

increased flows between the 1st and 2nd pairs showed obvious capillary recruitment (marked by yellow circle in c1). Angiogenesis occurred around 3 days after wound onset (185). There was strong vessel dilation occurred in the 1st pair of vessel (186), which played the role of rescuing for the neighbor region. On the right of the puncture area, the vein bridged from V4 was interrupted and the capillary flow near it dropped dramatically (marked by orange circle). From the mDOMAG image [Fig. 21(c2)], the regions on the left and right sides of A2 show increased and decreased flow, respectively, which could be coregistered with UHS-OMAG images. The flow direction in V2 and its left branch (marked by blue arrows) appeared reversed. A2 was still flowing towards downstream due to the support from A7 and reversed A8 (yellow arrow), but A3 was interrupted. The flow direction of V4 (white arrow) was also reversed of A4 due to the interruption in its supporting bridge. There was no arterial-venous shunt that could be visualized, indicating that the artery and vein systems were still working independently. The SDW-LSCI image [Fig. 21(c3)] showed slower flow in almost all the areas than that at the onsite of punching, excluding the behaviors of the 2nd vessel pair and their branches. However, the phenomena of increase and decrease at the left and right side of the 2nd vessel pair, respectively is consistent with that appears in OMAG images. Moreover, the left branch of V2 was indistinctly connected to V1 via small capillaries, suggesting that V1 was the draining vein causing the reversed flow in the left branch of V2. The HbO and Hb images in Figs. 21(c4) and 2(c5) described a similar distribution as that at the onsite of punching. But it showed a tendency of hemoglobin concentration to return to baseline.

There was an overall recovery of blood flow comparing to 6 min after punching as shown in the UHS-OMAG image [Fig. 21(d1)]. The mDOMAG maps exhibited similar changes [Fig. 21(d2)]. For example, A8 became very strong to aid A7 for supplying A2 and A3. A clear connection showed up between V1 and the left branch of V2 (black arrow). We plotted the time courses from the ROIs in Fig. 22 for further elucidation of the wound process. The SDW-LSCI maps are shown with time interval of ~1.5 min. The mDOMAG maps are shown at time points of 6, 20, 32 and 45 min after punching. We employed an integration method of the flow velocities in the projection plane to better evaluate the response of absolute blood flow (83). For most of the non-reversed vessels, they showed a stronger flow after punching and maintained their levels [Fig. 22(a)]. The flow directions in V2 and V4 kept reversed through all the time after punch. The flow in AL5 was temporarily cut off at the onsite of punch, while came back with a strong overshoot. The functional vasculature behaved with the same trend with that in AL5. The blood flow changes in the selected ROIs in SDW-LSCI maps [Fig. 22(b)] showed instantaneous responses after punching, such as it showed flow reduction in ROI6 in downstream. ROI3 was located in the capillary recruitment region and appeared

with the strongest flow increase. The overall blood flow trend was consistent with that shown in the single-vessel captured by mDOMAG. For the hemoglobin concentration changes, the responses at the onsite of punching were also diversified. HbO in the upstream of ROIs showed a positive response while that in the downstream showed anegative response. However, their changing trends went back towards the baseline. The Hb response appeared as the opposite response with HbO.

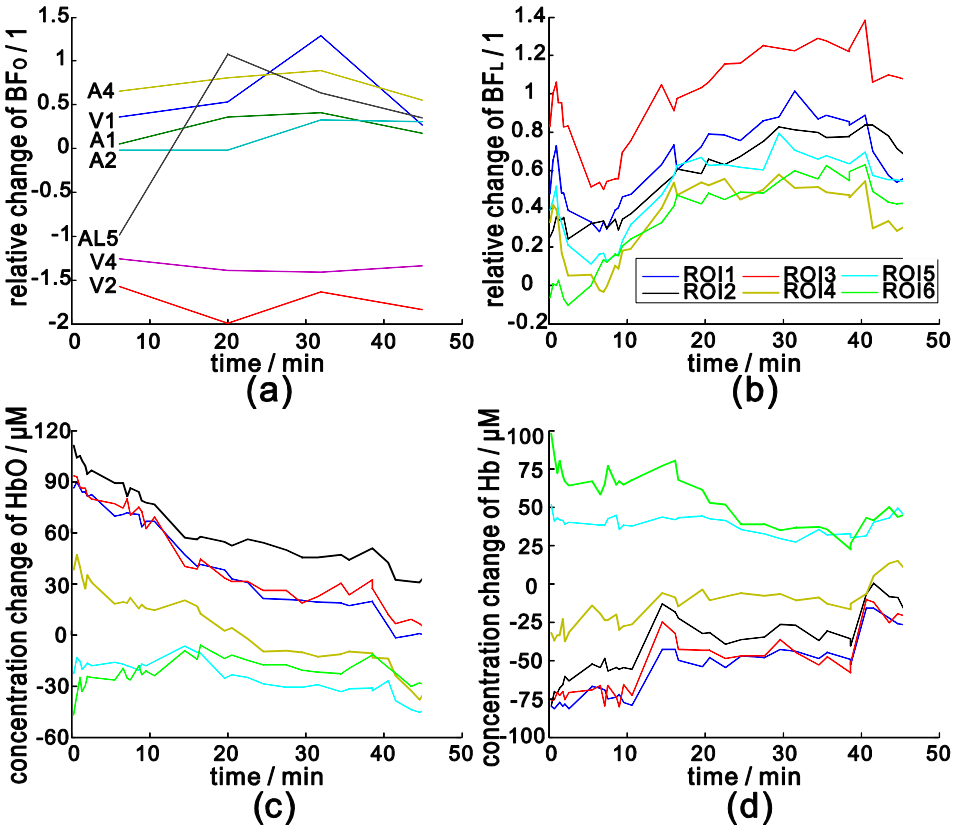

Figure 22 Time courses of the variations of blood flow and hemoglobin concentration after wound onset for selected vessels in ROIs. BF_O and BF_L: the blood flow calculated from mDOMAG and SDW-LSCI, respectively.

Except monitoring the short term tissue injury response, SDWLS-OMAG imager may also play an important role in chronic wound healing study. We could access more hemodynamic parameters, such as vessel diameter, length, density, tortuosity, fractal dimension and blood volume, which are critical to the analysis of angiogenesis and arteriogenesis. It would also be feasible to elucidate the oxygen consumption similar to the cerebral metabolic rate of oxygen using near-infrared spectroscopy (187). Those evaluations will contribute to better understanding of the complete wound healing process.

3.3.3.2. Summarization

In conclusion, this technique is able to quantify the detailed hemodynamic responses of wound punch. Such detailed vascular responses have not previously been able to be visualized using other techniques. Our techniques can greatly contribute to the investigation of vascular function in tissue injury.

3.4. Discussion

The SDWLS-OMAG system inevitably has some limitations. For example, the alignment of two cameras can be time consuming during the system development, compared to single camera systems. However, a USAF RES Target (resolution test pattern) could be employed as the sample for the alignment of the two cameras and coregistration of the two wavelength images. Thus, it does not hasve great influence onto our proposed work. An automatic images coregistration approach will be developed for more efficient implementation of future experiments. The major limitation of OMAG is that its imaging depth cannot be beyond 2 mm into the tissue. However, it is enough to image the mouse cortex through the cranium (1.0 mm to 2.0 mm) and the whole depth of mouse pinna (500 μm to 1.0 mm). Therefore, it does not influence the success of our study. A novel digital focusing approach can be implemented in order to automatically focus onto the en face section of the tissue to extend the depth of field. However, it needs to be implemented with prolix arithmetic.

Chapter 4. Determine the utility of multifunctional imaging system for serial monitoring of blood flow changes and vascular remodeling following experimental stroke in mice

The feasibility of the SDWLS-OMAG system has been demonstrated by our 2D large field-of-view, high temporal resolution and 3D high spatial resolution images filled with full set of information on tissue injury responses. The ability to non-invasively monitor and quantify hemodynamic responses down to the capillary level is important for improved diagnosis, treatment, and management of neurovascular disorders, including stroke. The SDWLS-OMAG system was used to evaluate vessel blood flow velocity and direction, vascular morphology, hemoglobin oxygenation, and cerebral blood volume, in experimental stroke induced by MCAO in mice. SDWLS-OMAG differentiated four distinct regions designated as infarct, peri-infarct, mild hypoperfusion and contralateral regions based on corresponding blood flow ranges during occlusion. In these regions, blood

volumes and typical vessel flows were distinguished and quantified. Furthermore, we characterized the contribution of different vascular compartments in generating and controlling the hemodynamic response. We found that the distal downstream arterioles reversed flow during occlusion, which may be important to mitigate and verse effects of vessel obstruction. The contents in this chapter are unpublished work. The manuscript is being prepared.

4.1. Introduction

Stroke is caused by blockage or rupture of a blood vessel supplying the brain with oxygen and nutrients. The reduction of cerebral blood flow (CBF) below critical values leads to a series of metabolic, functional, and structural changes resulting in irreversible neuronal death, i.e. infarct. Decreased blood flow beyond the critical value leading to infarct causes damage but this peri-infarct region has the potential for recovery. Over the past several decades, much effort has been put forth in investigating endogenous mechanisms involved in salvaging the peri-infarct region but has focused on neuroprotective mechanisms with little attention given to the vasculature. This is most likely due to the lack of a technology capable of elucidating real time microvascular dynamics *in vivo*. A more comprehensive understanding of microvascular responses and hemodynamic parameters during and after ischemic injury would greatly improve our ability to develop therapeutic interventions to improve vascular function and brain survival after stroke occurs. Currently there are no imaging techniques for experimental stroke that can non-invasively and simultaneously measure blood volume, velocity, direction and tissue oxygenation, and detect vascular remodeling (e.g. blood vessel deformation) down to capillary-level resolution at an appropriate imaging depth without the use of contrast agents in the microcirculation in vivo. To more comprehensively evaluate the microvascular responses to experimental stroke, we have developed the SDWLS-OMAG system. More recent improvements to OMAG allow detection of a wider range of fast and slow blood flow velocities for simultaneous measurement in capillaries, arterioles/venuals and arteries/veins (162). We employed UHS-OMAG (89) and multi-range Doppler OMAG (mDOMAG) (162) in our combined system to map the cerebral vascular response down to capillary level. SDW-LSCI improves on LSCI by the addition of a second camera. This creates faster imaging speed which can detect changes in oxygenated and deoxygenated hemoglobin concentrations and the relative changes in CBF in the mouse brain, within tens of milliseconds, through an intact cranium (147). Although SDW-LSCI is limited in depth, it can visualize a wide field-of-view (10 cmX10 cm) and accurately predict the area of infarct within a minute after an occlusion (188). SDWLS-OMAG is used to identify distinct blood flow regions corresponding to infarct, peri-infarct, and non-injured tissue and characterize the differences in vascular responses among them.

The multifunctional system detects microvascular responses with high spatial and temporal resolutions before during and after experimental stroke in male mice. In this work, SDW-LSCI enables rapid identification of CBF and hemoglobin oxygenation over the whole mouse brain and is used to guide the OMAG system to home in on depth information regarding blood volume, flow, and vascular architecture pertaining to defined regions of decreased CBF. SDWLS-OMAG provides a yet unparalleled tool to assess key dynamic information about cortical cerebral blood flow, which is important to understand the mechanisms relating to vascular injury and repair.

4.2. Material and method

For SDW-LSCI, we used the same protocol as described in section 3.1.1. For OMAG, we imaged 2×2 tiles of a 2.0×2.0 mm2 area to obtain a mosaic area of 3.6 × 3.6 mm2. At each position, 3-D volume data of both UHS-OMAG and mDOMAG were acquired. The 3D UHS-OMAG data was composed of 512 pixels×400 A-lines×400 B-frames. Each B-frame was high-pass filtered from eight repeated frames with a frame rate of 180 Hz. The blood flow sensitivity of UHS-OMAG was ~4 μm/s, which could resolve the complete vasculature morphology from arteries and veins down to the capillary level (89). Subsequently, we used mDOMAG for multi-range imaging of blood flow velocity. To extract the velocities ranged from arteries down to venules, we performed step scanning with the A-line rate of 75 KHz. 25 repeated A-lines were captured at each position. Each B-frame contained such 380 positions, yielding a frame rate of 6 Hz. The 3D mDOMAG data was composed of 512 pixels × 380 positions × 300 B-frames. The captured blood flow were within the axial velocity ranges of [-18.2, 18.2], [−6.1, 6.1] and [−2.0, 2.0] mm/s.

All experiments were carried out in accordance with National Institutes of Health guidelines for research animal care and the protocols were approved by the Institutional Animal Care and Use Committee of the University of Washington. Male mice C57BL/6J (Charles River Laboratories, Hollister, CA) approximately 8-10 weeks of age with body weights from 20-25 g were used in all experiments. Briefly, the animal was anesthetized with 1.5% isoflurane (0.2 L/min O2, 0.8 L/min air). The body temperature was maintained at 36.5±0.5 ℃ with a feedback rectal probe and heating pad (Harvard Apparatus). An incision of ~1.2 cm was made on the skin along the direction of sagittal suture and the frontal parietal and interparietal bones were exposed. It is worth mentioning that the mouse cranium was left intact, neither thinned nor opened for imaging (147, 179). The animal was then positioned under the SDWLS-OMAG imaging system. After the baseline imaging, a small laser Doppler probe

(Model moorVMS-LDF2, Moor Instruments Ltd., Oxford, England) was affixed to the right side of the skull at the mid-ear to eye distance to monitor cortical perfusion and verify vascular occlusion and reperfusion. A 6-0 nylon filament with a silicone-coated tip was inserted into the right internal carotid artery via the external carotid artery until the laser Doppler flowmetry value dropped to <25% of baseline. After 90 min of occlusion, the filament was removed and reperfusion was allowed to occur. Subcutaneous buprenorphine (0.05 mg/kg) was administered every 8-12 h until the time of euthanasia. To define and measure the region of infarct after imaging, at 24 h after reperfusion, brains were removed and stained whole with 1.2% TTC in saline at 37℃ and photographed to overlay with the whole field blood threshold values acquired with SDW-LSCI. Whole brains were then cut into 2 mm sections stained again with TTC and placed into 10% formalin overnight. Slices were photographed, and analyzed for infarction size with SigmaScan Pro 5.0 software (Systat Software Inc., San Jose, CA, USA). TTC is metabolized by viable cells to a pink color, which can clearly delineate the area of infarct as the area of pallor (189). Infarct volume was calculated by integrating infarcted areas across the rostral–caudal axis and expressed as a percentage of the contralateral hemisphere to account for edema.

The SDW-LSCI was utilized for assessing important hemodynamic and metabolism parameters, including the relative changes of blood flow, the changes in hemoglobin concentrations, blood flow direction and 3D blood vessel morphology. Briefly, we imaged the baseline, response to occlusion after 90 min and 20 min and 24 h after reperfusion.

Differences in oxy, deoxy and total hemoglobin concentration, vessel diameter, cerebral blood volume and flow were analyzed with repeated measure one-way ANOVA and with the post hoc Newman–Keuls test. The criterion for statistical significance was $p < 0.05$. All values are reported as mean ± SEM.

4.3. Results

In order to characterize the vascular responses to experimental stroke, male mice (n=5) were subjected to occlusion of the MCA by the intraluminal filament model (190). Baseline images were taken immediately before the MCAO surgery. MCAO was confirmed by laser Doppler flowmetry. After 90 min of occlusion the filament was removed on the imaging platform without moving the animal. After 24h the animals were imaged, animals euthanized and brains removed and stained with TTC for analysis of infarct size. The average infarct size was 46.65±14.24% and 39.94±10.61% in the cortex and total hemisphere, respectively. The mouse survival rate after surgery was 75%.

A reduction of blood flow below critical values leads to irreversible neuronal death, resulting in infarction (191). Reduced blood flow between determined values in the peri-infarct zone leads to reversible damage. Figure 23 shows the infarct core, peri-infarct, mild hypoperfusion and contralateral areas which were segmented based on computation of the ratio of blood flow during occlusion relative to that during baseline by SDW-LSCI. Blood flow percentages were calculated as the ratio of flow rate at 60 min of occlusion over the flow rate at baseline. Through further analysis, we were able to differentiate critical regions according to the magnitude of blood flow reduction during the period of occlusion. In the evaluated regions of five animals, the flow ranges were 92±2.1%-100% for the healthy tissue region (non-ischemic), 66±6.2%-92±2.1% for the region of mild hypoperfusion; 38±4.5% - 66±6.2% for the peri-infarct region, and 0-38±4.5% in the infarct core. The threshold flow maps can be consistently coregistered with the regions defined by TTC staining (192).

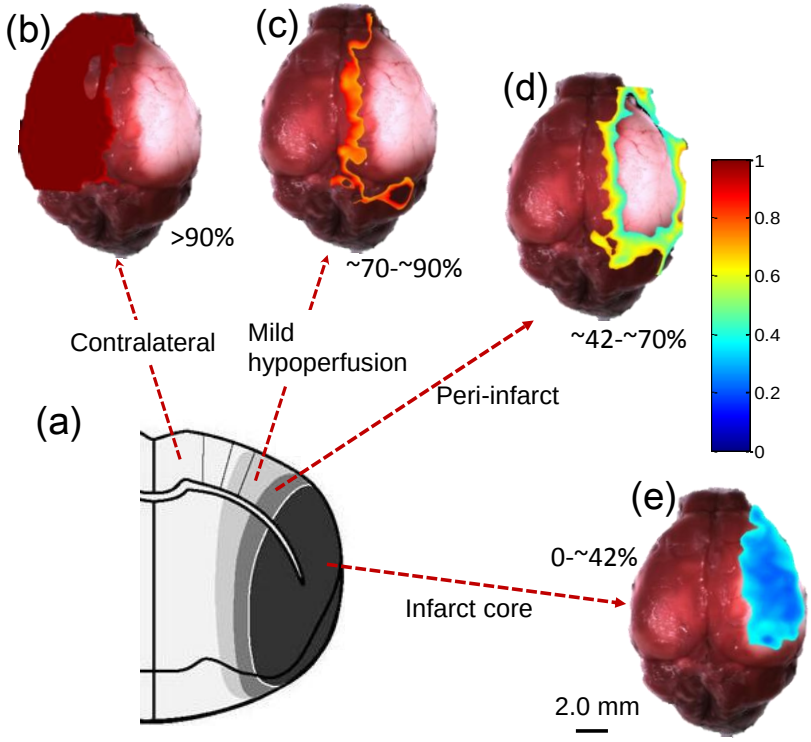

Figure 23 Blood flow thresholds used to differentiate infarct, peri-infarct, region of mild hypoperfusion, contralateral area in the mouse brain by SDW-LSCI. (a) Anatomical depiction of the four areas in MCAO model (193). (b) Evaluated contralateral region (flow rate >90% of control's); (c) region of mild hypoperfusion (flow rate ~70%-~90% of control's); (d) peri-infarct region (flow rate ~42%-~70% of control's); (e) Infarct core (0-~42% of control's), overlaid onto the snapshots of TTC staining in the mouse brain. Color bar represents the ratio of the ischemia flow relative to that of baseline. Scale bar denotes 2.0 mm. (n=5)

Regions and subtleties of dynamic cerebral blood flow (CBF) response; blood flow direction and vascular

remodeling before, during, and after MCAO were revealed by the SDWLS-OMAG system. SDW-LSCI captured a wide range of blood flow maps. The infarct core, marked by the dotted region, was estimated from Fig. 23(e) based on calculation of the flow rate during occlusion normalized to the baseline flow rate. During each time slot, a wide field of view of whole brain could be visualized. Prior to occlusion (baseline), blood flow in the right (ipsilateral) side of the brain was abundant, with an identical flow range to that of the left (contralateral) brain. During occlusion, the blood flow decreased most prominently in the core region (red, less than speckle contrast value of 0.16) of the MCA. A smaller peri-infarct region, surrounding the predicted core resulted in a less severe but marked decrease (yellow/green, speckle contrast values 0.10-.016). During reperfusion, the flow increased similarly over the entire hemisphere, with the infarct core and peri-infarct regions at similar levels. Vessel remodeling occurred in two surface meningeal vessels (marked by arrows in (c) and (d)) at 24 hours. The predicted core infarct area was validated by coregistering with TTC staining (data not shown). SDW-LSCI provided rapid identification of different tissue states based on variations of blood flow rates, and was used to guide OMAG for individual vessel investigation of morphology, blood flow, and flow direction.

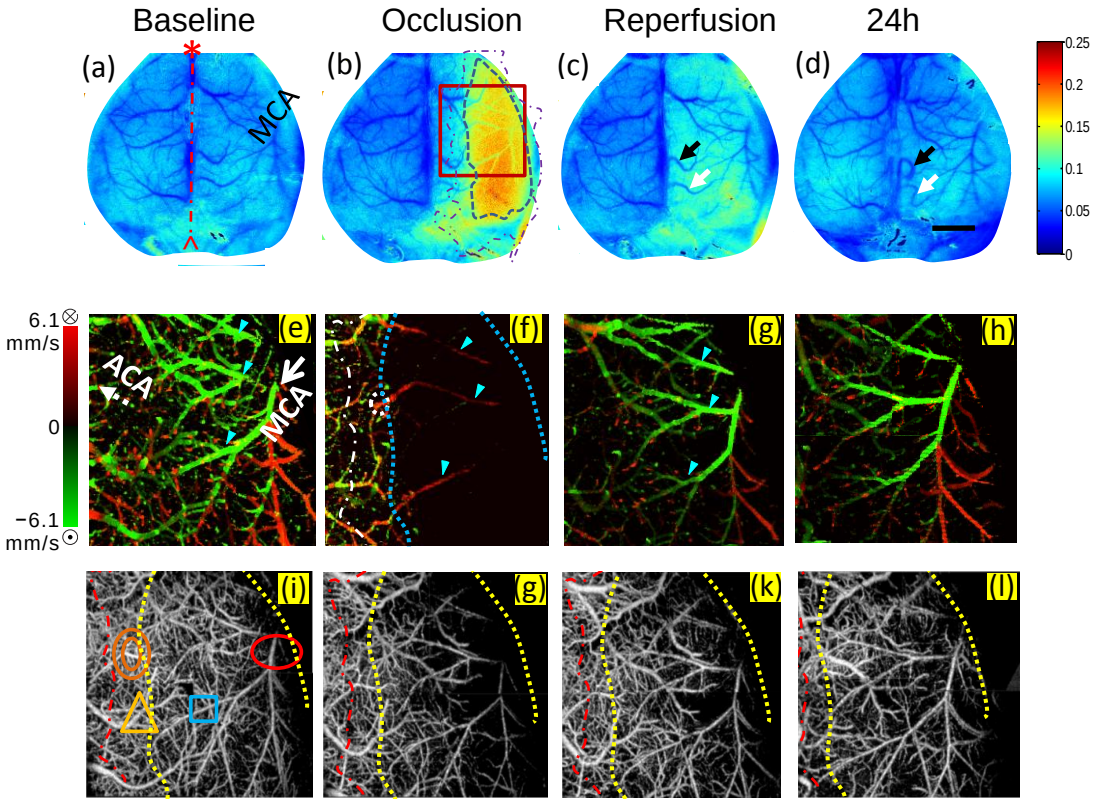

Figure 24 Representative laser speckle contrast maps (a-d), Doppler velocity (mDOMAG) (e-h) and vessel morphology maps (UHS-DOMAG) (i-l). The normal mouse brain (baseline a, e and i), 90 min (b,f, g) after onsite of occlusion, 20 min (c, g and k) and 24 h (d, h and l) after reperfusion, with the predicted infarct core marked by black dotted region in (b). In (a), the dash-dotted line denotes the midline of mouse brain; the asterisk and triangle indicate the anterior and posterior parts of the brain. The MCA territory is denoted in (a). The region of interest is marked by the red square in (b). A primary branch of MCA is marked by the large arrow in (e); a branch of anterior cerebral artery (ACA) is labeled by the dotted arrow in (e). Small arrows in (e), (f) and (g) label three branches of MCA. The dotted circle in (f) indicates the ACA-MCA anastomosis. The infarct region is marked by the yellow dotted lines in (i)-(l); the peri-infarct region is marked by the dash-dotted lines in (b), (f), and (i)-(l). In (i), the oval marks the MCA branch, the double-oval indicates the ACA branch, the triangle marked a vein, and the rectangular indicates an arterial branched from MCA. The color bars for (a-d) and (e-h) stand for speckle contrast and flow velocity, respectively. Scale bar in (d) for speckle contrast images is 2.0 mm. Scale bar for the OMAG images is 1.0 mm.

A similar observation was detected with a more detailed analysis with high resolution images of microcirculation up to 2 mm in depth by OMAG. OMAG is able to quantify blood flow down to the capillary level following ischemic stroke. Quantification of blood flow requires the assessment of flow velocity in individual vessels; however, the flow velocity within the cerebral cortex ranges from tens of μm/s in capillaries to tens of mm/s in the MCA. Here, we could distinguish the flow velocity and direction in individual blood vessels using mDOMAG (162). As observed with SDW-LSCI, the blood flow was drastically reduced in the predicted infarct core. Most interestingly, flow direction in three large arterioles (marked by small arrows in (e), (f) and (g) naturally formed anastomoses between ACA and MCA territories prior to stroke reversed during occlusion. The flow was recovered to the baseline direction at the onset of reperfusion and maintained the original baseline flow direction at 24 h post-reperfusion. The images of vascular morphology are also demonstrated in (i)-(l), from which we visualized the vascular architecture and morphology change of the blood vessels during occlusion and reperfusion in the mouse brain. Prior to occlusion, the capillary network was intact and dense. During occlusion, both large vessel and capillary blood flow in the infarct core regions decreased dramatically, as shown by the lack of observed vessels. The absence of the dense capillary network can be visualized at the time point of 24 h (l) relative to that of baseline (i). To the best of our knowledge, this is the first time this novel SDWLS-OMAG technique has been used to quantify the detailed blood flow responses, vessel by vessel within peri-infarct and infarct regions, when ischemic injury occurs, and

serially monitor vascular remodeling. Such detailed vascular responses have not previously been able to be visualized using other techniques.

The concentration change of HbO, Hb and HbT in the predicted regions of infarct, peri-infarct, mild hypoperfusion and contralateral regions are shown in Figure 25. The calculation was based on the comparison of HbO, Hb and HbT concentrations at reperfusion to that at occlusion. The change in hemoglobin oxygenation concentration in the infarct region was highest as this region has the lowest level of HbO during occlusion. The concentration change of HbO showed a decreasing trend (~0.12-~-0.08 mM) along the defined region from IF to PI, RF and CT. Deoxygenated Hb appeared a rising trend (~-0.2-~0.1 mM) at the time of reperfusion in the four regions. In the infarct region, Hb decreased and HbO increased remarkably, indicating that blood vessels were occupied by deoxygenated Hb during occlusion. This data suggests that hemoglobin remained as clots inside the vessel lumen during blood flow stasis were induced by MCAO. In the peri-infarct region, concentration of HbO remained relatively stable, whereas both Hb and HbT decreased. This phenomenon may be due to vessel constriction at the onset of reperfusion, and/or vasodilatation during occlusion in the peri-infarct region. In the mild hypoperfusion region, HbO showed mild decreases; HbT presented a tiny rising trend (~-0.065-~-0.01 mM). As the blood volume is linear proportional to HbT, the stability of HbT indicates stability of blood volume. An increase in Hb and decrease in HbO occurred in the contralateral region suggesting that upon reperfusion of the MCA oxygenated blood is also supplied by the contralateral hemisphere.

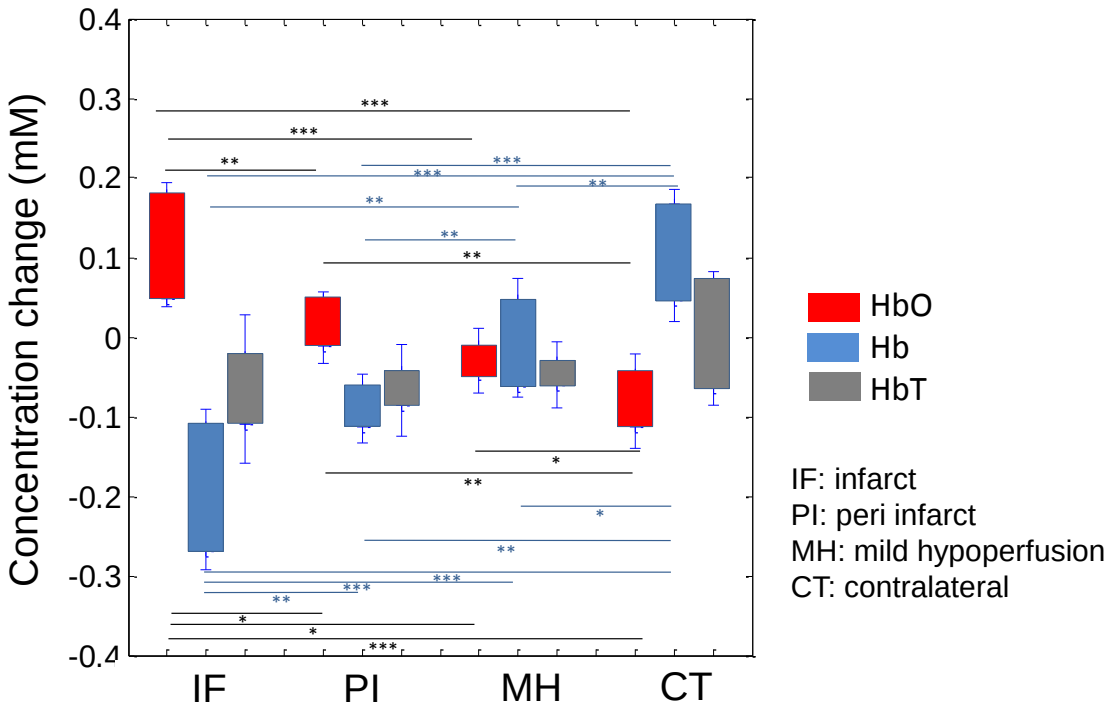

Figure 25 Concentration changes of HbO (red), Hb (blue), and HbT (grey) from time of occlusion to reperfusion. Means±S.E. Concentration changes were evaluated and measured by the SDW-LSCI subsystem. *p<0.05, **p<0.01, ***p<0.001.

Overall, the function of SDW-LSCI is important for a whole brain imaging because it may provide rapid identifications of different tissue states based on variations of blood flow rate, which can be used to guide OMAG for vessel-to-vessel investigation of morphology, blood flow and direction.

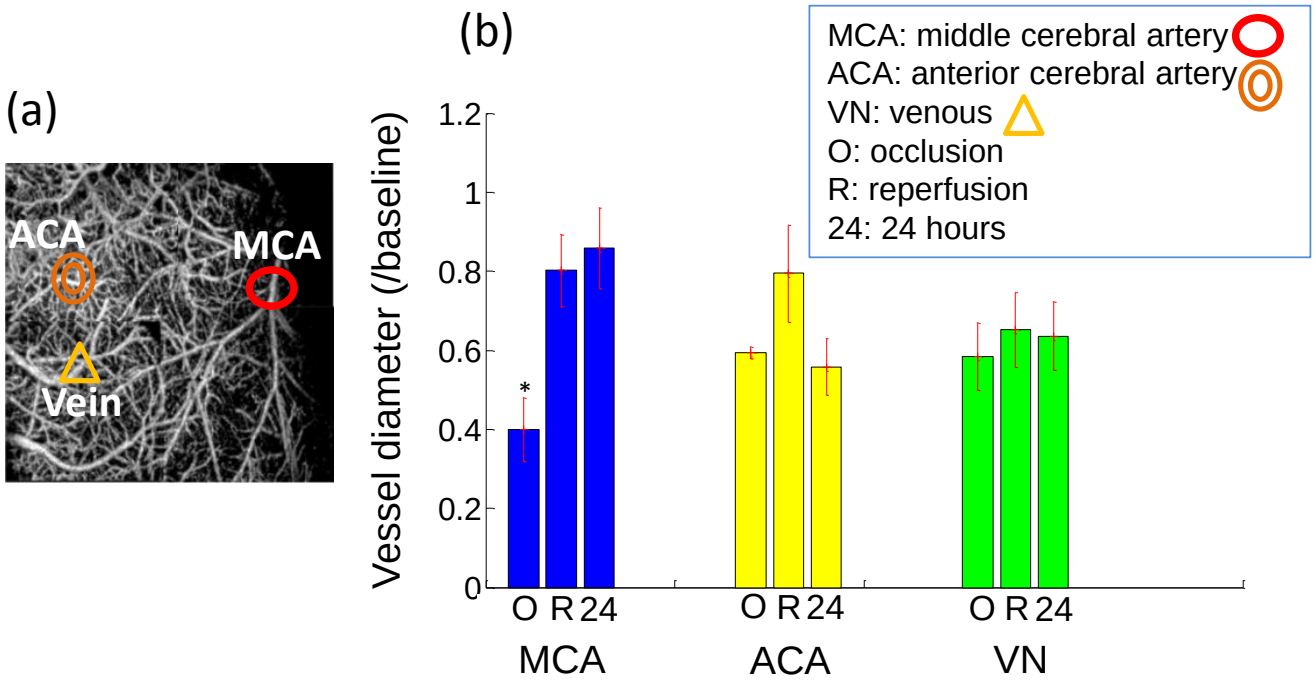

Figure 26 (a) Representative blood vessels image, demonstrating the vessels type that we selected. The image is a representative vessel morphology map, extracted by UHS-OMAG. (b) Vascular diameter changes during occlusion, reperfusion, and at 24 hours after MCAO. Values in graphs are expressed as diameter change in cerebral vessels, including middle cerebral artery, anterior cerebral artery and venules, during the time course in the mouse brain subjected to MCAO and presented as means ± S.E. (n=5). In MCA, occlusion vessel diameter is significantly different with that of reperfusion and 24 hours (*p<0.05).

The vessel diameter (shown in Fig. 26) was collapsed to ~40% during occlusion in the MCA, reperfused to ~80% and recovered to ~83% of baseline. The vessel diameter was reduced to ~58% during occlusion in the ACA, reperfused to ~79% and reduced again to ~55% of baseline. While the vessel diameter in the vein was steady around 55%-62% during the time courses of occlusion, reperfusion, and 24 hours later. We can estimate that ACA plays the role in rescuing the ischemic regions in the MCA territory.

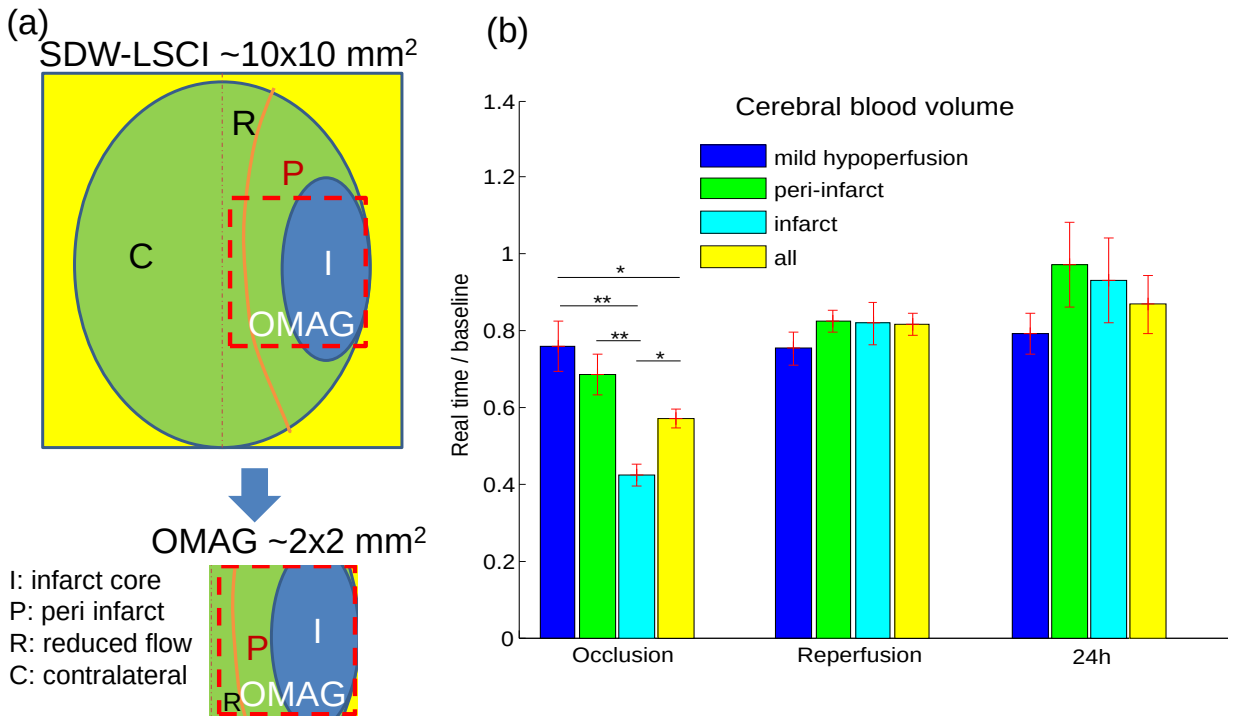

Figure 27 (a) Graphs delineating the correlation between imaging regions by SDW-LSCI and OMAG. The infarct core (I), peri-infarct (P), mild hypoperfusion (R), and contralateral regions (C) are marked in the imaging regions. (b) The UHS-OMAG imaged blood volume responses in three major functional regions during occlusion and after reperfusion. The regions are

defined from the threshold regions by SDW-LSCI. For all these areas the blood volume increased from occlusion time slot to 24 hours after reperfusion. All the data are normalized to baseline (n=5). Newman-Keuls Multiple Comparison Test: *$p<0.05$, **$p<0.01$.

Cerebral blood volume was calculated by thresholding the UHS-OMAG data, which was sensitive enough to capture blood flow from arteries and veins down to the capillary level. At the stage of occlusion, the regions from mild hypoperfusion to infarct suffered from stronger and stronger reduction in blood volume. Due to the occlusion of MCA, the CBV reduction in infarct region was severe; down to 42% of baseline. Peri-infarct and mild hypoperfusion regions have reductions of 68% and 76% of baseline, respectively. The standard error of BV in peri-infarct and mild hypoperfusion areas were larger than that of infarct area, indicating higher fluctuation in their vasculatures in response to occlusion. These data are consistent with those calculated by SDW-LSCI. During reperfusion, strong blood flow in the MCA led to the recovery of CBV in infarct and peri-infarct areas, ~82% and 83% of its individual baseline. Changes in the mild hypoperfusion region were minimal possibly because it was at the farthest distance from the MCA. The regions of mild hypoperfusion, peri-infarct, infarct and the whole of them maintained similar reperfusion values, approximately 80% of baseline, illustrating the reperfusion effectiveness in the whole cerebral vasculature system. At 24 hours after reperfusion, the blood volume in the peri-infarct was highest at 97% of baseline. The strong perfusion occurred in various types of vessels, such as arteries, veins and capillaries. The blood volume in the infarct area recovered to 93% of baseline, mainly due to the perfusion in MCA and its arterioles rather than the capillaries; the mild hypoperfusion area remained stable at 79%, just slightly higher than occlusion and reperfusion. Due to the long-term compensatory variation among animals, the standard errors of blood volume in peri-infarct and infarct regions were much larger than the previous time points.

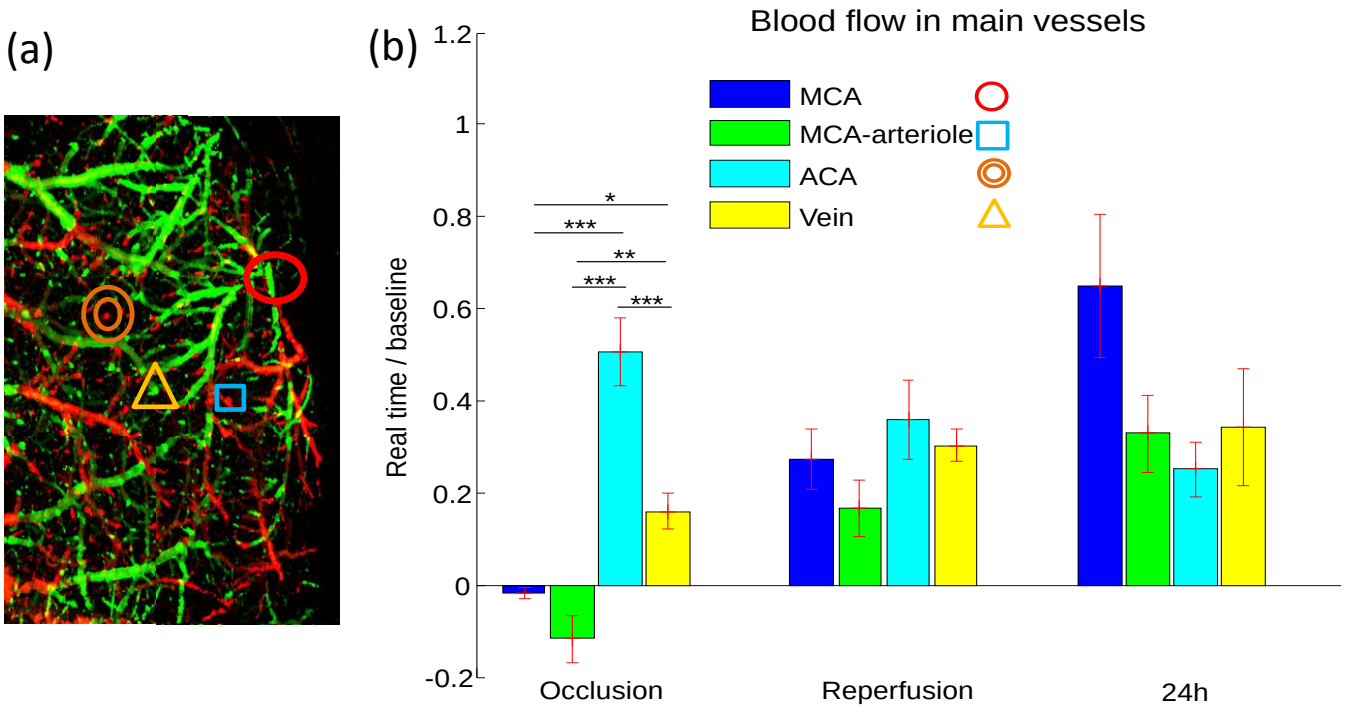

Figure 28 (a) Representative blood vessels, demonstrating the vessels type that we selected. The image is a representative blood flow map, extracted by mDOMAG. (b) The mDOMAG imaged blood flow responses in four main vessels during the procedure of MCAO. The selected vessels are the MCA, the arteriole of the MCA, the ACA and a large vein. These representative vessels are marked in (a). The arteriole of MCA connects to the arteriole of ACA via anastomosis. The large vein is the direct branch of the superior sagittal sinus vein. Flow reversal in the MCA and its arteriole was observed during occlusion. Then they returned to the original direction upon reperfusion. All the data are normalized to baseline (n=5). Newman-Keuls Multiple Comparison Test: *p<0.05, **p<0.01, ***p<0.001.

The blood flow in main vessels (shown in Fig. 28) was calculated by integrating the axial velocity signals at a specific *en face* plane of each vessel from the mDOMAG data. This calculation can determine the absolute blood flow without knowing the Doppler angle between the vessel and light directions. As expected, occlusion reduced blood flow in the MCA almost to zero. However, with the extended detection range of mDOMAG, we precisely captured the remaining weak flow in MCA, which was -1.7% of baseline. The negative value here means that the flow direction was from the arteriole of MCA towards MCA. It was reversed when comparing to baseline. This phenomenon came from the compensation of blood flow from ACA via the anastomoses between the arterioles of the ACA and MCA. Flow reversal also occurred in the large arterioles of MCA, about -12% of baseline, which was stronger than in the MCA as they were closer to the ACA. The flow in the ACA during occlusion was also reduced, to half of baseline. The ACA potentially served as the salvage artery to the areas originally supplied by the MCA.

The vein was greatly reduced due to the overall reduction in the supply from arteries. After the onset of reperfusion, the MCA and its arteriole recovered to the normal flow direction, but the flow was very weak compared to baseline. At the time point of 24 hours after reperfusion, the MCA and its arteriole recovered more, approximately 65% and 33% of baseline, respectively. The blood flow to the ACA was further reduced, with only 25% of baseline; and the blood flow to the vein was increased from the onset of occlusion to 24 h hours after reperfusion. Due to the long-term compensatory variation among animals, the standard error of blood flow in these main vessels, except ACA, was much higher at the 24 h time point.

Overall, SDWLS-OMAG may improve our understanding of vascular responses under pathologic and physiological conditions, and ultimately facilitate clinical diagnosis, monitoring, and therapeutic interventions of neurovascular diseases.

Chapter 5. Future work

Currently, the 1stG and 2ndG systems have been developed and the utilizations of the systems have been demonstrated. In the future, we will optimize the analysis and algorithms for quantifying capillary recruitment, blood flow, oxygenation, blood vessel remodeling, tortuosity and flow direction, etc. We will also improve the functions of the system for acquiring higher quality images in the regions of interest.

5.1 SDWLS-OMAG imaging for long term assessment of vasculature

The future direction of this project is: long term investigation of microvascular reorganization followed by ischemic injury. I will use endogenous vasodilators (e.g. EETs) to regulate the CBF. Currently, it is still unclear whether applying overdose of EETs can improve the cerebral vascular structure and increase angiogenesis in long term. We will determine the usefulness of SDWLS-OMAG for long term peri-infarct evolution in blood flow and vascular remodeling after a focal brain ischemia between untreated mice and mice that are given therapeutic interventions. The hypothesis is that higher level of therapeutic interventions will result in more neovascularization and smaller peri-infarct area compared with untreated controls. The vessel density, fractal dimension, and histological quantification of cell numbers positive markers that indicate angiogenesis will be assessed. We will track and compare SDWLS-OMAG images with the terminal histological endpoints in the same animal with imaging points

at 24 h, 96 h, 7 days, 14 days, and 20 days. A significant number of mice to establish a correlation between SDWLS-OMAG images of microvasculature and histological assessments will be used because the histological analysis is an end-point assessment technique. Furthermore, neural stimulation will be performed on stroked mouse. Using electrical currents, functional electrical stimulation will activate nerves innervating extremities affected by paralysis resulting from stroke or other neurological disorders. We will monitor the neurovascular response followed by neural activation in stroked mouse.

5.2. Depth Enhanced Cerebral Blood Flow Imaging Using Optical Microangiography

Conventional fixed-focal-plane imaging schemes for mouse brain are limited in depth of focus, particularly when imaging three-dimensional volumes in deep mouse brain using objective lens with high numerical aperture. We demonstrated a shifting-focus approach in our OMAG technique, achieving fast localization of multiple depths of view by translating the sample probe to select imaging areas in the axial direction freely. By focusing beam at different layers within the mouse brain, backscattered signals from these regions could be uniquely separated. A mouse model of cranial window was used to demonstrate the capability of OMAG for imaging the microvasculature morphology and Doppler blood flow in the mouse brain with high quality. This approach allows in vivo imaging in multiple focal planes within and even underneath the living neocortex using intrinsic contrast. It will benefit the study of hemodynamics in experimental models within deep brain.

5.2.1. Introduction

To differentiate the cerebral blood flow in multiple layers is crucial for localizing the abnormalities during diagnosing and treating cortical diseases. Two-dimensional imaging methods, such as LSCI (41, 46, 194), is capable of measuring blood flow in the surface of the neocortex; however, they are deficient in the resolution to detect capillary beds, and they lack the capability to image deeper cortical layers (70). Other blood flow imagings, such as two-photon imaging (195, 196), have been used in ultrahigh-resolution brain imaging over the past decades. However, the penetration depth remains limited to a few hundred microns, and typically, exogenous dyes are required (197, 198). Combined fluorescence intravital microscopy, dynamic light scattering, and spectrally enhanced microscopy modalities (54), also require the injections of contrast agents, which may cause side effects and put patients at risk. Magnetic resonance imaging (55) is able to image the whole brain. However, the spatiotemporal resolution is relatively low. OCT (56) has revolutionized *in vivo* brain imaging using intrinsic contrast, i.e. contrast arising from endogenous properties of biological tissue. However, the normally utilized fixed-focal-plane (FFP) method sacrificed the imaging quality where the sample position was out of the depth of focus. Recent approaches to fast volumetric high-resolution microscopy have included optical coherence microscopy.

However, the field-of-view and depth of focus are relatively low because of the ultrahigh numerical aperture (199). In addition, flow velocity cannot be extracted using this approach. Here, we present a novel strategy for deep brain imaging using OMAG

(101, 174, 176). In conventional OMAG system setup, it is problematic that the image degraded seriously within the region outside the depth of focus. Here, we use a flexible sample probe to progressively scan through the tissue of interests step by step. Therefore, 3-D volumes in a large depth of view could be accessed and precisely maintained within the depth of focus. This approach is termed the Multi-Focal-Plane (MFP) scanning method. By using the combination of hardware rendered flexibly positioning and software rendered selective data processing, deep brain tissue can be accessed and the efficiency of data analysis is improved. We have demonstrated that OMAG could separate signals originating from multiple depths in the living brain, and could achieve unprecedented image quality using MFP method. We also compared microvasculature morphology images acquired by MFP method with those by conventional FFP method. An image with wide field-of-view is also presented using FFP method. This is the first time for OMAG to map the vasculature morphology and flow velocity through the craniotomy cortex down to capillary level.

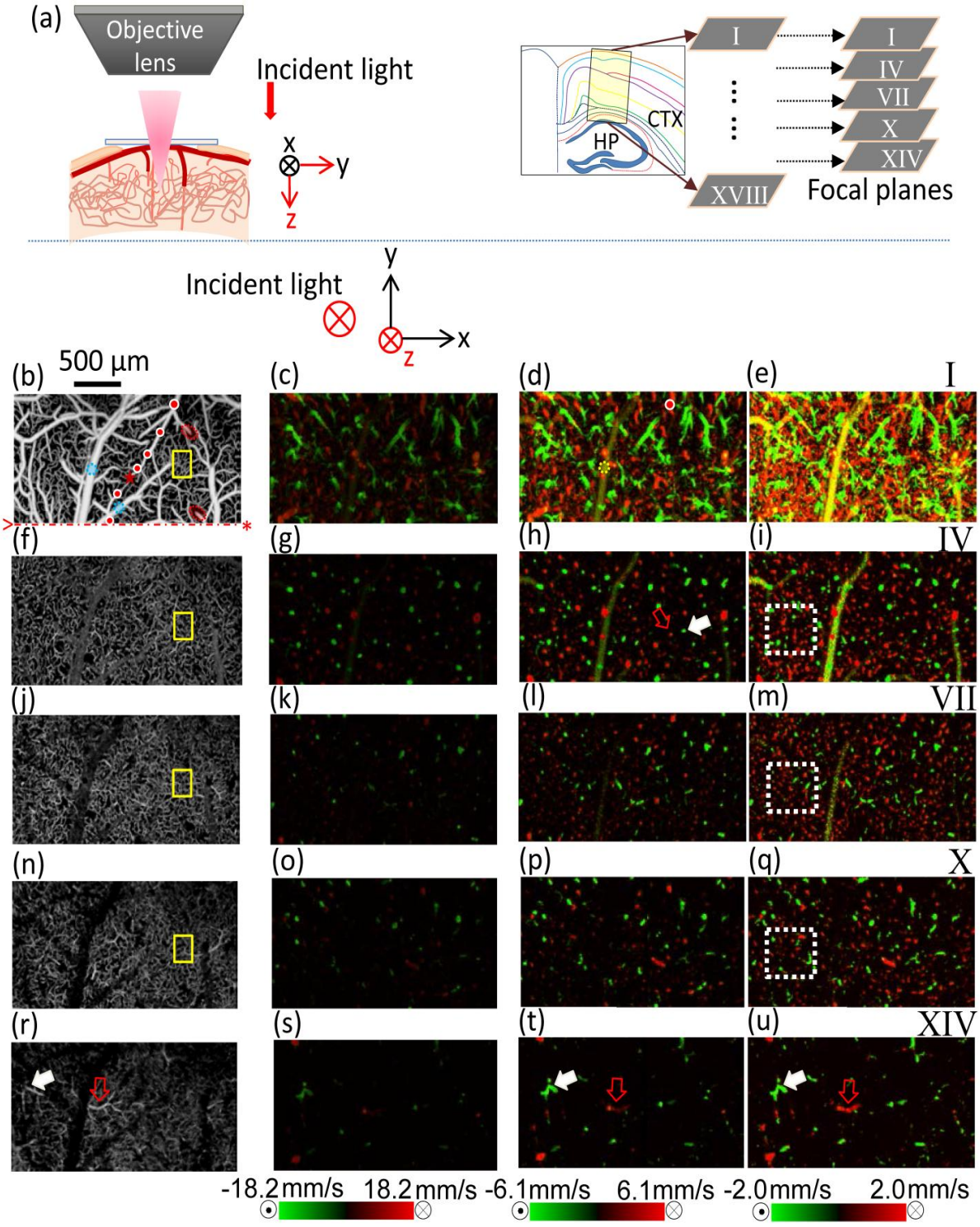

Figure 29 Imaging configuration and multi-focal-plane method highlights advantages of in vivo imaging microcirculation and blood flow from surface to deeper layers in mouse brain using UHS-OMAG and mDOMAG. (a) Left: brain imaging configuration. The scanning beam is focused from the planes with larger surface vessels to the planes of deeper diving vessels and capillaries; right: imaging configuration with

delineation of layers in the neocortex. CTX: cortex, HP: hippocampus. (b)-(u), representative morphology and Doppler blood flow images in layers I, IV, VII, X, and XIV. The first column: blood vessel morphology; the other three columns (from left to right): Doppler flow with the velocity ranges of -18.2 mm/s to 18.2 mm/s, -6.1 mm/s to 6.1 mm/s and -2.0 mm/s to 2/0 mm/s. In image (b) and (d), typical arteries are marked by the red solid dots; typical veins are marked by the blue dotted circles; typical diving vessels are marked by the red dotted oval; representative anastomosis is marked by the star. In (b), the red dot-dash line indicates the midline; the anterior side is indicated by an asterisk; the posterior side is indicated by a triangle. The yellow squares in (b), (f), (j) and (n), mark regions of capillary beds at different layers. Typical arteries and venous are visualized as "tiny spots", such as the ones indicated by the white dotted rectangle in (i), (m) and (q). The green tiny spots denote the arterioles, with the direction of the flow towards the deeper layers of the neocortex; the red dots indicate the venous, with the direction of the flow toward neocortex surface. The white solid and red hollow arrows in (r), (t) and (u), respectively point to a typical feeding artery with flow direction towards hippocampus, and a typical draining vein with the opposite flow direction.

5.2.2. Materials and Methods

Optimal cranial window surgeries are critical for deep neocortex imaging. Briefly, the mouse was anesthetized with isoflurane (1.5%) by a face mask. After that, its head was firmly fixed with ear bars in a stereotaxic frame. A craniotomy surgery was performed using a saline cooled dental drill and a ~4.0 mm diameter area over the cortex was exposed. The dura was carefully removed, and then the brain surface was covered with a glass cover slip and sealed with cyanoacrylate based glue (200). Immediately after surgery, animals were moved to our imaging system.

The experimental system used in our studies is shown in (164). The OMAG was working at a central wavelength of 1340 nm with a bandwidth of 110 nm; the integrated LSCI system was working at 780 nm. The imaging geometry is shown in Fig. 29(a). The light passes through the glass cover slip, went down into the brain and then is reflected back. The whole OMAG probe assembly was translated axially to change the focal position. To investigate the fine vasculature system, we imaged a 1.3×2.3 mm2 area within the cranial window (a bone flap is removed from the skull to access the brain) using both UHS-OMAG (89) and mDOMAG (24). This area was a mosaic of two 1.3×1.3 mm2 tiles that were imaged one after another by laterally shifting the OMAG probe for 1.0 mm. During data acquisition of each tile, the focal position started from just above the cortical surface, and then translated down into the brain at increments of 43 μm. At each focus position a 3-D volume data was acquired. The 3D UHS-OMAG data was composed of 512 pixels×400 A-lines×400 B-frames. Each B-frame was high-pass filtered from eight repeated frames with a frame rate of 180 Hz. The B frames were reconstructed in post-processing using the method in (175). Subsequently, we used mDOMAG (24) for multi-range imaging of blood flow velocity. To extract the velocities ranged

from artery down to venule, we performed step scanning with the A-line rate of 75 KHz. 25 repeated A-lines were captured at each position. Each B-frame contained such 380 positions, yielding a frame rate of 3 Hz. The 3D mDOMAG data was composed of 512 pixels×380 positions×300 B-frames. The captured blood flow was within the axial velocity ranges of [-18.2, 18.2], [−6.1, 6.1] and [−2.0, 2.0] mm/s. The systematically integrated LSCI (107) served to capture the whole profile of the cranial window, for better positioning the overall imaging area. We adjusted the LSCI system with a field of view of ~4.2×4.2 mm2 to fit the size of cranial window. The temporal speckle contrast maps were calculated as the ratio of the standard deviation to the mean intensity for each single pixel along every 30 frames (147).

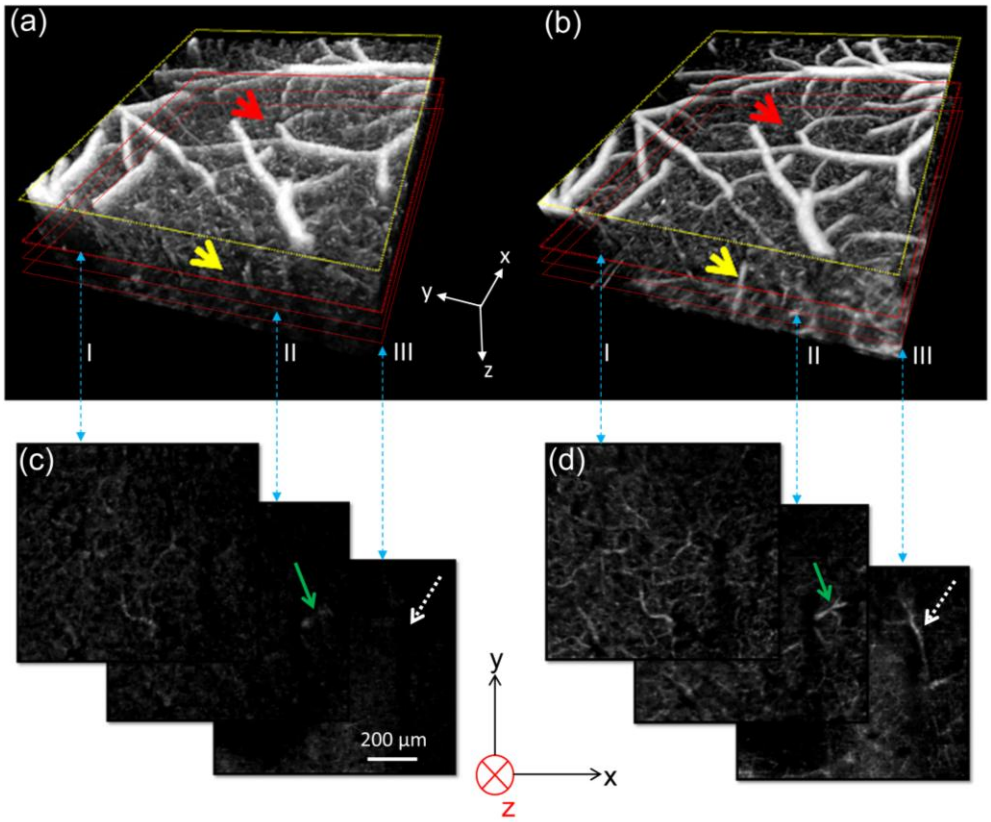

Figure 30 *In vivo* OMAG images of mouse brain through a region of cranial window. (a) and (b), Three-dimensional rendering comparing FFP and MFP methods, respectively. The 3D vasculature map appears with higher quality in the MFP data set. Arrows in (a) and (b) mark some typical vessels for comparison. (c) and (d), representative *en face* planes corresponding to the planes marked by the red dotted squares in (a) and (b), respectively. The dotted arrows and numbers I, II and III, connect and denote the matching planes. Arrows in (c) and (d) point to some typical vessels under comparison. Scale bar: 200 μm.

5.2.3. Results

Blood vessels within this area of the mouse brain loop and connect in complex ways. Figure 29(b)-(u) shows the mouse brain vascular images captured using the MFP method. From the surface of the neocortex down to the deep brain, we captured 18 MFP 3D volumes. The projection view images captured at the depths of 0-43 μm, 130-172 μm, 259-301 μm, 474-516 μm, and 603-645 μm are presented. It is noteworthy that the capillary network can be clearly differentiated in these maps (e.g., marked by squares in Figs. 29(b), (f), (g) and (n)). These tiny capillary vessels deliver oxygen and nutrients to energy-hungry brain cells and carry away wastes. We could extract the artery and vein based on the flow direction shown in Doppler flow images flying through different focal positions. For example, in Fig. 29(d), the blood vessel marked by a solid spot represents the flow went from a surface loop and connect to deeper blood vessels. It is also notable that there were numerous arterioles and venules connecting the main surface vessels to the deeper capillary loops. For example, the white solid arrow in Fig. 29(f) indicates blood vessel with the flow going from the surface of neocortex towards deeper brain. It demonstrates that it was a "diving arteriole" feeding the deeper brain tissue. In the dotted rectangle in mDOMAG maps Fig. 29(i), (m) and (q), there are diving and ascending vessels shaped as "tiny spots", with the flow directions explicitly exhibited. These "tiny spots" are arterioles and venules located in the second, third, and fourth layers, termed anatomically, the external granular layer, the external pyramidal layer, and the internal granular layer, respectively, in the neocortex (201). As a part of the neocortex, the area that we imaged is fed by arteries that plunge from the surface of the brain and is drained by veins that return from the deep brain to the surface. It is also noticeable that the vascular architecture is translated from capillary loops dominated layers (IV, VII and X) to larger feeding vessels dominated layers (XIV). For example, one feeding artery (marked by the white solid arrows in Figs. 30(r), (t) and (u)) and one draining vein (marked by red hollow arrows in Figs. 29(r), (t) and (u)) showed up when the "flying through" projection maps went through layer XIV. The artery and vein connects the neocortex and hippocampus, which belongs to the limbic system and plays important roles in the consolidation of information from short-term memory to long-term memory and spatial navigation. The artery provides nutrition for the hippocampus and the vein drains back the nutrition consumed blood. By figuring out the vascular architecture within the deep brain, it may benefit the study of capillary response in diagnosis of early neurovascular diseases (202).

Acquisition of deep tissue measurements is challenging for FFP method, because of the limitation of the depth of focus. Our MFP data acquisition method could enhance the well-focused imaging depth. Figure 30 demonstrate that the microvasculature

is much more clearly visible using MFP method. For example, the typical vessels, pointed by red and yellow arrows, show that they can be visualized by the MFP but not by the FFP approach. To further demonstrate, a series of *en face* views were chosen and compared in Figs. 30(c) and 30(d) corresponding to the marked planes in Figs. 30 (a) and (b), respectively ((I), (II) and (III)). Fig. 30(d) shows more abundant capillary loops than Fig. 30(c). This phenomenon is more obvious when the deeper layers are compared. Overall, we have observed that with the MPF method, the image quality is dramatically improved. We attribute this to the enhanced collection of singly backscattered light when the focus is placed deep in the sample. In Fig. 31(a), the conventional microscopy image can only show some large surface blood vessels without the capillary loops. In the cross-sectional FFP OMAG image with cranial window [Fig. 31(d)], the deeper blood vessels and capillaries are more explicit, comparing with those in cross-sectional FFP image with skull [Fig. 31(c)]. Furthermore, the high quality capillary loop profiles (marked by oval and rectangle) are able to be revealed by the multi-focus window rendering image in Fig. 31 (f) comparing to skull remained-image in Fig. 31(e). In addition, the experimental mode with the skull left intact is non-invasive, thus that it is more suitable for longitudinal time course study of brain.

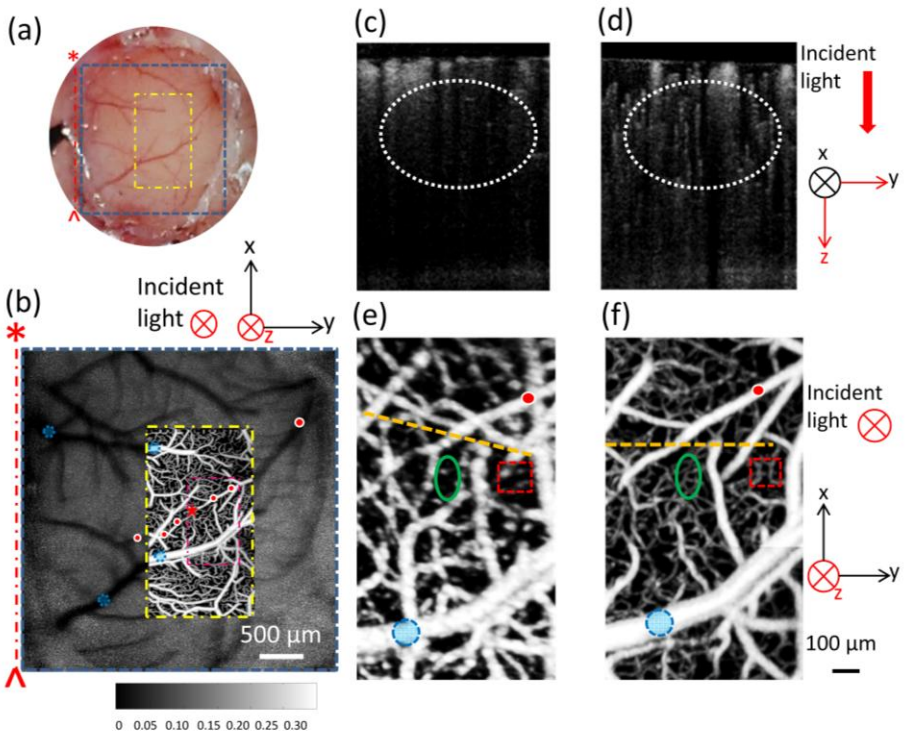

Figure 31 Comparisons of cranial window rending images with the skull left intact rending images. (a) Conventional microscopy through the cranial window with the imaging range marked by the dashed square (LSCI) and dash-dot rectangle (OMAG). The dot-dash line indicates the midline; the anterior side is indicated by an asterisk; the posterior side is indicated by a triangle. (b) OMAG image superposed onto the LSCI image. Speckle contrast image is marked by the blue dashed square. The OMAG image is marked by the outer dash-dotted rectangle. The inner dash-dotted rectangle notes the imaging area in (e) and (f). The scale bar is 500 µm. The color bar denotes speckle contrast. In (a) and (b), the dot-dash line indicates the midline; the anterior side is indicated by an asterisk; the posterior side is indicated by a triangle. The red solid spots mark the arteries; dotted circles mark the veins. The red star denotes the anastomosis. The color bar denotes speckle contrast. (c) and (d) are respectively cross-section images with skull and cranial window. The positions of (c) and (d) are indicated by the dashed lines in (e) and (f), respectively. The dotted ovals in (b) and (c) circled the regions that are under comparison. (e) and (f) are respectively the projection views of 75 µm thickness from the surface of mouse brain. Still, the blue dotted circle mark the vein, and the red solid spots note the artery. The ovals and rectangles presents regions with (f) or without (e) capillary loops. The scale bar in (c)-(f) is 100 µm.

Figure 32 shows a wide field of view of the intact cranial window. It is a representative wide-field mosaic projection view of macro and micro- circulations within 50 µm beneath the cortex surface. The rich cortical blood flow can be clearly identified, providing volumetric measurements of detailed microcirculation through the vascular tree down to

capillary level. In Fig. 32(a), the upstreams of middle cerebral artery (MCA) and anterior cerebral artery (ACA) are denoted by the double circles and star, respectively. There is remarkable spatial arrangement of the blood vessels supplying the barrels in somatosensory cortex. The MCA arises from the internal carotid and continues into the lateral sulcus where it then diminishes in size, branches in the anterior-posterior direction and projects to different parts of the lateral cerebral cortex (marked by solid line circle), running across the surface of the cortex to supply the barrels. ACA diminishes in size and spreads to several branches and projects to an area on the neocortex (marked by solid spots).

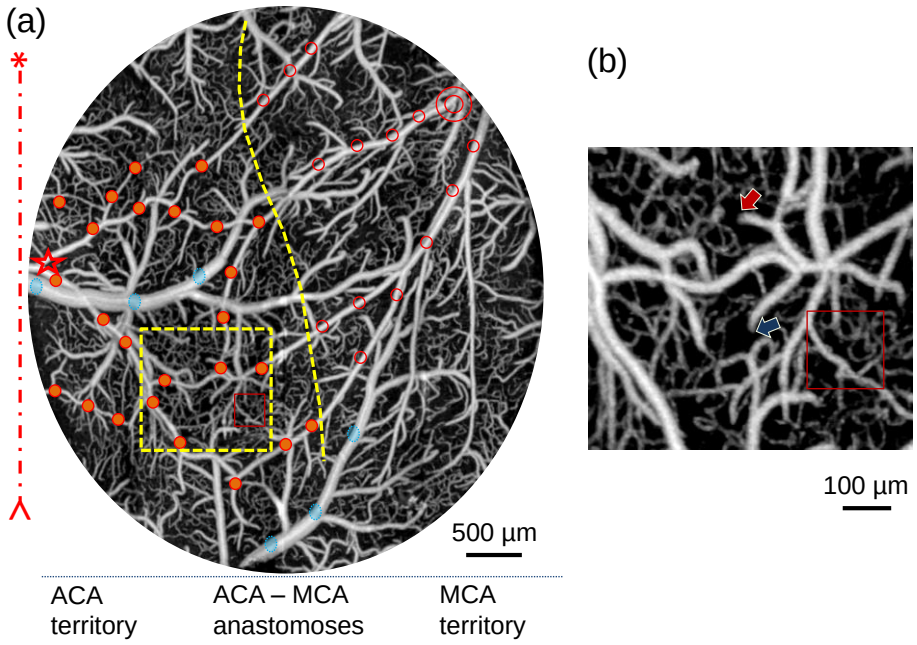

Figure 32 Wide field of view (cranial window diameter: 4.2 mm) of the functional blood flow within 0-50 µm from the cortex surface. (a) Star denotes ACA and its branches; double circles denote MCA and its branches. Solid line circle denotes MCA branched arteries and arterioles; solid dots mark ACA branched arteries and arterioles; dotted circles mark veins; dashed line indicates anastomosis. The dot-dash line indicates the midline, where the superior sagittal sinus locates in; the anterior side and the posterior side are indicated by an asterisk and a triangle, respectively. (b) The magnification of the region marked by yellow dashed square in (a). The arrows point to typical diving vessels. The red square denotes the region of interest.

More importantly, OMAG is capable of visualizing the rich anastomoses between the peripheral branches of the ACA and MCA (the dashed line in (a)). Veins (marked by blue dotted circles) on the cortical surface drain the large area medially into the

superior sagittal sinus. Our projection view image encompassed all those afore mentioned functional vasculatures. The points of anastomoses between the peripheral branches of the ACA and MCA are marked by the dashed line. Because of its capability of imaging extremely slow blood flow, it is not surprising that OMAG could give images with great capillary density in the cortex (see square region). Furthermore, capillaries are more tortuous than the large vessel. In Fig. 32(b), it is noticeable that there are no capillaries surrounding the diving vessels (pointed by the arrows). It is due to the characteristic and behavior of the penetrating vessels, which dive down into the deep brain tissue. They first branch into intracerebral arterioles, which later eventually branch into capillaries where exchange between the blood and the tissues of oxygen, nutrients, carbon dioxide, and metabolites occur. The characteristic of diving vessels cannot be visualized from laser speckle image [Fig. 31(b)].

5.2.4 Summarization and discussion

In conclusion, we have demonstrated multi-focal-plane imaging of vascular network in the highly scattering cortical tissue in vivo down to capillary level with intrinsic contrast. Through the use of image-guided OMAG with dynamic focusing and high-resolution image processing techniques, we demonstrated imaging of both angiography and blood flow velocity. The concept of depth enhanced multi-parametric microvasculature imaging with intrinsic contrast has potential applications in longitudinal studies of development, disease progression, and treatment response. It can contribute to the investigation of layer-to-layer microvasculature functions down to cellular resolution. In the future, we will optimize the system to achieve a ~2 μm resolution for capillary visualization. With the high imaging resolution, it is possible to directly monitor a single blood cell transporting within the capillaries in different layers of the brain. Using a repeated B-scan scanning pattern, the process of a blood cell passing through the scanning cross section can be recorded. The light backscattered from the single blood cell could be detected as a bright spot in the UHS-OMAG flow image. If it is recorded over time, the appearance of blood cells would be demonstrated as an intensity peak. The peak width can present the time that a single blood cell passes through the imaging beam while the peak number is the red blood cell flux of the capillaries. With the proposed method, it is possible to accurately measure the hemodynamic properties of capillaries in individual layer of the brain and other organs, which will help us to achieve better understanding of the mechanisms by which microcirculation contributes to neurovascular diseases.

Publications

Journals:

1. **Jia Qin***, Lei Shi*, Ruikang Wang, "Depth Enhanced Cerebral Blood Flow Imaging", ***Optics letters*** (in preparation)
2. Lei Shi*, **Jia Qin***, Lin An, Ruikang Wang, "Flexibly combined optical microangiography and dual-wavelength laser speckle system for comprehensive imaging of hemodynamic and metabolic responses", ***Optics letters*** (in preparation)
3. Suzan Dziennis*, **Jia Qin***, Lei Shi*, Ruikang Wang, "*A multifunctional optical imager for monitoring the hemodynamic response in ischemic stroke",* ***Journal of Cerebral Blood Flow & Metabolism.*** (in preparation)
4. Michael C. Chappell, Sivash Yousefi, **Jia Qin**, Ruikang Wang, Shu-Hong Chang, "*In Vivo* Imaging of a Novel Mouse Model of Filler-Induced Tissue Necrosis" (in preparation).
5. **Jia Qin**, Lei Shi, Hequn Wang, Ruikang Wang, "Functional evaluation of hemodynamic and metabolic variations in neural activation using a multifunctional optical imaging system based on dual-wavelength laser speckle imaging and optical microangiography", ***Journal of biomedical optics letter***s, 19(2), 026013, 2014.
6. Siavash Yousefi, **Jia Qin**, Ruikang K Wang, "Super-resolution spectral estimation of optical micro-angiography for quantifying blood flow within microcirculatory tissue beds *in vivo*", ***Biomedical optics express***, 4(7), 1214-1228, 2013.
7. Lei Shi, **Jia Qin**, Ruikang Wang, Wide velocity range Doppler optical microangiography using optimized step-scanning protocol with phase-variance mask, ***Journal of biomedical optics***, 18(10), 106015, 2013.
8. Rong Liu, **Jia Qin**, Ruikang K. Wang, "Motion-contrast laser speckle imaging of microcirculation

within tissue beds in Vivo”, ***Journal of biomedical optics letter***, 18(6), 060508-060508, 2013.

9. Siavash Yousefi, **Jia Qin**, Zhongwei Zhi, Ruikang K Wang, “Label-free optical lymphangiography: development of an automatic segmentation method applied to optical coherence tomography to visualize lymphatic vessels using Hessian filters”, ***Journal of biomedical optics***, 18(8), 086004-086004, 2013.
10. Siavash Yousefi, **Jia Qin**, and Ruikang Wang, “Uniform Enhancement of Optical Micro-angiography Images using Rayleigh Contrast-Limited Adaptive Histogram Equalization”, ***Quantitative imaging in medicine and surgery***, 3(1), 5, 2013.
11. Roberto Reif *, **Jia Qin ***, Lei Shi *, Suzan Dziennis, Zhongwei Zhi, Alfred Nuttall and Ruikang K. Wang, “Monitoring hypoxia induced changes in cochlear blood flow and haemoglobin concentration using a combined dual-wavelength laser speckle contrast imaging and Doppler optical microangiography system”, ***PLoS One***, 7 (12), e52041, 2012.
12. Roberto Reif*, **Jia Qin***, Lin An, Zhongwei Zhi, Suzan Dziennis and Ruikang Wang. “Quantifying optical microangiography images obtained from a spectral domain optical coherence tomography system”, ***International Journal of Biomedical Imaging,*** 11, 509783, 2012.
13. **Jia Qin**, Lei Shi, Suzan Dziennis, Roberto Reif, and Ruikang K. Wang, “Fast synchronized dual-wavelength laser speckle imaging system for monitoring hemodynamic changes in a stroke mouse model”, ***Optics Letters***, 37 (19), 4005 – 4007, 2012.
14. **Jia Qin**, Roberto Reif, Lin An, Zhongwei Zhi, Suzan Dziennis, Ruikang Wang. Hemodynamic and morphological vasculature response to a burn using a dual-wavelength laser speckle imaging and ultrahigh sensitive optical microangiography system, ***Biomedical optics expre***ss, 3 (3), 455-466, 2011.
15. **Jia Qin**, Jingying Jiang, Lin An, Dan Gareau, Ruikang Wang, *In vivo* Volumetric Imaging of Microcirculation within Human Skin under Psoriatic Conditions using Optical Microangiography**,** ***Lasers in Surgery and Medicine***, 43(2), 122–129, 2011.
16. Yali Jia, **Jia Qin**, Zhongwei Zhi, and Ruikang Wang, “Ultra-high sensitive optical microangiography

reveals depth-resolved microcirculation and its longitudinal response to prolonged ischemic event within skeletal muscles in mice", ***Journal of Biomedical Optics***, 16(8), 086004-086004-6, 2011.

17. **Jia Qin*,** Zhongwei Zhi*, Lin An, and Ruikang K. Wang. Supercontinuum light source enables in vivo optical microangiography of capillary vessels within tissue beds. ***Optics letter***, 36(16), 3169-3171, 2011.
18. Lin An, **Jia Qin** and Ruikang Wang, "Ultrahigh sensitive optical microangiography for in vivo imaging of microcirculations within human skin tissue beds", ***Optics Express***, 18, 8220-8228, 2010.
19. **J Qin**, ZR Qiu, DF Lv, L An, YM Fan, GX Zhang, "Design and application of a laser confocal probe", ***Instrumentation Science and Technology*** 35 (3), 295-306, 2007.

Conferences:

1. **Jia Qin**, et al, "Large field of view and depth specific cortical microvascular imaging underlies regional differences in ischemic brain," for Invited Oral presentation, ***SPIE***, 2014 (invited)
2. **Jia Qin,** et al, "Multi parametric imaging of cerebral hemodynamic and metabolic response followed by ischemic injury," ***SPIE***, 2014.
3. Shu-Hong Chang, Michael C. Chappell, Sivash Yousefi, **Jin Qin,** Kristin Tarbet, Suzan Dziennis, Ruikang Wang, In Vivo Imaging of a Novel Mouse Model of Filler-Induced Tissue Necrosis, annual American Society of Ophthalmic Plastic & Reconstructive Surgery ***(ASOPRS***) fall scientific meeting, 2013.
4. **Jia Qin**, Lin An, Ruikang Wang, Functional evaluation of the fast and slow response in neural activation using a multi-modality optical imaging system, ***SPIE***, 2013
5. Lei Shi, **Jia Qin**, Ruikang Wang, Full-scale blood flow response in functional electrical stimulation in ouse model evaluated by variable range Doppler OCT, ***SPIE***, 2013
6. Lei Shi, Jia Qin, Suzan Dziennis, Ruikang K. Wang, Variable-range Doppler OCT using stabilized step scanning and phase variance binarized mask, ***SPIE***, 2013.
7. **Jia Qin**, Lin An, and Ruikang Wang. High-speed dynamic laser speckle imaging of changes of

microcirculation in vivo. ***Proc. SPIE***, 7898, 78980C, 2011;

8. **Jia Qin**, Lin An, Ruikang Wang, Ultra-high-sensitive optical micro-angiography provides depth resolved visualization of microcirculations within human skin under psoriatic conditions, ***SPIE BIOS***, 2011;
9. Lin An, **Jia Qin**, Zhongwei Zhi, et al, Ultra high resolution ultrahigh sensitive optical micro-angiography based on super continuum light source, ***SPIE***, 2011

Reference

1. T. H. Murphy and D. Corbett, "Plasticity during stroke recovery: from synapse to behaviour," *Nature reviews. Neuroscience* 10(12), 861-872 (2009)

2. F. Calamante, D. L. Thomas, G. S. Pell, J. Wiersma and R. Turner, "Measuring cerebral blood flow using magnetic resonance imaging techniques," *J Cereb Blood Flow Metab* 19(7), 701-735 (1999)

3. J. J. Bergan, L. Pascarella and G. W. S. Schonbein, "Microcirculation and venous ulcers: A review," *Ann Vasc Surg* 19(6), 921-927 (2005)

4. D. L. Crandall, G. J. Hausman and J. G. Kral, "A review of the microcirculation of adipose tissue: Anatomic, metabolic and angiogenic perspectives," *Microcirculation-Lon* 4(2), 211-232 (1997)

5. V. Srinivasan, S. Sakadzic, I. Gorczynska, A. Yaseen, J. Fujimoto and D. Boas, "Depth-resolved microscopy of cerebral blood flow and volume during somatosensory stimulation with doppler optical coherence tomography," *J Cerebr Blood F Met* 29(S111-S112 (2009)

6. A. Assoc, "Alzheimer's Association Report 2011 Alzheimer's disease facts and figures," *Alzheimers Dement* 7(2), 208-244 (2011)

7. M. Ferrari, T. Binzoni and V. Quaresima, "Oxidative metabolism in muscle," *Philos T Roy Soc B* 352(1354), 677-683 (1997)

8. V. Provitera, M. Nolano, N. Pappone, E. Lubrano, B. Lanzillo and L. Santoro, "Axonal degeneration in systemic sclerosis can be reverted by factors improving tissue oxygenation," *J Peripher Nerv Syst* 11(2), 202-202 (2006)

9. S. R. Nirmala, S. Dandapat and P. M. Bora, "Wavelet weighted blood vessel distortion measure for retinal images," *Biomed Signal Proces* 5(4), 282-291 (2010)

10. G. Ciuffetti, L. Pasqualini, M. Pirro, R. Lombardini, M. De Sio, G. Schillaci and E. Mannarino, "Blood rheology in men with essential hypertension and capillary rarefaction," *Journal of Human Hypertension* 16(8), 533-537 (2002)

11. P. M. Hutchins, V. L. Roddick and J. W. Dusseau, "Correlation of Blood-Pressure and Rarefaction of Small Arterioles in Back-Crossed Spontaneously Hypertensive Rats," *Microvasc Res* 21(2), 246-246 (1981)

12. J. P. Noon, B. R. Walker, D. J. Webb, A. C. Shore, D. W. Holton, H. V. Edwards and G. C. M. Watt, "Impaired microvascular dilatation and capillary rarefaction in young adults with a predisposition to high blood pressure," *J Clin Invest* 99(8), 1873-1879 (1997)

13. P. Horstmann, "The Oxygen Consumption in Diabetes Mellitus," *Acta Med Scand* 139(4), 326-330 (1951)

14. F. S. Sutherland, E. Stefansson, D. L. Hatchell and H. Reiser, "Retinal Oxygen-Consumption Invitro the Effect of Diabetes-Mellitus, Oxygen and Glucose," *Acta Ophthalmol* 68(6), 715-720 (1990)

15. E. Tibirica, E. Rodrigues, R. A. Cobas and M. B. Gomes, "Endothelial function in patients with type 1 diabetes evaluated by skin capillary recruitment," *Microvasc Res* 73(2), 107-112 (2007)

16. A. Shmonin, E. Melnikova, M. Galagudza and T. Vlasov, "Characteristics of cerebral ischemia in major rat stroke models of middle cerebral artery ligation through craniectomy," *Int J Stroke* (2012)

17. N. S. Basheer, E. H. Roland, S. Miller, K. Poskitt, M. Sargent and A. Hill, "The role of hypoxia-ischemia in term newborns with arterial stroke," *Annals of Neurology* 62(S130-S130 (2007)

18. C. M. Wacker, A. W. Hartlep, M. Bock, S. Pfleger, G. Beck, G. van Kaick, L. R. Schad and W. R. Bauer, "BOLD-MRI of the heart in patients with coronary artery disease: Evidence for imaging of capillary recruitment in myocardium supplied by the stenotic artery," *Circulation* 98(17), 371-371 (1998)

19. R. Cooper, J. Cutler, P. Desvigne-Nickens, S. P. Fortmann, L. Friedman, R. Havlik, G. Hogelin, J. Marler, P. McGovern, G. Morosco, L. Mosca, T. Pearson, J. Stamler, D. Stryer and T. Thom, "Trends and disparities in coronary heart disease, stroke, and other cardiovascular diseases in the United States - Findings of the National Conference on Cardiovascular Disease Prevention," *Circulation* 102(25), 3137-3147 (2000)

20. G. Weinstein, A. S. Beiser, R. Au, C. Decarli, P. A. Wolf and S. Seshadri, "Association of Parental Stroke With Brain Injury and Cognitive Measures in Offspring: The Framingham Heart Study," *Stroke* (2013)

21. X. Fan, M. Ning, E. H. Lo and X. Wang, "Early insulin glycemic control combined with tPA thrombolysis reduces acute brain tissue damages in a focal embolic stroke model of diabetic rats," *Stroke* 44(1), 255-259 (2013)

22. D. I. Hoult, S. J. Busby, D. G. Gadian, G. K. Radda, R. E. Richards and P. J. Seeley, "Observation of tissue metabolites using 31P nuclear magnetic resonance," *Nature* 252(5481), 285-287 (1974)

23. T. Krucker, A. Schuler, E. P. Meyer, M. Staufenbiel and N. Beckmann, "Magnetic resonance angiography and vascular corrosion casting as tools in biomedical research: application to transgenic mice modeling Alzheimer's disease," *Neurol Res* 26(5), 507-516 (2004)

24. W. H. Xu, M. L. Li, S. Gao, J. Ni, L. X. Zhou, M. Yao, B. Peng, J. M. Wang and L. Y. Cui, "Middle Cerebral Artery Plaque in Patients with A Single Infarct in the Territory of Deep Penetrating Arteries: a High-resolution MRI Study," *Stroke* 42(3), E125-E125 (2011)

25. K. Cheng, "Recent progress in high-resolution functional MRI," *Curr Opin Neurol* 24(4), 401-408 (2011)

26. K. C. Mazzetto-Betti, O. M. Pontes-Neto, R. F. Leoni, A. D. Santos, A. C. Silva, J. P. Leite and D. B. Araujo, "BOLD Response Stability is Altered Patients With Chronic Ischemic Stroke," *Stroke* 41(4), E370-E370 (2010)

27. S. G. Kim, A. C. Silva, S. P. Lee, G. Yang and C. Iadecola, "Simultaneous blood oxygenation level-dependent and cerebral blood flow functional magnetic resonance imaging during forepaw stimulation in the rat," *J Cerebr Blood F Met* 19(8), 871-879 (1999)

28. K. Sako, A. Kato, K. Kobatake, M. Diksic, L. Yamamoto and Y. Yonemasu, "[Quantitative double tracer autoradiographic technique for the simultaneous measurement of local cerebral blood flow and local cerebral glucose utilization using 14C-IAP and 18F-FDG]," *No To Shinkei* 36(7), 649-656 (1984)

29. S. J. Colloby, J. P. Taylor, C. M. Davison, J. J. Lloyd, M. J. Firbank, I. G. McKeith and J. T. O'Brien, "Multivariate spatial covariance analysis of (99m)Tc-exametazime SPECT images in dementia with Lewy bodies and Alzheimer's disease: utility in differential diagnosis," *J Cereb Blood Flow Metab* (2013)

30. J. E. Assentoft, J. S. Thomsen and A. Andreasen, "Supersampling in PET. A concept for improvement of the resolution of positron emission tomography," *Conf Proc IEEE Eng Med Biol Soc* 2010(3622-3625 (2010)

31. J. R. Davies, J. H. Rudd, T. D. Fryer, M. J. Graves, J. C. Clark, P. J. Kirkpatrick, J. H. Gillard, E. A. Warburton and P. L. Weissberg, "Identification of culprit lesions after transient ischemic attack by combined 18F fluorodeoxyglucose positron-emission tomography and high-resolution magnetic resonance imaging," *Stroke* 36(12), 2642-2647 (2005)

32. M. Folin, S. Baiguera, M. Gallucci, M. Conconi, R. Liddo, A. Zanardo and P. Parnigotto, "A cross-sectional study of homocysteine-, NO-levels, and CT-findings in Alzheimer dementia, vascular dementia and controls," *Biogerontology* 6(4), 255-260 (2005)

33. E. M. C. Hillman, "Optical brain imaging in vivo: techniques and applications from animal to man," *Journal of Biomedical Optics* 12(5), (2007)

34. C. Longo, A. Casari, B. De Pace, S. Simonazzi, G. Mazzaglia and G. Pellacani, "Proposal for an in vivo histopathologic scoring system for skin aging by means of confocal microscopy," *Skin Res Technol* 19(1), E167-E173 (2013)

35. L. Belayev, E. Pinard, H. Nallet, J. Seylaz, Y. T. Liu, W. H. Zhao, R. Busto and M. D. Ginsberg, "In vivo microvascular analysis of albumin therapy in focal cerebral ischemia: Dynamic laser confocal microscopy.," *Stroke* 32(1), 350-351 (2001)

36. J. Lecoq, A. Parpaleix, E. Roussakis, M. Ducros, Y. G. Houssen, S. A. Vinogradov and S. Charpak, "Simultaneous two-photon imaging of oxygen and blood flow in deep cerebral vessels," *Nat Med* 17(7), 893-U262 (2011)

37. T. Hashimoto, H. Ohata and K. Honda, "Determination of calcium and contractile responses of rat cerebral artery employing real-time confocal laser microscopy.," *J Pharmacol Sci* 103(73p-73p (2007)

38. L. H. V. Wang, H. F. Zhang, K. Maslov and G. Stoica, "Functional photoacoustic microscopy for high-resolution and noninvasive in vivo imaging," *Nat Biotechnol* 24(7), 848-851 (2006)

39. J. A. Eyre, T. J. H. Essex, P. A. Flecknell, P. H. Bartholomew and J. I. Sinclair, "A Comparison of Measurements of Cerebral Blood-Flow in the Rabbit Using Laser Doppler Spectroscopy and Radionuclide Labeled Microspheres," *Clin Phys Physiol M* 9(1), 65-74 (1988)

40. D. A. Boas and A. K. Dunn, "Laser speckle contrast imaging in biomedical optics," *Journal of Biomedical Optics* 15(1), (2010)

41. C. Ayata, A. K. Dunn, Y. Gursoy-Ozdemir, Z. H. Huang, D. A. Boas and M. A. Moskowitz, "Laser speckle flowmetry for the study of cerebrovascular physiology in normal and ischemic mouse cortex," *J Cerebr Blood F Met* 24(7), 744-755 (2004)

42. A. F. Fercher, "Velocity-Measurement by 1st Order-Statistics of Time-Differentiated Laser Speckles," *Opt Commun* 33(2), 129-135 (1980)

43. J. D. Briers, "Laser Doppler, speckle and related techniques for blood perfusion mapping and imaging," *Physiol Meas* 22(4), R35-R66 (2001)

44. A. K. Dunn, T. Bolay, M. A. Moskowitz and D. A. Boas, "Dynamic imaging of cerebral blood flow using laser speckle," *J Cerebr Blood F Met* 21(3), 195-201 (2001)

45. B. Weber, C. Burger, M. T. Wyss, G. K. von Schulthess, F. Scheffold and A. Buck, "Optical imaging of the spatiotemporal dynamics of cerebral blood flow and oxidative metabolism in the rat barrel cortex," *Eur J Neurosci* 20(10), 2664-2670 (2004)

46. D. A. Boas and A. K. Dunn, "Laser speckle contrast imaging in biomedical optics," *J Biomed Opt* 15(1), 011109 (2010)

47. R. Reif, O. A'Amar and I. J. Bigio, "Analytical model of light reflectance for extraction of the optical properties in small volumes of turbid media," *Appl Optics* 46(29), 7317-7328 (2007)

48. A. K. Dunn, A. Devor, H. Bolay, M. L. Andermann, M. A. Moskowitz, A. M. Dale and D. A. Boas, "Simultaneous imaging of total cerebral hemoglobin concentration, oxygenation, and blood flow during functional activation," *Optics Letters* 28(1), 28-30 (2003)

49. J. Qin, J. Y. Jiang, L. An, D. Gareau and R. K. Wang, "In Vivo Volumetric Imaging of Microcirculation Within Human Skin Under Psoriatic Conditions Using Optical Microangiography," *Laser Surg Med* 43(2), 122-129 (2011)

50. Z. C. Luo, Z. J. Yuan, Y. T. Pan and C. W. Du, "Simultaneous imaging of cortical hemodynamics and blood oxygenation change during cerebral ischemia using dual-wavelength laser speckle contrast imaging," *Optics letters* 34(9), 1480-1482 (2009)

51. Z. J. Yuan, Z. C. Luo, N. D. Volkow, Y. T. Pan and C. W. Du, "Imaging separation of neuronal from vascular effects of cocaine on rat cortical brain in vivo," *Neuroimage* 54(2), 1130-1139 (2011)

52. M. B. Bouchard, B. R. Chen, S. A. Burgess and E. M. C. Hillman, "Ultra-fast multispectral optical imaging of cortical oxygenation, blood flow, and intracellular calcium dynamics," *Optics Express* 17(18), 15670-15678 (2009)

53. M. Wolf, U. Wolf, J. H. Choi, V. Toronov, L. A. Paunescu, A. Michalos and E. Gratton, "Fast cerebral functional signal in the 100-ms range detected in the visual cortex by frequency-domain near-infrared spectrophotometry," *Psychophysiology* 40(4), 521-528 (2003)

54. V. Kalchenko, N. Madar-Balakirski, I. Meglinski and A. Harmelin, "In vivo characterization of tumor and tumor vascular network using multi-modal imaging approach," *J Biophotonics* 4(9), 645-649 (2011)

55. S. A. Carp, G. P. Dai, D. A. Boas, M. A. Franceschini and Y. R. Kim, "Validation of diffuse correlation spectroscopy measurements of rodent cerebral blood flow with simultaneous arterial spin labeling MRI; towards MRI-optical continuous cerebral metabolic monitoring," *Biomed Opt Express* 1(2), 553-565 (2010)

56. D. Huang, E. A. Swanson, C. P. Lin, J. S. Schuman, W. G. Stinson, W. Chang, M. R. Hee, T. Flotte, K. Gregory, C. A. Puliafito and et al., "Optical coherence tomography," *Science* 254(5035), 1178-1181 (1991)

57. S. A. Boppart, B. E. Bouma, C. Pitris, J. F. Southern, M. E. Brezinski and J. G. Fujimoto, "In vivo cellular optical coherence tomography imaging," *Nature medicine* 4(7), 861-865 (1998)

58. L. An and R. K. Wang, "Use of a scanner to modulate spatial interferograms for in vivo full-range Fourier-domain optical coherence tomography," *Optics letters* 32(23), 3423-3425 (2007)

59. J. D. Briers, "Laser Doppler, speckle and related techniques for blood perfusion mapping and imaging," *Physiological measurement* 22(4), R35-66 (2001)

60. J. D. Briers, "Laser Doppler, speckle and related techniques for blood perfusion mapping and imaging," *Physiol Meas* 22(4), R35-66 (2001)

61. J. D. Briers and S. Webster, "Laser speckle contrast analysis (LASCA): a nonscanning, full-field technique for monitoring capillary blood flow," *J Biomed Opt* 1(2), 174-179 (1996)

62. S. Yuan, A. Devor, D. A. Boas and A. K. Dunn, "Determination of optimal exposure time for imaging of blood flow changes with laser speckle contrast imaging," *Appl Opt* 44(10), 1823-1830 (2005)

63. G. Royl, C. Leithner, H. Sellien, J. P. Muller, D. Megow, N. Offenhauser, J. Steinbrink, M. Kohl-Bareis, U. Dirnagl and U. Lindauer, "Functional imaging with laser speckle contrast analysis: vascular compartment analysis and correlation with laser Doppler flowmetry and somatosensory evoked potentials," *Brain Res* 1121(1), 95-103 (2006)

64. B. Ruth, J. Schmand and D. Abendroth, "Noncontact determination of skin blood flow using the laser speckle method: application to patients with peripheral arterial occlusive disease (PAOD) and to type-I diabetics," *Lasers Surg Med* 13(2), 179-188 (1993)

65. A. K. Murray, R. E. Gorodkin, T. L. Moore, R. J. Gush, A. L. Herrick and T. A. King, "Comparison of red and green laser doppler imaging of blood flow," *Lasers in surgery and medicine* 35(3), 191-200 (2004)

66. H. Cheng, Q. Luo, Q. Liu, Q. Lu, H. Gong and S. Zeng, "Laser speckle imaging of blood flow in microcirculation," *Phys Med Biol* 49(7), 1347-1357 (2004)

67. C. Millet, M. Roustit, S. Blaise and J. L. Cracowski, "Comparison between laser speckle contrast imaging and laser Doppler imaging to assess skin blood flow in humans," *Microvasc Res* 82(2), 147-151 (2011)

68. A. Ponticorvo, D. Cardenas, A. K. Dunn, D. Ts'o and T. Q. Duong, "Laser speckle contrast imaging of blood flow in rat retinas using an endoscope," *J Biomed Opt* 18(9), 90501 (2013)

69. L. M. Richards, S. M. Kazmi, J. L. Davis, K. E. Olin and A. K. Dunn, "Low-cost laser speckle contrast imaging of blood flow using a webcam," *Biomedical optics express* 4(10), 2269-2283 (2013)

70. A. K. Dunn, H. Bolay, M. A. Moskowitz and D. A. Boas, "Dynamic imaging of cerebral blood flow using laser speckle," Journal of cerebral blood flow and metabolism : official journal of the International Society of Cerebral Blood Flow and Metabolism 21(3), 195-201 (2001)

71. Z. C. Luo, Z. J. Yuan, Y. T. Pan and C. W. Du, "Simultaneous imaging of cortical hemodynamics and blood oxygenation change during cerebral ischemia using dual-wavelength laser speckle contrast imaging," *Optics Letters* 34(9), 1480-1482 (2009)

72. A. K. Dunn, "Laser Speckle Contrast Imaging of Cerebral Blood Flow," *Annals of Biomedical Engineering* 40(2), 367-377 (2012)

73. M. H. Li, P. Miao, Y. S. Zhu and S. B. Tong, "Functional laser speckle imaging of cerebral blood flow under hypothermia," *Journal of Biomedical Optics* 16(8), (2011)

74. P. Zakharov, A. C. Volker, M. T. Wyss, F. Haiss, N. Calcinaghi, C. Zunzunegui, A. Buck, F. Scheffold and B. Weber, "Dynamic laser speckle imaging of cerebral blood flow," *Optics Express* 17(16), 13904-13917 (2009)

75. A. F. Fercher, "Optical coherence tomography - development, principles, applications," *Zeitschrift fur medizinische Physik* 20(4), 251-276 (2010)

76. J. G. Fujimoto, M. E. Brezinski, G. J. Tearney, S. A. Boppart, B. Bouma, M. R. Hee, J. F. Southern and E. A. Swanson, "Optical Biopsy and Imaging Using Optical Coherence Tomography," *Nat Med* 1(9), 970-972 (1995)

77. A. M. Sergeev, V. M. Gelikonov, G. V. Gelikonov, F. I. Feldchtein, R. V. Kuranov, N. D. Gladkova, N. M. Shakhova, L. B. Snopova, A. V. Shakhov, I. A. Kuznetzova, A. N. Denisenko, V. V. Pochinko, Y. P. Chumakov and O. S. Streltzova, "In vivo endoscopic OCT imaging of precancer and cancer states of human mucosa," *Optics Express* 1(13), 432-440 (1997)

78. W. Drexler, U. Morgner, F. X. Kartner, C. Pitris, S. A. Boppart, X. D. Li, E. P. Ippen and J. G. Fujimoto, "In vivo ultrahigh-resolution optical coherence tomography," *Optics Letters* 24(17), 1221-1223 (1999)

79. C. Pitris, A. Goodman, S. A. Boppart, J. J. Libus, J. G. Fujimoto and M. E. Brezinski, "High-resolution imaging of gynecologic neoplasms using optical coherence tomography," *Obstetrics and gynecology* 93(1), 135-139 (1999)

80. U. Morgner, W. Drexler, F. X. Kartner, X. D. Li, C. Pitris, E. P. Ippen and J. G. Fujimoto, "Spectroscopic optical coherence tomography," *Optics Letters* 25(2), 111-113 (2000)

81. J. Lee, W. Wu, J. Y. Jiang, B. Zhu and D. A. Boas, "Dynamic light scattering optical coherence tomography," *Opt Express* 20(20), 22262-22277 (2012)

82. Y. Zhao, Z. Chen, Z. Ding, H. Ren and J. S. Nelson, "Real-time phase-resolved functional optical coherence tomography by use of optical Hilbert transformation," *Optics letters* 27(2), 98-100 (2002)

83. V. J. Srinivasan, S. Sakadzic, I. Gorczynska, S. Ruvinskaya, W. Wu, J. G. Fujimoto and D. A. Boas, "Quantitative cerebral blood flow with optical coherence tomography," *Optics express* 18(3), 2477-2494 (2010)

84. R. K. Wang and Z. Ma, "Real-time flow imaging by removing texture pattern artifacts in spectral-domain optical Doppler tomography," *Optics letters* 31(20), 3001-3003 (2006)

85. Y. C. Huang, T. L. Ringold, J. S. Nelson and B. Choi, "Noninvasive blood flow imaging for real-time feedback during laser therapy of port wine stain birthmarks," *Laser Surg Med* 40(3), 167-173 (2008)

86. B. E. Bouma, S. H. Yun, B. J. Vakoc, M. J. Suter and G. J. Tearney, "Fourier-domain optical coherence tomography: recent advances toward clinical utility," *Current opinion in biotechnology* 20(1), 111-118 (2009)

87. K. Zhang and J. U. Kang, "Graphics processing unit accelerated non-uniform fast Fourier transform for ultrahigh-speed, real-time Fourier-domain OCT," *Opt Express* 18(22), 23472-23487 (2010)

88. R. K. Wang, S. L. Jacques, Z. Ma, S. Hurst, S. R. Hanson and A. Gruber, "Three dimensional optical angiography," *Optics express* 15(7), 4083-4097 (2007)

89. L. An, J. Qin and R. K. Wang, "Ultrahigh sensitive optical microangiography for in vivo imaging of microcirculations within human skin tissue beds," *Optics express* 18(8), 8220-8228 (2010)

90. R. K. Wang and S. Hurst, "Mapping of cerebro-vascular blood perfusion in mice with skin and skull intact by Optical Micro-AngioGraphy at 1.3 mum wavelength," *Optics express* 15(18), 11402-11412 (2007)

91. L. An, H. M. Subhush, D. J. Wilson and R. K. Wang, "High-resolution wide-field imaging of retinal and choroidal blood perfusion with optical microangiography," *Journal of biomedical optics* 15(2), 026011 (2010)

92. R. K. Wang, L. An, S. Saunders and D. J. Wilson, "Optical microangiography provides depth-resolved images of directional ocular blood perfusion in posterior eye segment," *Journal of biomedical optics* 15(2), 020502 (2010)

93. B. J. Vakoc, R. M. Lanning, J. A. Tyrrell, T. P. Padera, L. A. Bartlett, T. Stylianopoulos, L. L. Munn, G. J. Tearney, D. Fukumura, R. K. Jain and B. E. Bouma, "Three-dimensional microscopy of the tumor microenvironment in vivo using optical frequency domain imaging," *Nature medicine* 15(10), 1219-1223 (2009)

94. Z. Luo, Z. Yuan, Y. Pan and C. Du, "Simultaneous imaging of cortical hemodynamics and blood oxygenation change during cerebral ischemia using dual-wavelength laser speckle contrast imaging," *Optics letters* 34(9), 1480-1482 (2009)

95. A. K. Dunn, A. Devor, H. Bolay, M. L. Andermann, M. A. Moskowitz, A. M. Dale and D. A. Boas, "Simultaneous imaging of total cerebral hemoglobin concentration, oxygenation, and blood flow during functional activation," *Optics letters* 28(1), 28-30 (2003)

96. J. Qin, R. Reif, Z. W. Zhi, S. Dziennis and R. K. Wang, "Hemodynamic and morphological vasculature response to a burn monitored using a combined dual-wavelength laser speckle and optical microangiography imaging system," *Biomedical Optics Express* 3(3), 455-466 (2012)

97. J. L. Martin and S. Roy, "Chronic morphine regulation on tissue remodeling and angiogenesis following wound injury and infection," *J Immunol* 176(S41-S41 (2006)

98. M. Kosieradzki, J. Pratschke, J. Kupiec-Weglinski and W. Rowinski, "Ischemia/Reperfusion injury, its mechanisms, and prevention," *J Transplant* 2012(610370 (2012)

99. A. Forster, K. Szabo and M. G. Hennerici, "Pathophysiological concepts of stroke in hemodynamic risk zones--do hypoperfusion and embolism interact?," *Nature clinical practice. Neurology* 4(4), 216-225 (2008)

100. S. Schreiber, M. Serdaroglu, F. Schreiber, M. Skalej, H. J. Heinze and M. Goertler, "Simultaneous occurrence and interaction of hypoperfusion and embolism in a patient with severe middle cerebral artery stenosis," *Stroke* 40(7), e478-480 (2009)

101. J. Qin, R. Reif, Z. Zhi, S. Dziennis and R. Wang, "Hemodynamic and morphological vasculature response to a burn monitored using a combined dual-wavelength laser speckle and optical microangiography imaging system," *Biomed Opt Express* 3(3), 455-466 (2012)

102. C. W. Du, Z. C. Luo, Z. J. Yuan and Y. T. Pan, "Simultaneous imaging of cortical hemodynamics and blood oxygenation change during cerebral ischemia using dual-wavelength laser speckle contrast imaging," *Opt Lett* 34(9), 1480-1482 (2009)

103. S. J. Kirkpatrick, D. D. Duncan and E. M. Wells-Gray, "Detrimental effects of speckle-pixel size matching in laser speckle contrast imaging," *Opt Lett* 33(24), 2886-2888 (2008)

104. S. J. Kirkpatrick, D. D. Duncan and E. M. Wells-Gray, "Detrimental effects of speckle-pixel size matching in laser speckle contrast imaging," *Opt Lett* 33(24), 2886-2888 (2008)

105. S. Yuan, A. Devor, D. A. Boas and A. K. Dunn, "Determination of optimal exposure time for imaging of blood flow changes with laser speckle contrast imaging," *Appl Optics* 44(10), 1823-1830 (2005)

106. H. Cheng, Q. Luo, S. Zeng, S. Chen, J. Cen and H. Gong, "Modified laser speckle imaging method with improved spatial resolution," *J Biomed Opt* 8(3), 559-564 (2003)

107. R. Liu, J. Qin and R. K. Wang, "Motion-contrast laser speckle imaging of microcirculation within tissue beds in vivo," *J Biomed Opt* 18(6), 060508 (2013)

108. B. Commoner and D. Lipkin, "The Application of the Beer-Lambert Law to Optically Anisotropic Systems," *Science* 110(2845), 41-43 (1949)

109. L. Kocsis, P. Herman and A. Eke, "The modified Beer-Lambert law revisited," *Phys Med Biol* 51(5), N91-98 (2006)

110. C. W. Du, A. P. Koretsky, I. Izrailtyan and H. Benveniste, "Simultaneous detection of blood volume, oxygenation, and intracellular calcium changes during cerebral ischemia and reperfusion in vivo using diffuse reflectance and fluorescence," *J Cerebr Blood F Met* 25(8), 1078-1092 (2005)

111. T. Kusaka, Y. Hisamatsu, K. Kawada, K. Okubo, H. Okada, M. Namba, T. Imai, K. Isobe and S. Itoh, "Measurement of cerebral optical pathlength as a function of oxygenation using near-infrared time-resolved spectroscopy in a piglet model of hypoxia," *Opt Rev* 10(5), 466-469 (2003)

112. M. Kohl, U. Lindauer, G. Royl, M. Kuhl, L. Gold, A. Villringer and U. Dirnagl, "Physical model for the spectroscopic analysis of cortical intrinsic optical signals," *Phys Med Biol* 45(12), 3749-3764 (2000)

113. Z. W. Zhi, W. Cepurna, E. Johnson, T. Shen, J. Morrison and R. K. K. Wang, "Volumetric and quantitative imaging of retinal blood flow in rats with optical microangiography," *Biomedical Optics Express* 2(3), 579-591 (2011)

114. L. An and R. K. Wang, "In vivo volumetric imaging of vascular perfusion within human retina and choroids with optical micro-angiography," *Opt Express* 16(15), 11438-11452 (2008)

115. L. An, J. Qin and R. K. Wang, "Ultrahigh sensitive optical microangiography for in vivo imaging of microcirculations within human skin tissue beds," *Optics Express* 18(8), 8220-8228 (2010)

116. J. Qin, J. Jiang, L. An, D. Gareau and R. K. Wang, "In vivo volumetric imaging of microcirculation within human skin under psoriatic conditions using optical microangiography," *Lasers Surg Med* 43(2), 122-129 (2011)

117. R. G. Jobling, "Psoriasis -- a preliminary questionnaire study of sufferers' subjective experience," *Clinical and experimental dermatology* 1(3), 233-236 (1976)

118. J. N. Barker, "The pathophysiology of psoriasis," *Lancet* 338(8761), 227-230 (1991)

119. R. De Angelis, L. Bugatti, P. Del Medico, M. Nicolini and G. Filosa, "Videocapillaroscopic findings in the microcirculation of the psoriatic plaque," *Dermatology* 204(3), 236-239 (2002)

120. Z. A. Awan, T. Wester and K. Kvernebo, "Human microvascular imaging: a review of skin and tongue videomicroscopy techniques and analysing variables," *Clinical physiology and functional imaging* 30(2), 79-88 (2010)

121. M. C. Pierce, J. Strasswimmer, B. H. Park, B. Cense and J. F. de Boer, "Advances in optical coherence tomography imaging for dermatology," *The Journal of investigative dermatology* 123(3), 458-463 (2004)

122. B. B. Davidovici, N. Sattar, J. Prinz, L. Puig, P. Emery, J. N. Barker, P. van de Kerkhof, M. Stahle, F. O. Nestle, G. Girolomoni and J. G. Krueger, "Psoriasis and systemic inflammatory diseases: potential mechanistic links between skin disease and co-morbid conditions," *J Invest Dermatol* 130(7), 1785-1796 (2010)

123. C. Prost-Squarcioni, "[Histology of skin and hair follicle]," *Med Sci (Paris)* 22(2), 131-137 (2006)

124. I. Garcia-Valladares and L. R. Espinoza, "Psoriasis pathophysiology," *Immunotherapy* 2(4), 444-445 (2010)

125. Z. Zhi, J. Qin, L. An and R. K. Wang, "Supercontinuum light source enables in vivo optical microangiography of capillary vessels within tissue beds," *Opt Lett* 36(16), 3169-3171 (2011)

126. J. P. Noon, B. R. Walker, D. J. Webb, A. C. Shore, D. W. Holton, H. V. Edwards and G. C. Watt, "Impaired microvascular dilatation and capillary rarefaction in young adults with a predisposition to high blood pressure," *The Journal of clinical investigation* 99(8), 1873-1879 (1997)

127. C. M. Wacker, M. Bock, A. W. Hartlep, W. R. Bauer, G. van Kaick, S. Pfleger, G. Ertl and L. R. Schad, "BOLD-MRI in ten patients with coronary artery disease: evidence for imaging of capillary recruitment in myocardium supplied by the stenotic artery," *Magma* 8(1), 48-54 (1999)

128. W. W. Wagner, Jr., L. P. Latham and R. L. Capen, "Capillary recruitment during airway hypoxia: role of pulmonary artery pressure," *Journal of applied physiology: respiratory, environmental and exercise physiology* 47(2), 383-387 (1979)

129. P. Horstmann, "The oxygen consumption in diabetes mellitus," *Acta medica Scandinavica* 139(4), 326-330 (1951)

130. E. Tibirica, E. Rodrigues, R. A. Cobas and M. B. Gomes, "Endothelial function in patients with type 1 diabetes evaluated by skin capillary recruitment," *Microvascular research* 73(2), 107-112 (2007)

131. R. K. Wang, "Three-dimensional optical micro-angiography maps directional blood perfusion deep within microcirculation tissue beds in vivo," *Physics in medicine and biology* 52(23), N531-537 (2007)

132. M. Wojtkowski, V. Srinivasan, T. Ko, J. Fujimoto, A. Kowalczyk and J. Duker, "Ultrahigh-resolution, high-speed, Fourier domain optical coherence tomography and methods for dispersion compensation," *Optics express* 12(11), 2404-2422 (2004)

133. A. C. Sull, L. N. Vuong, L. L. Price, V. J. Srinivasan, I. Gorczynska, J. G. Fujimoto, J. S. Schuman and J. S. Duker, "Comparison of spectral/Fourier domain optical coherence tomography instruments for assessment of normal macular thickness," *Retina* 30(2), 235-245 (2010)

134. S. Wray, M. Cope, D. T. Delpy, J. S. Wyatt and E. O. Reynolds, "Characterization of the near infrared absorption spectra of cytochrome aa3 and haemoglobin for the non-invasive monitoring of cerebral oxygenation," *Biochimica et biophysica acta* 933(1), 184-192 (1988)

135. S. J. Kirkpatrick, D. D. Duncan and E. M. Wells-Gray, "Detrimental effects of speckle-pixel size matching in laser speckle contrast imaging," *Opt Lett* 33(24), 2886-2888 (2008)

136. J. A. Eyre, T. J. Essex, P. A. Flecknell, P. H. Bartholomew and J. I. Sinclair, "A comparison of measurements of cerebral blood flow in the rabbit using laser Doppler spectroscopy and radionuclide labelled microspheres," *Clinical physics and physiological measurement : an official journal of the Hospital Physicists' Association, Deutsche Gesellschaft fur Medizinische Physik and the European Federation of Organisations for Medical Physics* 9(1), 65-74 (1988)

137. M. E. Seaman, S. M. Peirce and K. Kelly, "Rapid analysis of vessel elements (RAVE): a tool for studying physiologic, pathologic and tumor angiogenesis," *PloS one* 6(6), e20807 (2011)

138. H. F. Zhang, K. Maslov, G. Stoica and L. H. V. Wang, "Imaging acute thermal burns by photoacoustic microscopy," *J Biomed Opt* 11(5), (2006)

139. H. Schulte, A. Sollevi and M. Segerdahl, "The distribution of hyperaemia induced by skin burn injury is not correlated with the development of secondary punctate hyperalgesia," *J Pain* 5(4), 212-217 (2004)

140. A. H. Mulder, A. P. J. Van Dijk, P. Smits and C. J. Tack, "Real-time contrast imaging: A new method to monitor capillary recruitment in human forearm skeletal muscle," *Microcirculation* 15(3), 203-213 (2008)

141. K. Parthasarathi and H. H. Lipowsky, "Capillary recruitment in response to tissue hypoxia and its dependence on red blood cell deformability," *Am J Physiol-Heart C* 277(6), H2145-H2157 (1999)

142. M. E. Seaman, S. M. Peirce and K. Kelly, "Rapid Analysis of Vessel Elements (RAVE): A Tool for Studying Physiologic, Pathologic and Tumor Angiogenesis," *Plos One* 6(6), (2011)

143. R. Reif, J. Qin, L. An, Z. Zhi, S. Dziennis and R. Wang, "Quantifying optical microangiography images obtained from a spectral domain optical coherence tomography system," *International journal of biomedical imaging* 2012(509783 (2012)

144. B. R. Masters, "Fractal analysis of the vascular tree in the human retina," *Annu Rev Biomed Eng* 6(427-452 (2004)

145. V. Guarino, A. Guaccio, P. A. Netti and L. Ambrosio, "Image processing and fractal box counting: user-assisted method for multi-scale porous scaffold characterization," *J Mater Sci-Mater M* 21(12), 3109-3118 (2010)

146. J. W. Baish, T. Stylianopoulos, R. M. Lanning, W. S. Kamoun, D. Fukumura, L. L. Munn and R. K. Jain, "Scaling rules for diffusive drug delivery in tumor and normal tissues," *P Natl Acad Sci USA* 108(5), 1799-1803 (2011)

147. J. Qin, L. Shi, S. Dziennis, R. Reif and R. K. Wang, "Fast synchronized dual-wavelength laser speckle imaging system for monitoring hemodynamic changes in a stroke mouse model," *Optics letters* 37(19), 4005-4007 (2012)

148. C. Ayata, A. K. Dunn, O. Y. Gursoy, Z. Huang, D. A. Boas and M. A. Moskowitz, "Laser speckle flowmetry for the study of cerebrovascular physiology in normal and ischemic mouse cortex," *J Cereb Blood Flow Metab* 24(7), 744-755 (2004)

149. A. Kleinschmidt, H. Obrig, M. Requardt, K. D. Merboldt, U. Dirnagl, A. Villringer and J. Frahm, "Simultaneous recording of cerebral blood oxygenation changes during human brain activation by magnetic resonance imaging and near-infrared spectroscopy," *J Cereb Blood Flow Metab* 16(5), 817-826 (1996)

150. J. Axelsson, A. K. Glaser, D. J. Gladstone and B. W. Pogue, "Quantitative Cherenkov emission spectroscopy for tissue oxygenation assessment," *Opt Express* 20(5), 5133-5142 (2012)

151. H. Ren, C. Du, Z. Yuan, K. Park, N. D. Volkow and Y. Pan, "Cocaine-induced cortical microischemia in the rodent brain: clinical implications," *Molecular psychiatry* 17(10), 1017-1025 (2012)

152. M. B. Bouchard, B. R. Chen, S. A. Burgess and E. M. Hillman, "Ultra-fast multispectral optical imaging of cortical oxygenation, blood flow, and intracellular calcium dynamics," *Opt Express* 17(18), 15670-15678 (2009)

153. S. A. Carp, G. P. Dai, D. A. Boas, M. A. Franceschini and Y. R. Kim, "Validation of diffuse correlation spectroscopy measurements of rodent cerebral blood flow with simultaneous arterial spin labeling MRI; towards MRI-optical continuous cerebral metabolic monitoring," *Biomed Opt Express* 1(2), 553-565 (2010)

154. J. M. Lee, H. An, A. L. Ford, K. D. Vo, A. M. Nassief, C. P. Derdeyn, W. J. Powers and W. Lin, "Perfusion instability in the penumbra influences infarct probability in acute ischemic stroke patients," *J Cerebr Blood F Met* 29(S624-S625 (2009)

155. T. Y. Lee, B. D. Murphy, R. I. Aviv, A. J. Fox, S. E. Black, D. J. Sahlas, S. Symons, D. H. Lee, D. Pelz, I. B. Gulka, R. Chan, V. Beletsky, V. Hachinski, M. J. Hogan, M. Goyal, A. M. Demchuk and S. B. Coutts, "Cerebral blood flow threshold of ischemic penumbra and infarct core in acute ischemic stroke: A systematic review," *Stroke* 37(9), 2201-2201 (2006)

156. B. D. Murphy, A. J. Fox, D. H. Lee, D. J. Sahlas, S. E. Black, M. Hogan, S. B. Coutts, A. M. Demchuk, M. Goyal, R. I. Aviv, S. Symons, I. B. Gulka, V. Beletsky, D. Pelz, V. Hachinski, R. Chan and T. Y. Lee, "Identification of penumbra and infarct in acute ischemic stroke using computed tomography perfusion-derived blood flow and blood volume measurements," *Stroke* 37(7), 1771-1777 (2006)

157. R. Bandyopadhyay, A. S. Gittings, S. S. Suh, P. K. Dixon and D. J. Durian, "Speckle-visibility spectroscopy: A tool to study time-varying dynamics," *Rev Sci Instrum* 76(9), (2005)

158. P. B. Jones, H. K. Shin, D. A. Boas, B. T. Hyman, M. A. Moskowitz, C. Ayata and A. K. Dunn, "Simultaneous multispectral reflectance imaging and laser speckle flowmetry of cerebral blood flow and oxygen metabolism in focal cerebral ischemia," *J Biomed Opt* 13(4), 044007 (2008)

159. F. Hyder, "Neuroimaging with calibrated fMRI," *Stroke* 35(11), 2635-2641 (2004)

160. W. R. Zhang, I. P. Koerner, R. Noppens, M. Grafe, H. J. Tsai, C. Morisseau, A. Luria, B. D. Hammock, J. R. Falck and N. J. Alkayed, "Soluble epoxide hydrolase: a novel therapeutic target in stroke," *J Cerebr Blood F Met* 27(12), 1931-1940 (2007)

161. J. Krejza, J. Fryc, M. Owlasiuk, M. Huba, R. J. Bert and Z. Mariak, "Transcranial color Doppler sonography in the emergency diagnosis of middle cerebral artery occlusion in a patient after head injury," *Clinical imaging* 25(2), 90-94 (2001)

162. L. Shi, J. Qin, R. Reif and R. K. Wang, "Wide velocity range Doppler optical microangiography using optimized step-scanning protocol with phase variance mask," *J Biomed Opt* 18(10), 106015 (2013)

163. J. Qin, L. Shi, H. Wang, R. Reif and R. K. Wang, "Functional evaluation of hemodynamic response during neural activation using optical microangiography integrated with dual-wavelength laser speckle imaging," *J Biomed Opt* 19(2), 26013 (2014)

164. R. Reif, J. Qin, L. Shi, S. Dziennis, Z. Zhi, A. L. Nuttall and R. K. Wang, "Monitoring hypoxia induced changes in cochlear blood flow and hemoglobin concentration using a combined dual-wavelength laser speckle contrast imaging and Doppler optical microangiography system," *PloS one* 7(12), e52041 (2012)

165. A. K. Dunn, A. Devor, A. M. Dale and D. A. Boas, "Spatial extent of oxygen metabolism and hemodynamic changes during functional activation of the rat somatosensory cortex," *Neuroimage* 27(2), 279-290 (2005)

166. K. K. Kwong, J. W. Belliveau, D. A. Chesler, I. E. Goldberg, R. M. Weisskoff, B. P. Poncelet, D. N. Kennedy, B. E. Hoppel, M. S. Cohen, R. Turner and et al., "Dynamic magnetic resonance imaging of human brain activity during primary sensory stimulation," *Proc Natl Acad Sci U S A* 89(12), 5675-5679 (1992)

167. G. Bonvento, N. Cholet and J. Seylaz, "Sustained attenuation of the cerebrovascular response to a 10 min whisker stimulation following neuronal nitric oxide synthase inhibition," *Neurosci Res* 37(2), 163-166 (2000)

168. B. M. Ances, "Coupling of changes in cerebral blood flow with neural activity: What must initially dip must come back up," *J Cerebr Blood F Met* 24(1), 1-6 (2004)

169. E. Hamel, "Perivascular nerves and the regulation of cerebrovascular tone," *J Appl Physiol* 100(3), 1059-1064 (2006)

170. A. F. McCaslin, B. R. Chen, A. J. Radosevich, B. Cauli and E. M. Hillman, "In vivo 3D morphology of astrocyte-vasculature interactions in the somatosensory cortex: implications for neurovascular coupling," *J Cereb Blood Flow Metab* 31(3), 795-806 (2011)

171. H. Bolay, U. Reuter, A. K. Dunn, Z. Huang, D. A. Boas and M. A. Moskowitz, "Intrinsic brain activity triggers trigeminal meningeal afferents in a migraine model," *Nat Med* 8(2), 136-142 (2002)

172. S. Lloyd-Fox, A. Blasi and C. E. Elwell, "Illuminating the developing brain: the past, present and future of functional near infrared spectroscopy," *Neuroscience and biobehavioral reviews* 34(3), 269-284 (2010)

173. V. Kalchenko, Y. Kuznetsov, I. Meglinski and A. Harmelin, "Label free in vivo laser speckle imaging of blood and lymph vessels," *J Biomed Opt* 17(5), 050502 (2012)

174. Y. Jia, L. An and R. K. Wang, "Label-free and highly sensitive optical imaging of detailed microcirculation within meninges and cortex in mice with the cranium left intact," *Journal of biomedical optics* 15(3), 030510 (2010)

175. L. An, T. T. Shen and R. K. Wang, "Using ultrahigh sensitive optical microangiography to achieve comprehensive depth resolved microvasculature mapping for human retina," *J Biomed Opt* 16(10), 106013 (2011)

176. Y. Jia, J. Qin, Z. Zhi and R. K. Wang, "Ultrahigh sensitive optical microangiography reveals depth-resolved microcirculation and its longitudinal response to prolonged ischemic event within skeletal muscles in mice," *Journal of biomedical optics* 16(8), 086004 (2011)

177. S. Yousefi, J. Qin and R. K. Wang, "Super-resolution spectral estimation of optical micro-angiography for quantifying blood flow within microcirculatory tissue beds in vivo," *Biomed Opt Express* 4(7), 1214-1228 (2013)

178. R. K. Wang and L. An, "Doppler optical micro-angiography for volumetric imaging of vascular perfusion in vivo," *Opt Express* 17(11), 8926-8940 (2009)

179. Y. Jia, N. Alkayed and R. K. Wang, "Potential of optical microangiography to monitor cerebral blood perfusion and vascular plasticity following traumatic brain injury in mice in vivo," *J Biomed Opt* 14(4), 040505 (2009)

180. Y. Chen, A. D. Aguirre, L. Ruvinskaya, A. Devor, D. A. Boas and J. G. Fujimoto, "Optical coherence tomography (OCT) reveals depth-resolved dynamics during functional brain activation," *J Neurosci Methods* 178(1), 162-173 (2009)

181. Y. Chen, A. D. Aguirre, L. Ruvinskaya, A. Devor, D. A. Boas and J. G. Fujimoto, "Optical coherence tomography (OCT) reveals depth-resolved dynamics during functional brain activation," *Journal of Neuroscience Methods* 178(1), 162-173 (2009)

182. A. J. Kennerley, J. E. Mayhew, P. Redgrave and J. Berwick, "Vascular Origins of BOLD and CBV fMRI Signals: Statistical Mapping and Histological Sections Compared," *The open neuroimaging journal* 4(1-8 (2010)

183. A. M. VanDijk, P. A. Wieringa, M. van der Meer and J. D. Laird, "Mechanics of resting isolated single vascular smooth muscle cells from bovine coronary artery," *Am J Physiol* 246(3 Pt 1), C277-287 (1984)

184. D. Hayoz, Y. Tardy, B. Rutschmann, J. P. Mignot, H. Achakri, F. Feihl, J. J. Meister, B. Waeber and H. R. Brunner, "Spontaneous diameter oscillations of the radial artery in humans," *Am J Physiol* 264(6 Pt 2), H2080-2084 (1993)

185. C. J. Busuioc, F. C. Popescu, G. D. Mogosanu, I. Lascar, I. Pirici, O. T. Pop and L. Mogoanta, "Angiogenesis assessment in experimental third degree skin burns: a histological and immunohistochemical study," *Romanian journal of morphology and embryology = Revue roumaine de morphologie et embryologie* 52(3), 887-895 (2011)

186. W. K. Stadelmann, A. G. Digenis and G. R. Tobin, "Physiology and healing dynamics of chronic cutaneous wounds," *American journal of surgery* 176(2A Suppl), 26S-38S (1998)

187. K. M. Tichauer, J. A. Hadway, T. Y. Lee and K. St Lawrence, "Measurement of cerebral oxidative metabolism with near-infrared spectroscopy: a validation study," *Journal of cerebral blood flow and metabolism : official journal of the International Society of Cerebral Blood Flow and Metabolism* 26(5), 722-730 (2006)

188. Y. Li, S. Zhu, L. Yuan, H. Lu, H. Li and S. Tong, "Predicting the ischemic infarct volume at the first minute after occlusion in rodent stroke model by laser speckle imaging of cerebral blood flow," *J Biomed Opt* 18(7), 76024 (2013)

189. J. B. Bederson, L. H. Pitts, S. M. Germano, M. C. Nishimura, R. L. Davis and H. M. Bartkowski, "Evaluation of 2, 3, 5-Triphenyltetrazolium Chloride as a Stain for Detection and Quantification of Experimental Cerebral Infarction in Rats," *Stroke* 17(6), 1304-1308 (1986)

190. T. Chiang, R. O. Messing and W. H. Chou, "Mouse model of middle cerebral artery occlusion," *Journal of visualized experiments : JoVE* 48), (2011)

191. J. Vogel, M. A. Weigand, A. Behrens, E. F. Wagner, M. Schorpp-Kistner, M. Zimmermann and J. Schenkel, "Infarct volume after transient middle cerebral artery occlusion (MCAo) can be reduced by attenuation but not by inactivation of c-Jun action," *Brain Res* 1151(12-19 (2007)

192. W. Luo, Z. Wang, P. Li, S. Zeng and Q. Luo, "A modified mini-stroke model with region-directed reperfusion in rat cortex," *J Cereb Blood Flow Metab* 28(5), 973-983 (2008)

193. P. Li and T. H. Murphy, "Two-photon imaging during prolonged middle cerebral artery occlusion in mice reveals recovery of dendritic structure after reperfusion," *J Neurosci* 28(46), 11970-11979 (2008)

194. V. Kalchenko, Y. Kuznetsov, I. Meglinski and A. Harmelin, "Label free in vivo laser speckle imaging of blood and lymph vessels," *Journal of biomedical optics* 17(5), (2012)

195. H. Hashimoto, K. Isobe, A. Suda, F. Kannari, H. Kawano, H. Mizuno, A. Miyawaki and K. Midorikawa, "Measurement of two-photon excitation spectra of fluorescent proteins with nonlinear Fourier-transform spectroscopy," *Appl Opt* 49(17), 3323-3329 (2010)

196. W. Denk, J. H. Strickler and W. W. Webb, "Two-photon laser scanning fluorescence microscopy," *Science* 248(4951), 73-76 (1990)

197. B. A. Flusberg, J. C. Jung, E. D. Cocker, E. P. Anderson and M. J. Schnitzer, "In vivo brain imaging using a portable 3.9 gram two-photon fluorescence microendoscope," *Opt Lett* 30(17), 2272-2274 (2005)

198. O. Garaschuk, R. I. Milos and A. Konnerth, "Targeted bulk-loading of fluorescent indicators for two-photon brain imaging in vivo," *Nature protocols* 1(1), 380-386 (2006)

199. V. J. Srinivasan, H. Radhakrishnan, J. Y. Jiang, S. Barry and A. E. Cable, "Optical coherence microscopy for deep tissue imaging of the cerebral cortex with intrinsic contrast," *Opt Express* 20(3), 2220-2239 (2012)

200. R. Mostany and C. Portera-Cailliau, "A craniotomy surgery procedure for chronic brain imaging," *Journal of visualized experiments : JoVE* 12), (2008)

201. S. Ciaroni, T. Cecchini, F. Battelli and P. Del Grande, "Morphometric analysis of the development of the cortical layers and extension of the forceps major of the corpus callosum in the mouse," *Zeitschrift fur mikroskopisch-anatomische Forschung* 104(6), 898-906 (1990)

202. C. L. Grady, M. L. Furey, P. Pietrini, B. Horwitz and S. I. Rapoport, "Altered brain functional connectivity and impaired short-term memory in Alzheimer's disease," *Brain : a journal of neurology* 124(Pt 4), 739-756 (2001)